7-11-2014

Nanoscale Performance Mapping of Semiconducting Materials with Multiparametric Atomic Force Microscopy

James L. Bosse
University of Connecticut - Storrs, jlb05013@gmail.com

Nanoscale Performance Mapping of Semiconducting Materials with Multiparametric Atomic Force Microscopy

James Louis Bosse, Ph.D.

University of Connecticut, 2014

Atomic Force Microscopy (AFM) has become an indispensable tool for imaging the properties of surfaces at the nanoscale. With traditional AFM variations, quantitative mapping of surface properties is possible, but typically at the expense of spatial and/or temporal resolution. Accordingly, several new multiparametric AFM techniques have been developed to overcome these drawbacks in order to detect, understand, and ultimately enhance materials properties.

The first approach has been developed for Nanoscale Conductance Mapping (NCM), to efficiently investigate the nanoscale electronic properties of heterogeneous surfaces. The technique employs a sequence of conductive atomic force microscopy images, all acquired in a single area, but each with incrementally higher applied voltages. This generates a matrix of current versus voltage (I-V) spectra, providing nanoscale maps of conductance and current nonlinearities with negligible spatial drift. For crystalline and amorphous phases of a GeSe chalcogenide phase change film, conductance and characteristic amorphous phase "turn-on" voltages are mapped akin to traditional point-by-point I-V measurements, but acquired hundreds of times faster and with better spatial resolution. The methodology of the NCM technique has also been applied to spatially map the performance parameters for electro-mechanical (PMN-PT ferroelectrics) and nanotribology (SiO_2/Au) measurements.

The second approach has been developed for Ultrasonic Force Microscopy (UFM), which employs high frequency vibrations to map the nanomechanical properties of stiff materials and

subsurface features. Unfortunately, UFM critically depends on the usually poorly characterized high frequency behavior of AFM cantilevers. Leveraging automated multidimensional measurements, spectroscopic UFM (sUFM) is introduced to investigate a range of common experimental parameters. The data-rich sUFM signatures allow efficient optimization of ultrasonic-AFM based measurements, leading to best practices recommendations. Diverse materials such as Si, Cr, photoresist, and phase change memory films are specifically investigated.

In summary, multiparametric AFM techniques provide a means to efficiently investigate the nanoscale properties of heterogeneous surfaces with nanoscale resolution, with direct applicability to improving the performance of data storage systems, MEMS/NEMS, energy harvesting, and other semiconducting devices.

Nanoscale Performance Mapping of Semiconducting Materials with Multiparametric Atomic Force Microscopy

James Louis Bosse

B.S. University of Connecticut, 2009

M.S. University of Connecticut, 2012

A Dissertation

Submitted in Partial Fulfillment of the

Requirements for the Degree of

Doctor of Philosophy

at the

University of Connecticut

2014

APPROVAL PAGE

Doctor of Philosophy Dissertation

Nanoscale Performance Mapping of Semiconducting Materials with Multiparametric Atomic Force Microscopy

Presented by

James Louis Bosse, M.S.

Major Advisor _____

Bryan D. Huey

Associate Advisor _____

George A. Rossetti, Jr.

Associate Advisor _____

Ramamurthy Ramprasad

Committee Member _____

Mark Aindow

Committee Member _____

Harris L. Marcus

University of Connecticut

2014

Nanoscale Performance Mapping of Semiconducting Materials with Multiparametric Atomic Force Microscopy

This work is supported by:

Department of Energy, Office of Basic Energy Sciences, Division of Materials Sciences and Engineering, under award DE-SC0005037 (Electron and Scanning Probe Microscopies)

National Science Foundation, Division of Materials Research, Ceramics, under award 0909091 (Materials World Network)

Acknowledgements

First, I would like to thank my advisor Dr. Bryan D. Huey for asking me to be a part of his research group back in 2007. Throughout my undergraduate degree, he included me in many research projects and helped expose me to higher level research and the benefits of professorship. Bryan, I would like to thank you for pulling me out of industry in 2011 and inviting me back to the PhD program, which was a much needed escape from the absolute worst year of my life. The graduate school years have truly been a complete turnaround; the BEST years of my life. In that regard I would like to thank my labmates for making the lab an enjoyable experience. Particularly, I would like to thank Yasemin Kutes for being there through all of the trials and tribulations of graduate school. We had a lot of great times, right kid ☺? I would also like to thank my other labmates: Linghan Ye, Dr. Vincent Palumbo, Manuel Rivas, Alexandra Merkouriou, Alejandro Lluberes, and former members Dr. Nicholas Polomoff and Dr. Sungjun Lee.

I would also like to express gratitude to Dr. Oleg V. Kolosov for allowing me to work with him in Lancaster, UK, and also for being a great mentor and friend. You have always looked out for me and have always gone the extra mile. Also in Lancaster, I was fortunate to meet a great friend Riccardo Mazzocco. You made the time spent in the UK more enjoyable and I truly regret having to return to the US and leaving people like you behind. There are not too many people like you in this world. Remember, I still owe you! I would also like to acknowledge the other lab "mates" that made the time more enjoyable, namely Maria Timofeeva, Ben Robinson, Peter Tovee, Ilya Grishin, and Claire Tinker-Mill. Thank you all.

Aside from the lab and research, I owe a lot to my best friend and former ME/MSE alumni Greg White who has kept me grounded every single day of this thesis. It's easy to spend 100 hours per

week in the lab when you are always there to vent or chat about a multitude of topics including cars, careers, game theory, and humanity in general. I would also like to extend many thanks to former MSE alumni Dr. Juan C. Villegas and Dr. Gursel Akcay, who I have gotten to be great friends with recently and have helped me in my decision making regarding the industrial or professorship path. You are both awesome and I hope we keep in touch.

I would like to thank my dad for making all of this possible. I could have been working on cars in the garage with you, but you insisted that my brainpower was too strong for that. I know that we do not get to talk that often but I love you very much. Thanks for inspiring me to be better every single day. Without the sight of your success and your drive, ambition, etc. I would not have that role model to look up to. I hope that I can continue to follow in your footsteps and also make you proud.

I would also like to thank the rest of my awesome family, mom, Alexa, and Derrik. You are always around and I don't get to see you often but I love you too. Thanks for understanding how much time this career advancement takes. I hope you guys will come to visit me wherever I am.

Lastly, I would like to thank the following people who have helped steer me in the right direction: high school teachers Kevin Jameson and Morgan Hanna, my investing buddy George Tifft, UConn chemistry lecturer Dr. Edward 'EJ' Neth, and UConn professors Dr. Hal Brody, Dr. George A. Rossetti, Jr., Dr. Rampi Ramprasad, and Dr. Pamir Alpay. I owe all of you for many conversations that have helped me immensely through the last 10-15 years.

I would like to dedicate this thesis to my late grandfather and grandmother Michael J. Montos and Helen C. Montos.

Table of Contents

Table of Figures

Table of Tables

Chapter 1: Introduction

1.1. Scope of Research

Ever since Gordon E. Moore's famous prediction in 1965 that component density would double every two years [1], the market has used these types of performance targets not only for integrated circuits, but for hard drive storage, computer memory, and other applications outside of engineering [2]. This simple theory, coupled with Richard Feynman's idea to manipulate individual atoms [3], has impacted the world not only through device scaling, but also to nucleate the field of nanotechnology.

Significant efforts within this subset of applied physics have explored computer memory, including volatile (i.e. static and dynamic random-access memory (SRAM/DRAM)) and non-volatile (i.e. flash, magnetic and optical drive) systems. An attractive quality of the non-volatile memories is their lack of required power to maintain data storage, prompting the recent development of flash memory. However, despite its low cost and excellent data retention properties, flash has a much lower performance than DRAM in terms of reading and writing data, power consumption, and cycle endurance [4].

To address these concerns and provide a non-volatile memory equivalent, a resistive memory class called phase-change memory (PCM) has been developed, utilizing chalcogenide glass materials which undergo a rapid and reversible phase transition between the amorphous and crystalline states [5]. These are preferred candidates as each phase exhibits a high resistive and reflective contrast, ideal for electrical [6,7] or optical detection [8,9], respectively. Although PCM has a higher performance than flash, the three noteworthy factors that prevent this class of memory from surpassing DRAM performance is similar; power consumption, bit write time, and

cycle endurance [4]. It has been well established that the bit write time is limited by the amorphous to crystalline phase transition [10], with the threshold for switching proportional to power consumption. Therefore, focus has been placed to find fast crystallization stoichiometries with lower switching threshold power [11].

To study the threshold switching properties, several combinatorial approaches have been employed as they enable a variety of composition, switching potential, and/or switching times to be assessed. Instead of electrical signals to initiate the phase change, these often implement pulsed lasers [12] largely driven by the widespread use of phase change films in optical storage media. To characterize the electrical properties of these materials, variations of Atomic force microscopy (AFM) have also been used extensively [13]. Here, the nanosecond scale threshold for switching between the amorphous and crystalline phases in GeSe PCM thin films were investigated with conducting atomic force microscopy. Bit crystallization was achieved in as low as 15 ns, the fastest reported with scanning probe based methods. Additionally, the switched bits further reveal correlations between volume, pulse amplitude, and pulse duration, with conductivity contrast varied over 2-3 orders of magnitude. The AFM is an attractive tool for this use as it allows for property investigations with nanoscale spatial resolution, displayed as a map to correlate features as a function of defects, changes in topography, or other artifacts [14].

However, the AFM capabilities have not been realized fully as measurements are typically acquired with sacrificed dimensionality. For example, if one desired to map the electrical properties of a PCM thin film, the AFM tip would raster with a constant applied voltage and measure the current over a 2-D region. Although spatially resolved, this provides only one data point in the current versus voltage (I-V) axis. Similarly for a more quantitative approach, the AFM tip may be positioned at a fixed location (rastering disabled), and a complete I-V curve

may be acquired to map the electrical response. However, this approach lacks the influence of defects, changes in phase, etc., also resulting in sacrificed dimensionality. Therefore, a quantitative, multidimensional AFM technique called Nanoscale Conductance Mapping (NCM) has been developed to address these issues. With this method, a sequence of conductive AFM images acquired in a single area are collected with incrementally higher applied voltages. The images are placed into a matrix correlating I-V spectra to a spatial map of topography. The conductivity and current nonlinearities were observed for crystalline bits pulsed in amorphous GeSe films, and also for an as-grown amorphous film.

After successful application to PCM, the method was applied to piezoelectric materials by generating amplitude versus frequency spectra, providing nanoscale maps of the maximum piezoresponse amplitude and corresponding resonant frequency for adjacent grains in a polycrystalline $BaTiO_3$ thin film. Aside from electrical and electro-mechanical measurements, the method was also combined with high-speed AFM and applied to nanotribology measurements in the form of Friction Coefficient Mapping (FCM). The technique acquires sequential friction force images (AFM trace minus retrace), each with incrementally lower loads. This results in spatially resolved friction force curves, allowing for true tribological properties to be mapped, i.e. coefficient of friction, friction at zero applied force, etc. These parameters are determined at a scan velocity as fast as 2 mm/s for micro-fabricated SiO_2 mesas and Au coated pits, yielding results that are identical to traditional speed measurements despite being ~1000 times faster. To demonstrate the upper limit of sliding velocity for the custom setup, the friction properties of mica are reported from 200 µm/sec up to 2 cm/sec, approaching the operating speeds of real MEMS/NEMS or data storage devices [15].

While scanning at high rates approaching the vertical feedback bandwidth for the tribology study, it was apparent that the measured topography was featureless. Interestingly, the qualitative topography was captured in the cantilever deflection signal. As the scan rate was decreased, allowing for the vertical feedback to operate more effectively, the deflection signal was traded back to the topography signal. This observation led to the development of Error-Corrected AFM, a simple image correction method where calibrated error signals such as deflection and/or amplitude may be summed with the simultaneously acquired topography signals to substantially improve both height and lateral accuracy (3-5 fold decrease in image error). This concept has been proven for contact mode, AC mode, and high speed imaging, as well as property mapping such as phase contrast AFM, with obvious extensions to many specialized AFM variations. The technique is also easily applied to any AFM system, either in real time or in post-processing. Such Error Corrected AFM therefore offers a simple, broadly applicable approach for more accurate, more efficient, and more user-friendly implementation of AFM for nanoscale topography and property mapping.

As part of the National Science Foundation's Materials World Network research funding, two student exchanges took place between Lancaster, UK and Storrs, CT, USA to investigate the electrical and nanomechanical properties of phase change memory thin films. One collaborator site (Dr. Oleg Kolosov's facilities in Lancaster University, UK) has the capability to prepare, optically pulse, perform shallow-angle cross-sections, and nanomechanically characterize the PCM thin films. The travel not only resulted in investigation of these films, but also the exchange of knowledge. For example, while applying the nanomechanical characterization technique ultrasonic force microscopy (UFM) to the films, it was clear that many experimental parameters were chosen by tribal knowledge, without a systematic approach to optimization.

Also, the obtained results were largely qualitative, and suffered from repeatability issues. Previous instrumentation and programming experience led to the development of a spectroscopic approach to ultrasonic force microscopy (sUFM). The technique leveraged automated multidimensional measurements to investigate a range of common experimental parameters such as the length and force applied with AFM cantilevers, the spatial and frequency response of piezotransducers, and the transfer of ultrasonic vibrations between the probe and specimen. The data-rich signatures allowed for the efficient optimization of ultrasonic-UFM based measurements, leading to best practice recommendations. A diverse range of materials with known stiffness variations were investigated, including Si, Cr, and photoresist. This work thereby provided essential insight into the reliable use of MHz vibrations with AFM, and direct evidence substantiating phenomena such as sensitivity to adhesion, diminished friction for certain ultrasonic conditions, and the particular benefit of UFM and related methods for nanoscale mapping of stiff materials. The sUFM technique was then applied to characterize the nanomechanical morphology of free-surface and shallow angle cross-sections for amorphous and crystalline phases in $Ge_2Sb_2Te_5$ and GeTe thin films, displaying nucleation and growth dominated crystallization kinetics, respectively [16]. Combining surface and cross-section nanomechanical mapping in this manner allowed 3D analysis of microstructure and defects with nanoscale lateral and depth resolution, applicable to a wide range of materials characterization studies where the detection of subtle variations in elastic modulus or stiffness are required.

Another technique utilized at the collaborators site is scanning thermal microscopy (SThM), for the investigation of nanoscale thermal properties. This is a well established technique, implemented within three doctoral student theses [17-21]. When combined with quantitative physical modeling, the technique is powerful enough to spatially map and quantify thermal

properties such as thermal conductivity, thermal boundary conductance, etc. These methods were directly applied to the amorphous and crystalline phases in PCM thin films of varying thickness and stoichiometry. Although investigated for the PCM thin films here, the technique is also applicable to characterize other thin film materials with low thermal conductivity.

The all-encompassing focus of this thesis work is to therefore implement multiparametric improvements to various AFM scanning modes to map performance and properties of semiconducting materials, allowing for quantitative and efficient investigations that would otherwise be difficult or impossible with existing methods.

1.2. References

1. Gordon E Moore, (McGraw-Hill New York, NY, USA, 1965).
2. Robert Carlson, Biosecurity and bioterrorism: biodefense strategy, practice, and science **1** (3), 203 (2003).
3. Richard P Feynman, Engineering and science **23** (5), 22 (1960).
4. H. S. P. Wong, S. Raoux, Kim SangBum, Liang Jiale, John P. Reifenberg, B. Rajendran, Mehdi Asheghi, and Kenneth E. Goodson, Proceedings of the IEEE **98** (12), 2201 (2010).
5. Stanford R. Ovshinsky, Physical Review Letters **21** (20), 1450 (1968).
6. M. H. R. Lankhorst, B. W. S. M. M. Ketelaars, and R. A. M. Wolters, Nat Mater **4** (4), 347 (2005).
7. M. Wuttig and N. Yamada, Nat Mater **6** (11), 824 (2007).
8. M. Libera and M. Chen, Journal of Applied Physics **73** (5), 2272 (1993).
9. W. Welnic, S. Botti, L. Reining, and M. Wuttig, Physical Review Letters **98** (23) (2007).
10. W. J. Wang, L. P. Shi, R. Zhao, K. G. Lim, H. K. Lee, T. C. Chong, and Y. H. Wu, Applied Physics Letters **93** (4) (2008).
11. W. Welnic, A. Pamungkas, R. Detemple, C. Steimer, S. Blugel, and M. Wuttig, Nat. Mater. **5** (1), 56 (2006).
12. Simone Raoux, Robert Shelby, Becky Munoz, Martina Hitzbleck, Daniel Krebs, Martin Salinga, Michael Woda, Michael Austgen, Kyung-Min Chung, and Matthias Wuttig.
13. H. Kado and T. Tohda, Applied Physics Letters **66** (22), 2961 (1995).
14. G. Binnig, C. F. Quate, and C. Gerber, Physical Review Letters **56** (9), 930 (1986).
15. Tao Zhenhua and Bharat Bhushan, Rev. Sci. Instrum. **77** (10), 103705 (2006).
16. J. H. Coombs, A. P. J. M. Jongenelis, W. Vanesspiekman, and B. A. J. Jacobs, Journal of Applied Physics **78** (8), 4918 (1995).
17. A. Majumdar, Annu Rev Mater Sci **29**, 505 (1999).
18. Manuel E. Pumarol, Mark C. Rosamond, Peter Tovee, Michael C. Petty, Dagou A. Zeze, Vladimir Falko, and Oleg V. Kolosov, Nano Letters **12 (6)**, 2906 (2012).

19. P. Tovee, M. Pumarol, D. Zeze, K. Kjoller, and O. Kolosov, Journal of Applied Physics **112** (11) (2012).
20. Peter D Tovee and Oleg V Kolosov, arXiv:1110.6055v3 (2013).
21. Peter D Tovee, Manuel E Pumarol, Mark C Rosamond, Robert Jones, Michael C Petty, Dagou A Zeze, and Oleg V Kolosov, arXiv:1305.6240 (2013).

Chapter 2: Nanoscale Switching in GeSe Phase Change Memory Thin Films by Atomic Force Microscopy

2.1. Abstract

Nanosecond scale threshold switching is investigated with conducting atomic force microscopy for an amorphous GeSe film. Switched bits exhibit 2-3 orders of magnitude variations in conductivity, as demonstrated in phase change based memory devices. Through the nm-scale atomic force microscope (AFM) probe, this crystallization was achieved with pulse durations of as low as 15 ns, the fastest reported with scanning probe based methods. Conductance AFM imaging of the switched bits further reveals correlations between the switched volume, pulse amplitude, and pulse duration. The influence of film heterogeneities on switching is also directly detected, of tremendous importance for optimal device performance.

2.2. Introduction

Since the discovery of chalcogenide phase change materials as a candidate for future random access memory [1], significant research has been performed to improve read/write speeds, reduce power consumption, and enhance read/write cycle endurance [2]. These materials are ideal candidates due to the high resistive contrast between amorphous and crystalline states, typically initiated by voltage/current induced Joule heating [3]. As the dimensions of such devices diminish, the required switching time and power becomes particularly attractive when compared to competing solid state memory technologies [2,4-6].

To study the threshold switching properties of phase change materials, several combinatorial approaches [7] have been employed as they efficiently enable a variety of composition, switching potential, and/or switching times to be assessed. Instead of electrical signals to initiate

the phase change, these often implement pulsed lasers [8] largely driven by the widespread use of phase change films in optical storage media (CD, DVD, Blue Ray, etc.). To characterize the electrical properties of these materials, variations of atomic force microscopy (AFM) have also been used extensively [9]. In this work, conducting AFM investigations of phase change switching are extended to the nanosecond scale regime, with arrays of pulses applied combinatorially to relate switching dynamics to a range of practical pulse amplitudes and durations. Subsequent conductance mapping with the same AFM probe correlates writing parameters to bit sizes. Current maps on the order of pA additionally reveal how heterogeneities in the GeSe film can influence threshold switching properties.

2.3. Materials and Methods

The thin film measured in this work was prepared on an un-doped Si substrate by thermal co-evaporation of Ge and Se source materials in separate crucibles, creating a 50 nm amorphous GeSe film on a 50 nm conducting Pt back electrode using deposition rates of 2 and 1 Å/s, respectively [10]. The film was characterized in the as-deposited, amorphous state with no thermal treatments applied, e.g. annealing. From electron probe X-ray microanalysis, the GeSe film was determined to have the composition of $Ge_{51}Se_{49}$ (at.%). Arbitrary pulses from an external function generator are applied through a wire and a silver paint connection to the back electrode. A grounded conducting AFM probe and a built-in preamp complete the circuit for through-film current sourcing and/or detection. Figure 1(a) presents the schematic for the measurements. The pulse generation hardware (National Instruments, PXI-5421) was programmed to apply voltage pulses with varying amplitude and duration in a 5 x 5 array, synchronized with the fast scan axis (x) of the AFM for consistency in bit spacing. The voltage pulses were simultaneously recorded on a separate imaging channel in the AFM to verify their

location. The output impedance of the pulsing hardware and coaxial cable are both matched to 50 Ω to prevent attenuation and reflection. The leading and trailing edge of each pulse is 10 ns, while each pulse width is measured at full width of half maximum (FWHM). A schematic example of one AFM line scan is presented in Figure 1(b), with 5 pulses at 8 V ranging from 15 to 75 ns. Note that the pulse durations have been substantially expanded in X-direction in schematic diagram Figure 1(b) to demonstrate the distinct pulse shapes in the 5 columns of pulses. In reality, based on the tip speed, each pulse was applied in substantially less time in effectively a single pixel.

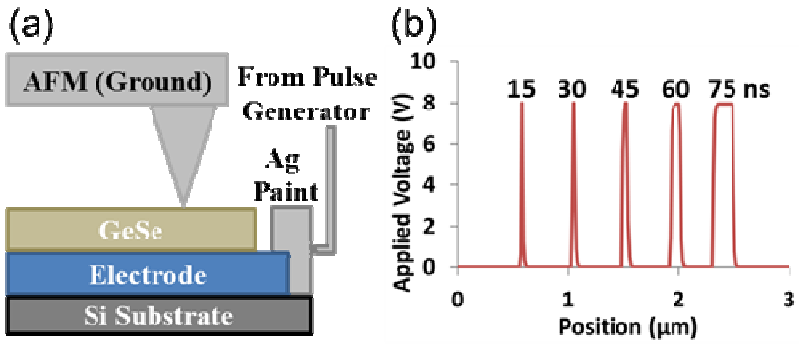

Figure 1: Schematic illustration of the layered GeSe structure (a). Line scan cross section of the AFM image, revealing 5 pulses at 8 V ranging from 15 ns to 75 ns (b).

All measurements were performed at room temperature and enclosed in the sealed scanning chamber of an AFM (Asylum Research, Cypher). A constant flow of dry Argon gas (relative humidity below 3%) at 20 CFH was used to minimize specimen oxidation during pulsing, and measurements were performed on the same day to ensure a consistent relative humidity for all data sets [11,12]. Current detection hardware (Asylum Research, ORCA) features dual gain current detection providing a maximum of ±10 µA/V with 1 nA resolution (low gain) or ±10 nA with 5 pA resolution (high gain). Diamond coated silicon cantilevers (Nanosensors, CDTP-NCHR) are employed throughout, with a quoted tip length of 10-15 µm, tip radius of 200-300

nm, cantilever length of 125 ± 10 μm, and resonant frequency of 275-720 kHz. Each cantilever's spring constant was calibrated in-situ, with typical values between 100-110 N/m. The diamond coated probes are ideal as they show negligible wear even with the application of high voltage pulses and normal forces, necessary for maintaining a consistent contact area throughout all current measurements.

The pulse durations and amplitudes covered range from 10 to 300 ns and 4 to 10 V, with 0 V applied at all other times. Initial work leveraged combinatorial approaches by employing distinct pulse durations for each column in the pulse grid, and distinct pulse amplitudes for each row. All results presented here, though, utilize a single pulse amplitude for all 25 pulses in any given image (N=5 rows, but each column is still based on a distinct duration). This provides important statistical insight into the switching process for the specimen being studied (N is at least 5 for each pulsing condition in any given image). Once the pulsing process is completed during a single AFM image (5 conditions), a second conductive AFM (c-AFM) image is acquired at the same location with a fixed 'read' voltage of 1 V and current channel engaged to distinguish between the crystalline and amorphous phases. This 'read' voltage is below the threshold switching voltage so as to not create any additional crystalline nuclei. Note that such write/read image pairs at additional pulse amplitudes are conducted at new locations but in the same specimen region (±50 um), in order to avoid any convolution between results with distinct parameters. The set-point force for both pulse writing and pulse reading are equivalent (4060 nN), and the tip-sample adhesive force under zero applied bias was measured by force-displacement curves (470 nN).

2.4. Results and Discussion

Figure 2(a) shows representative c-AFM results (read images) following pulse voltage amplitudes of 9, 7, and 5 V, as labeled, based on columns of pulses with durations ranging from 10-50 nanoseconds as noted. From such a combinatorial approach, the minimum pulse amplitude and duration required to crystallize the amorphous film can be extracted. Clearly, switching occurs in shorter times with higher voltages as anticipated. Furthermore, variability in the written bits is observed within a single column (switching duration), either because the pulsing parameters are exactly at the switching threshold (unlikely), or due to subtle spatial heterogeneities in the specimen (local composition, thickness, conductivity, etc.).

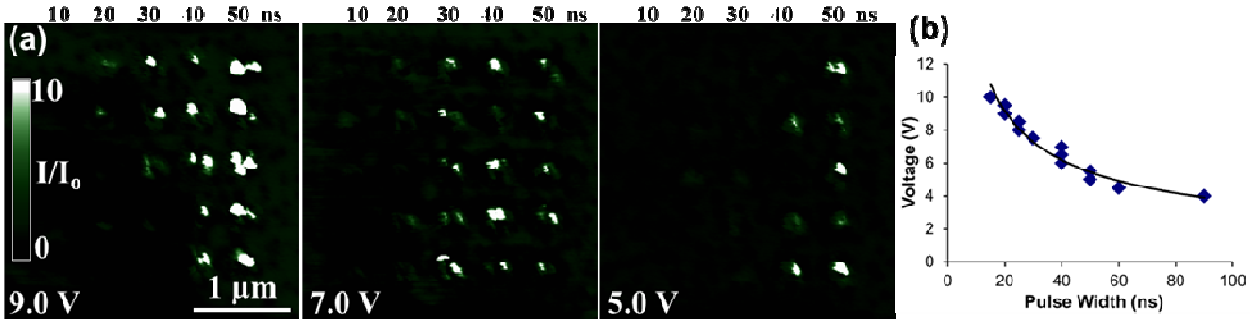

Figure 2: Current ratio images ($I/I_{amorphous\ background}$) of the pulsed amorphous GeSe film with varying pulse amplitude and duration (a). As noted, each image is acquired at varying pulse amplitudes, while each column of pulses is for a distinct pulse duration noted above the images. Minimum pulse amplitude and pulse duration required for the amorphous to crystalline phase transition in a GeSe thin film (b).

To analyze the switching threshold, a "current ratio" (I/I_o) was mapped for each of the c-AFM results. This is determined by dividing each image pixel (I) by the "background" current (I_o), which is defined as the average current for the deposited amorphous film everywhere except at the pulses. I_o ranged from 3 to 12 nA depending on the image parameters. The criteria used to establish an adequate phase transition (actual switched bit) is an I/I_o ratio of 10 or higher. Accordingly, the minimum pulse amplitude and duration detected to surpass this phase transition threshold, from Figure 2(a) and several equivalent experiments, is presented in Figure 2(b). The

curve-fit is intended to guide the eye; in fact no switching was observed for pulse amplitudes less than 4 V. Multiple threshold amplitudes appear for certain durations because several conditions were repeated to establish consistency.

The fastest phase transition observed occurred with a pulse duration of just 15 ns for a 10 V pulse amplitude (the max applicable). This represents the fastest reported crystallization speed based on scanning probe methods for similar-thickness phase change films. Pulse durations shorter than 15 ns can also be reliably applied [13], and would presumably also reveal switching if higher biases could be employed. The maximum possible pulse amplitude is 10 V for the present hardware, though, so no appreciable phase transition was expected for less than 15 ns. The lowest amplitude phase transition occurred upon 4 V pulsing with pulse durations of 90 ns or longer. Pulse amplitudes of 3.5 V or less did not produce any phase transitions, even for pulse durations up to 600 ns.

Switching thresholds in the range of 4-8 V have similarly been reported by other chalcogenide phase change film studies, though necessitating much longer pulse durations [4,14-17]. Minimum switching fields ranged from 8.1 – 94 V/μm [4], compared to approximately 80 V/μm for the GeSe film presented here. Several factors influence these results. The electrical conductivity of the AFM probes is relatively low in these experiments, nominally <3kΩ, favoring low switching thresholds compared to other SPM studies but of course higher thresholds compared to direct microfabricated devices. The thermal conductivities of the probe and junction are also important, here relatively high given the doped diamond probe compared to standard metal tip measurements (hence demanding higher switching thresholds). The more general specimen configuration is relevant as well. For instance, separate studies of layered chalcogenide structures have observed benefits from incorporating resistive capping layers

[14,15]. The films here are uncapped to directly access the GeSe surface, with all experiments conducted in the presence of Ar flow to minimize oxidation effects. For practical devices, the high thermal stability and crystallization temperature (~350 ºC) of GeSe [10], coupled with the fast phase transitions demonstrated here, supports GeSe as a candidate for high-temperature RAM devices.

Accordingly, in addition to characterizing the presence of switched bits and observed current ratios, the bit areas were also measured for the various switching conditions. The criteria for measuring switched bit size utilized the same current ratio (I/I_o of 10) as the threshold switching experiments. Unsurprisingly, there was no appreciable correlation between measured crystalline bit size and pulse duration, in agreement with most SPM based electrical switching experiments below a certain threshold where the feature size is largely controlled by the contact area of the AFM probe [16,18] and the pulse amplitude [14,17,19], not the pulse duration.

The results do, however, reveal a trend of an increased current ratio I/I_o as the pulse duration increases. This suggests that only a partial volume of material directly beneath the AFM apex undergoes the crystalline phase transition for shorter pulse durations. As the pulse duration increases, a higher volume percentage of material transforms to the conducting crystalline phase. This is evident in the AFM images and line scan cross sections of current maps, Figure 3, exhibiting 5x5 arrays of 10 V amplitude pulses for distinct pulse durations as noted (unlike Figure 2(a), each column of pulses is identical for any given image). For a very long 500 μs pulse the average I/I_o ratio is 128, whereas for shorter pulse durations of 300 ns and 100 ns, the average I/I_o is 69 and 41, respectively. It is interesting to note that even with a 500 μs pulse duration at 10 V, the material volume has not completely transformed into the crystalline state. This was verified by engaging the AFM probe with the film and performing I-V spectroscopy

measurements between 0 and 10 V for an entire second. The average I/I_o current ratio for the crystalline dot generated by this effectively much longer pulse is 588, almost 5 times greater than for a still relatively long 500 µs pulse. This observation is consistent with standard crystallization kinetics for this material class, as nucleation and growth are competing processes as a function of temperature [20].

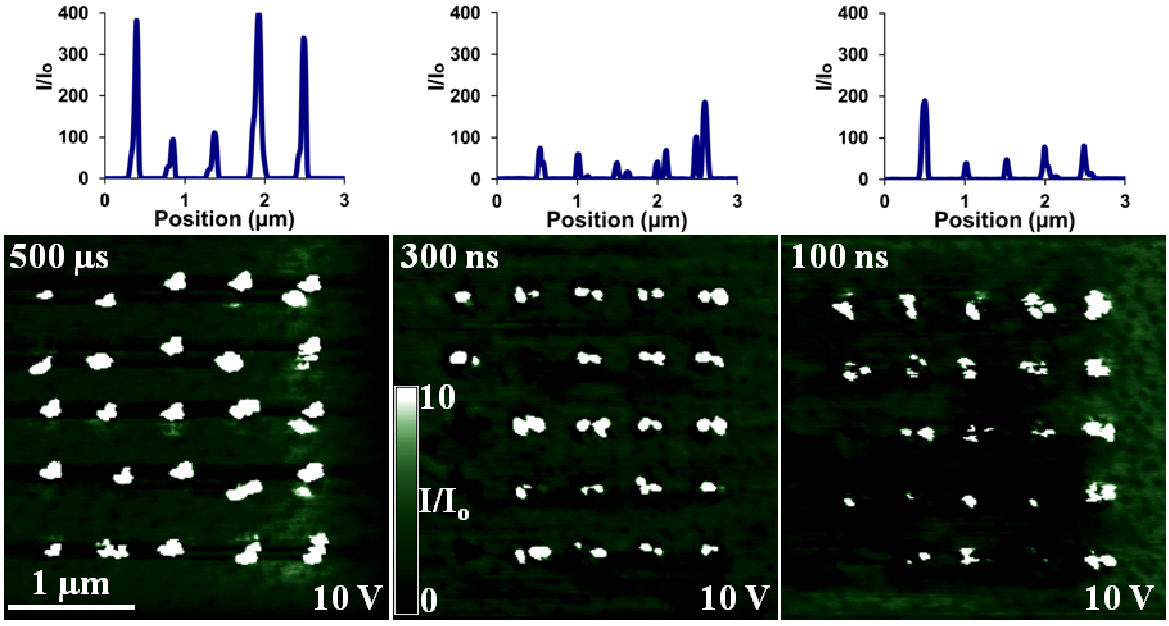

Figure 3: Current ratio images (I/Iamorphous background) and representative line-scan cross sections as a function of pulse duration. The average I/Io values for 500 µs, 300 ns, and 100 ns pulses are 128, 69, and 41, respectively.

One of the important benefits of utilizing AFM for electric property characterization is the ability to simultaneously map both topographic and electronic properties, providing evidence of heterogeneities at the nanoscale. For example, with the 5x5 array of 300 ns and 10 V pulses in Figure 3, the crystallized bits exhibit many different current contrasts and morphologies (beyond obvious tip-shape artifacts). In 4 of the 25 pulsed elements, no crystallization of the amorphous film is observed. In the other 21 pulsed elements, the average crystallized bit area is 8500 ± 5100 nm^2. This confirms nano to microscale heterogeneities in the initial amorphous film, leading to

spatial variations in conductivity, threshold switching, etc. Such heterogeneities can cause fluctuations in localized energy trap densities [21,22], modifying carrier transport in the amorphous state [3,23-26]. This would strongly influence local heating, and thus influence the onset of a phase transition (switching). One common source of such heterogeneity, particularly in glasses, is fluctuations in material density due to the presence of pores, vacancies, or even differences in coordination [27]. Additional possibilities are chemical fluctuations, such as impurity atoms or local changes in composition. Other likely sources are structural defects, such as dangling bonds or interfaces, or structural relaxation [6,28]. GeSe chalcogenide glasses can also exhibit physical ageing, although this effect is negligible for the stoichiometry and natural storage time scale considered here [29].

Any of these defects could modify the energy barrier for carrier transport, leading to a spatially varying energy profile or "energy landscape." Since electron transport will preferentially occur along path(s) of least barrier energy in this energy landscape [25], regions that possess a higher energy barrier than their surroundings will not transform as easily. In fact, a map of the current ratios of the amorphous film when applying a 2V 'read' bias reveals exactly such spatial variations for electronic transport, Figure 4(a).

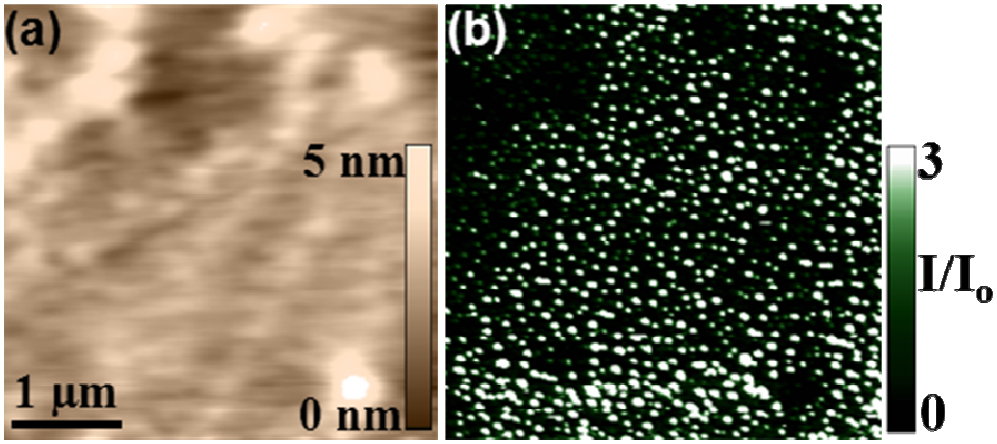

Figure 4: Topography (a) and current ratio (I/I_o) image (b) of the amorphous film. These current variations allow for low-resistance pathways, which lead to spatial heterogeneity in the threshold switching process.

Based on a histogram of the current measurements in the image, 95% of the imaged area exhibits a current ratio between 0 and 3.84 with respect to the average amorphous current (here I_o is the average current in the entire image). This is relatively insignificant compared to the several order of magnitude increases in current for pulsed bits as in Figures Figure 2(a) and Figure 3. Nevertheless, it is important in terms of heterogeneities of local switching thresholds and hence switched locations or patterns upon pulsing. For example, the written bits in Figures 2(a) and Figure 3 always occur near, but seldom exactly at, their programmed locations at specific points on a grid (as in Figure 1(b)), with error on the order of 100 nm. This is explained because of the conducting variations in the amorphous film, Figure 4(b), which are randomly scattered sub-100 nm patches with an average separation of approximately 100 nm. These are not related to any surface microstructure according to topography (Figure 4(a)). When a pulse is applied at any given position, current thus preferentially flows through the nearest low-resistance pathway (or pathways). The initial energy landscape, and how it evolves during the switching process, therefore has important implications for electronic transport. The same is true for the related yet distinct thermal transport, another crucial mechanism during phase change switching.

By utilizing the AFM to monitor spatial heterogeneities in the switching threshold, further studies can be performed to improve chalcogenide film fabrication for data storage devices, such as tailoring the composition to optimize switching thresholds, improving fabrication for a more uniform amorphous response, seeding multiple nucleation sites within each bit area for higher speed and lower energy switching, etc. Efforts to engineer low power consumption (lower switching thresholds), and/or improved data retention (structural stability), can therefore be enhanced.

2.5. Conclusion

In summary, the threshold switching dynamics of a GeSe chalcogenide phase change material have been characterized using conducting AFM, implementing pulse durations as short as 15 ns. Current ratio maps of the switched bits uniquely identify an increase in the crystalline phase volume with increasing pulse durations. The bit size is independent of pulse amplitude. Finally, statistical and spatial variations in the results correlate with variations in the conductivity of the initial amorphous film, demonstrating the particular value of AFM-based studies of such resistive switching processes which are sensitive to variations in the energy landscape at the nanoscale.

2.6. References

1. Stanford R. Ovshinsky, Physical Review Letters **21** (20), 1450 (1968).
2. D. Loke, T. H. Lee, W. J. Wang, L. P. Shi, R. Zhao, Y. C. Yeo, T. C. Chong, and S. R. Elliott, Science **336** (6088), 1566 (2012).
3. S. Senkader and C. D. Wright, Journal of Applied Physics **95** (2), 504 (2004).
4. D. Krebs, S. Raoux, C. T. Rettner, G. W. Burr, M. Salinga, and M. Wuttig, Applied Physics Letters **95** (8) (2009).
5. T. Gotoh, K. Sugawara, and K. Tanaka, Jpn J Appl Phys 2 **43** (6B), L818 (2004).
6. W. J. Wang, L. P. Shi, R. Zhao, K. G. Lim, H. K. Lee, T. C. Chong, and Y. H. Wu, Applied Physics Letters **93** (4) (2008).
7. M. Petro, S. H. Nguyen, M. J. Liu, and O. Kolosov, Macromolecular Rapid Communications **25** (1), 178 (2004).

8. Simone Raoux, Robert Shelby, Becky Munoz, Martina Hitzbleck, Daniel Krebs, Martin Salinga, Michael Woda, Michael Austgen, Kyung-Min Chung, and Matthias Wuttig.
9. H. Kado and T. Tohda, Applied Physics Letters **66** (22), 2961 (1995).
10. Doo Seok Jeong, Hyungkwang Lim, GoonHo Park, Cheol Seong Hwang, Suyoun Lee, and Byungki Cheong, Journal of Applied Physics **111** (10), 102807 (2012).
11. P. Avouris, R. Martel, T. Hertel, and R. Sandstrom, Appl Phys a-Mater **66**, S659 (1998).
12. X. X. Xiao, Z. D. Xiao, and Z. H. Lu, J Nanosci Nanotechno **5** (8), 1277 (2005).
13. N. A. Polomoff, A. Rakin, S. Lee, V. Palumbo, P. Yu, Y. H. Chu, R. Ramesh, and B. D. Huey, Journal of Applied Physics **109** (9) (2011).
14. S. Gidon, O. Lemonnier, B. Rolland, O. Bichet, C. Dressler, and Y. Samson, Applied Physics Letters **85** (26), 6392 (2004).
15. C. D. Wright, M. Armand, and M. M. Aziz, Ieee T Nanotechnol **5** (1), 50 (2006).
16. H. Bhaskaran, A. Sebastian, A. Pauza, H. Pozidis, and M. Despont, Review of Scientific Instruments **80** (8) (2009).
17. J. Kim, Scanning **32** (5), 320 (2010).
18. S. Raoux, G. W. Burr, M. J. Breitwisch, C. T. Rettner, Y. C. Chen, R. M. Shelby, M. Salinga, D. Krebs, S. H. Chen, H. L. Lung, and C. H. Lam, Ibm J Res Dev **52** (4-5), 465 (2008).
19. F. Yang, L. Xu, R. Zhang, L. Geng, L. Tong, J. Xu, W. N. Su, Y. Yu, Z. Y. Ma, and K. J. Chen, Appl Surf Sci **258** (24), 9751 (2012).
20. J. Orava, A. L. Greer, B. Gholipour, D. W. Hewak, and C. E. Smith, Nat Mater **11** (4), 279 (2012).
21. J. Frenkel, Physical Review **54** (8), 647 (1938).
22. H. H. Poole, Philosophical Magazine Series 6 **32** (187), 112 (1916).
23. Morrel H. Cohen, H. Fritzsche, and S. R. Ovshinsky, Physical Review Letters **22** (20), 1065 (1969).
24. D. Ielmini and Y. G. Zhang, Journal of Applied Physics **102** (5) (2007).
25. M. Rizzi and D. Ielmini, presented at the Electron Devices Meeting (IEDM), 2012 IEEE International, 2012 (unpublished).
26. G. B. Beneventi, L. Guarino, M. Ferro, and P. Fantini, J Appl Phys **113** (4) (2013).
27. Y. G. Choi, A. Kovalskiy, B. K. Cheong, and H. Jain, Chem Phys Lett **534**, 58 (2012).
28. D. Fugazza D. Ielmini, M. Boniardi, G. Montemurro, and A. L. Lacaita, in *E\PCOS* (Politecnico di Milano, Italy, 2010).
29. R. Golovchak, A. Kozdras, O. Shpotyuk, S. Kozyukhin, and J. M. Saiter, J Mater Sci **44** (15), 3962 (2009).

Chapter 3: Multidimensional SPM Applied for Nanoscale Conductance Mapping

3.1. Abstract

A new approach has been developed for Nanoscale Conductance Mapping (NCM) based on multidimensional Atomic Force Microscopy to efficiently investigate the nanoscale electronic properties of heterogeneous surfaces. The technique employs a sequence of conductive atomic force microscopy images, all acquired in a single area, but each with incrementally higher applied voltages. This generates a matrix of current versus voltage (I-V) spectra, providing nanoscale maps of conductance and current nonlinearities with negligible spatial drift. For crystalline and amorphous phases of a GeSe chalcogenide phase change film, conductance and characteristic amorphous phase "turn-on" voltages are mapped with results providing traditional point-by-point I-V measurements, but acquired hundreds of times faster. Although similar to current imaging tunneling spectroscopy in a scanning tunneling microscope, the NCM technique does not require conducting specimens. It is therefore a promising approach for efficient, quantitative electronic investigations of heterogeneous materials used in sensors, resistive memories, and photovoltaics.

3.2. Foreword

Although current images of the crystalline bits in the phase change material films produced sufficient contrast (Chapter 2:), they lack the ability to quantitatively map heterogeneities in electronic properties, i.e. conductance, critical for device performance investigations. Such quantitative techniques exist for the AFM, but are typically employed in a point-by-point fashion

at slow rates, suffering from thermal drift and poor spatial resolution. The following work aims to develop an AFM technique to address these existing characterization limitations.

3.3. Introduction

For several decades, the electronic properties of materials have been characterized with various atomic force microscopy (AFM) [1] based approaches targeting optimization of the designs and performance of a wide range of electronic devices. Such electronic investigations are especially relevant to micro- and nano-electromechanical systems (MEMS/NEMS) [2-6], organic and ceramic photovoltaics [7-9], oxide semiconductors [10-14], phase change memories [15-20], and other systems [21-28]. In these devices, the nanoscale spatial distribution in the local electronic response is critical for their operation, but its characterization is increasingly difficult to achieve as dimensions diminish and complexity rises.

Of course scanning tunneling microscopy (STM) can be utilized for current or conductance detection in circumstances where specimens are sufficiently conducting, but specialized surface preparation and/or vacuum environment is often required [29]. Therefore AFM based measurements have become more commonplace [30-33] as they are more compatible with lower conductivity specimens than STM necessitates and/or samples where only particular regions are conducting. Two main approaches have emerged. In first, the AFM maps currents with nanoscale resolution by scanning an area with a fixed voltage and recording the current, pixel-by-pixel [2,26,32,34]. Such individual images are excellent at qualitatively identifying heterogeneities, especially as they can be directly correlated with simultaneously imaged topographic structures. Nevertheless, images alone evidently do not provide quantitative details of more complicated electronic properties such as nonlinearities in the current-*vs.*-voltage, or 'I-V', response. For such purposes, the tip is instead typically fixed at a given location of interest and the current is

measured as voltage is swept producing I-V spectra [3,28,35]. Essentially, this adds an extra dimension in terms of electrical measurements, with the expense of sacrificing imaging capability.

Naturally, the *x* and *y* dimensionality can be recovered by collecting additional I-V spectra after repositioning the AFM probe, either at user-selected positions, at points along a user-defined line, or somehow distributed across an area of interest. These results are then reassembled into a matrix of I-V spectra, with known *x*, *y* positions for each, linked with the AFM measured topography *z* or cross-sectioned along any planes of interest where data set includes *x, y, z* coordinates, and *I, V* electrical parameters. For example, *x*-*y* maps of the current at certain bias voltages can be reconstructed, equivalent to a simple current image as described above. Similarly, I-V sections allow one to visualize the collective (spatially independent) current *vs.* voltage response, while *I*-*z* planes yield the current as a function of topographic height. Such results are obviously powerful for their ability to identify locally complex current-voltage relationships, for instance to relate such properties to specimen positions, depths (in trenches or on islands), and characteristic voltages (coercive fields, breakdown potentials).

Unfortunately, the precise locations of I-V spectra acquired pixel by pixel are difficult to synchronize with pre- or post- AFM images and their spatial resolution is inevitably, at best, very pixelated. This is primarily due to the relatively long settling times required when repositioning the AFM probe at each new pixel. Practical times spent per pixel are therefore relatively long compared to continuous scanning by an AFM tip and corresponding multidimensional Scanning Probe Microscopy (mSPM) experiments [36]. For example, the second column of Table I presents pixel times in seconds for a range of parameters for individual spectra or scanning measurements. The 4th row, italicized, indicates the most common settings for a single I-V

acquisition (1 voltage cycle per second, and hence more than 1000 minutes for a full 256x256 pixel resolution I/V map). The first 3 data rows are based on measurement times per pixel that are more ambitious, but diminishingly feasible. Regardless, the corresponding acquisition times for a complete set of 256 by 256 pixels range from practically long (hours) to essentially unfeasible (full working day). Several disadvantages result, including susceptibility to thermal drift, inaccuracies for positioning actuators (hysteresis and creep), the possibility of sample modification, decay, and oxidation. There is an additional caveat as well, in that images are not simultaneously acquired with the point by point I-V spectra, and hence any sample or tip damage, or imprecision in the actual tip position, cannot be observed and especially corrected in real time.

Table I. Representative acquisition times for arrays of conventional (pixel by pixel) I-V spectra (top 4 data rows) acquired at rates ranging from impractical (row 1) to common (row 4), compared to parameters for NCM implementing multidimensional SPM (mSPM) with equivalent pixel resolution (last 4 data rows) for standard (row 5) to high-speed scanning (row 8).

Imaging Approach	practical pixel time (sec)	practical line rate (Hz)	frame time (min)	I/V-xyz image time (min)
pixel by pixel	0.04	9.77E-02	43.69	43.7
pixel by pixel	0.1	3.91E-02	109.23	109.2
pixel by pixel	0.4	9.77E-03	436.91	436.9
pixel by pixel	*1*	*3.91E-03*	*1092.27*	*1092.3*
mSPM	*3.91E-03*	*1*	*4.27*	*128.0*
mSPM	3.91E-04	10	0.43	12.8
hs-mSPM	9.77E-05	40	0.11	3.2
hs-mSPM	3.91E-05	100	0.04	1.3

These issues can be somewhat mediated by hardware and software solutions. Closed loop positioning in AFM can correct for actuator irregularities, though this cannot mitigate the common issue of independent thermal drift of the sample with respect to the tip. Of course, software-enabled feature tracking could correct for such drift, if regular image updates were available that is, unfortunately, not the case for pixel-by-pixel I-V spectra. Alternately,

specialized systems with high thermal stability are proven for maintaining the tip at a fixed position, demonstrated particularly in atomic-scale, UHV SPM work [37,38]. But all of these challenges generally persist for the far more widely employed ambient measurements with standard commercial hardware, and especially for legacy systems. The most commonly applied solution is therefore simply to acquire fewer I-V spectra in a given area of interest, thus still providing the valuable multidimensional data (*x, y, z, I,* and *V*), but with a corresponding (and generally highly deleterious) decrease in spatial resolution.

Accordingly, this work acquires high resolution multidimensional results (still *x, y, z, I*, and *V*), but by leveraging the primary forte of AFM, i.e. imaging, instead of a persistent challenge, i.e. parking the tip in a precisely known location. Specifically, numerous consecutive conductive AFM (c-AFM) images are acquired recording current *I* in the *x-y* planes, each with distinct voltage *V* bias, and then the stack of images are reassembled into a 3-d dataset of current versus area and voltage (Figure 5). The array of I-V curves, 65,536 of them for a standard 256 by 256 pixel stack of c-AFM images, can then easily be used to calculate and map properties for the imaged area with the same nanoscale spatial resolution inherent in the individual images. Voltage resolution is evidently determined by the number of image frames and the voltage span. Crucially, thermal drift problems become practically negligible within any single image as each frame is acquired in seconds to minutes instead of hours to many hours for point by point I-V acquisition. Feature tracking from one image to the next (real time or in post-processing) can also easily be employed, while tip or specimen damage can be directly observed and coped with in real time. This mSPM approach is therefore particularly suited for investigating nanostructured or heterogeneous electronic materials and devices, where conductivity may differ significantly over the probed area, demonstrated in this work for nanoscale conductance mapping

as well as simultaneously acquired maps of the "turn-on" switching voltages for micron sized areas of phase change thin films reflecting nanoscale area phase transitions.

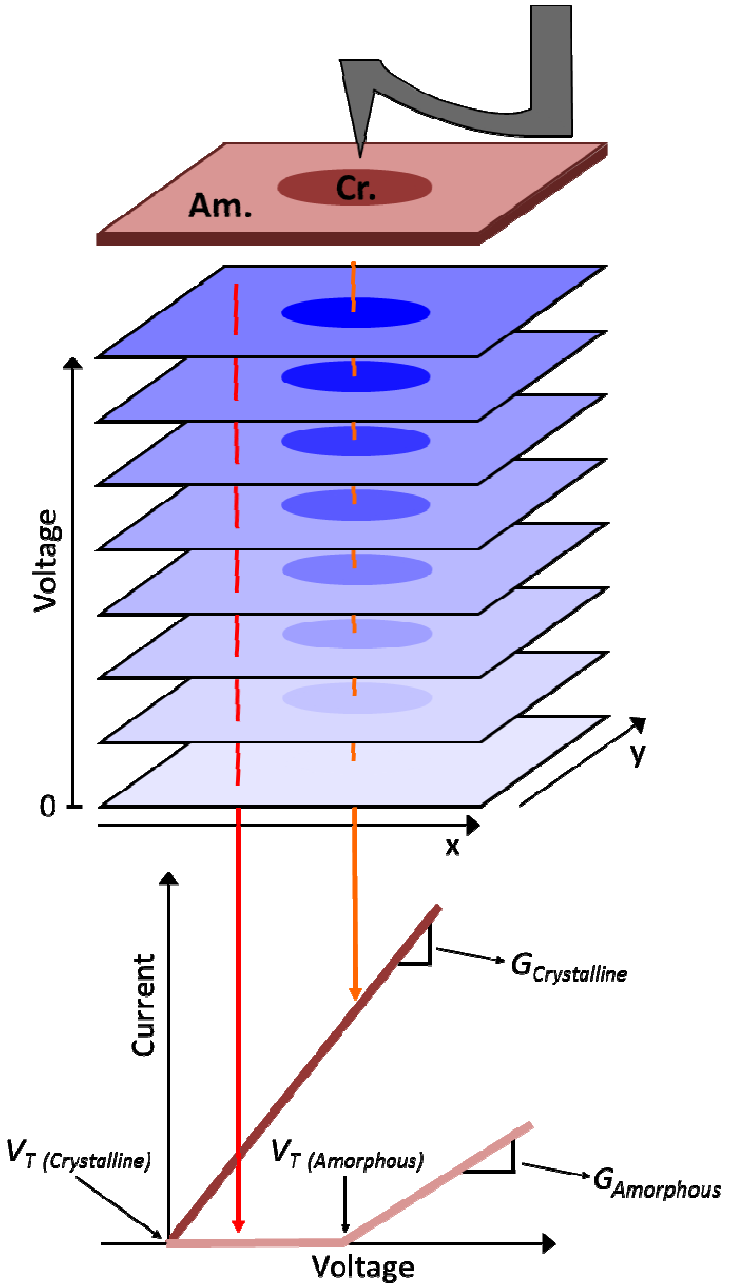

Figure 5: Sketch of Nanoscale Conductance Mapping (NCM) for a heterogeneous phase change memory thin film of GeSe. Consecutive conductive atomic force microscopy (c-AFM) images are acquired with incrementally higher applied voltages. Current versus voltage (I-V) curves are then extracted for each pixel to efficiently quantify and map local conductance properties.

Of course similar multidimensional stacks have been employed elsewhere, as it is relatively straightforward to automate changes in distinct imaging or sample parameters from one SPM scan to another. For example, phase and amplitude have been recorded during atomic scale AFM imaging, with each frame acquired at a different separation distance, yielding contrast related to the particular atom beneath the tip [39]. On a larger scale, multiple acoustic AFM images each with distinct ultrasonic excitation frequencies provided efficient maps of local contact stiffness [40], and recently consecutive friction images with decrementing normal loads yielded maps of the friction coefficient [41]. Current imaging tunneling spectroscopy (CITS) is the most closely related analog, implemented in scanning tunneling microscopy [42]. Since the base platform for the Nanocale Conductive Mapping (NCM) technique presented here is c-AFM, though, it is much more widely applicable than CITS. This is because it enables high spatial resolution maps of electronic transport in specimens with highly insulating regions, not just conductors, of increasing importance for real, nanostructured electronic devices. Furthermore, while NCM is applicable at any scanning speed, with any new or legacy AFM, the results presented here incorporate recent advances in high speed SPM. This enables not just results with negligible thermal drift, but highly efficient image acquisition as well, with obvious benefits for larger area detection, dynamic studies, and high throughput studies.

3.4. Standard Conductance Measurements

Figure 6(a) exemplifies a common application of AFM based current studies to a material with nanoscale heterogenous electronic properties. The specimen is a 50 nm thick amorphous GeSe layer, grown by thermal coevaporation on an underlying conducting back electrode of Pt [43] with a Si substrate. The GeSe film was determined to have the composition of $Ge_{51}Se_{49}$ (in atomic percent) from electron probe X-ray microanalysis. The specimen contains both

amorphous and crystalline phases, as shown in the topography image (Figure 6(b)), and a corresponding current map acquired while simply continuously biasing the scanned probe with $1.3V_{DC}$ (Figure 6(c)).

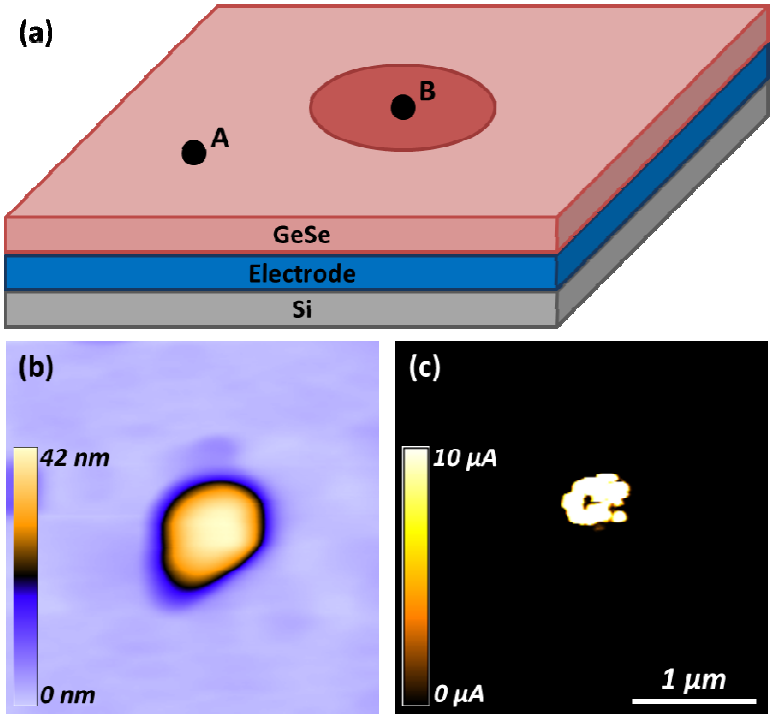

Figure 6: Sketch (a), AFM topography image (b), and standard c-AFM current image (c) of a model phase change specimen with a crystalline 'bit' (B) in the center of an amorphous (A) GeSe film.

Figure 7(a) presents standard c-AFM I-V curves acquired from a similar amorphous and crystalline region of the GeSe film, locations (A) and (B) respectively, as indicated in Figure 6(a). Both of the I-V curves were acquired by positioning the tip somewhere in the distinct specimen regions, then ramping the voltage from -2 V to +2 V and back with 5 mV steps at a cycle rate of 1 Hz. The current is sampled every ms, providing 500 current measurements in each direction. Note that the y-axes are in µS for the crystalline I-V spectra, and in nS for the amorphous location due to the profound difference in conductivity. The highly conducting crystalline phase actually reaches the upper and lower current acquisition limits (±10 µA) of the

c-AFM at +1.31 V and -1.60 V, respectively. Conversely, the current measured at the amorphous phase was typically 4 orders of magnitude less throughout the experiment. Imaging and acquiring I-V spectra and/or topographic images for such disparate phases with STM and/or CITS would be extraordinarily challenging, but with c-AFM it is thus relatively straightforward.

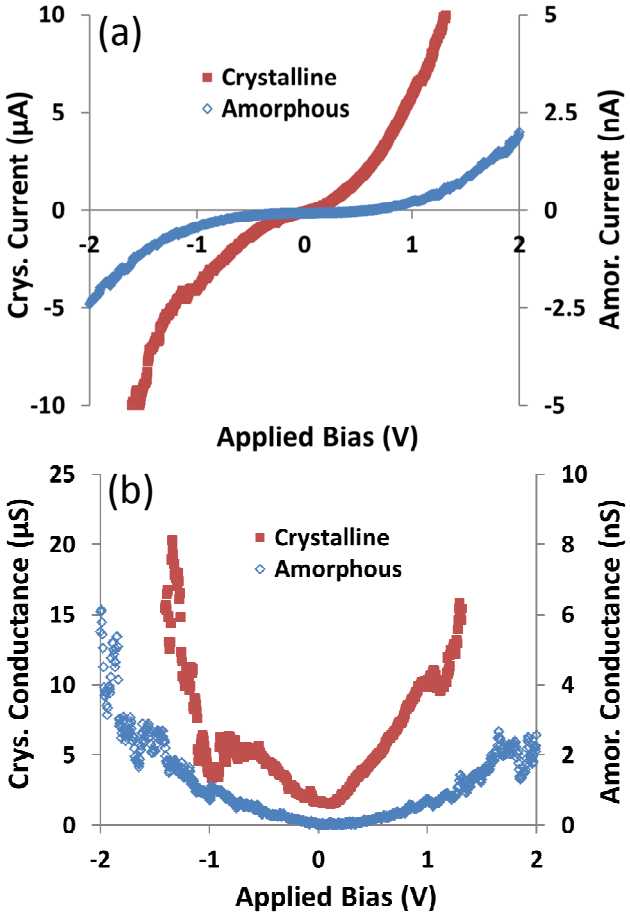

Figure 7: Standard I-V curves acquired at typical pixel-by-pixel rates (1 Hz) on crystalline and amorphous regions of a GeSe phase change film (a, note distinct scales at left and right). The conductance has also been calculated (b) for the crystalline and amorphous regions, respectively, revealing differences of 4 orders of magnitude (note scale difference).

The slope of the I-V curve is used to calculate the conductance at any applied voltage for both crystalline and amorphous phases, Figure 7(b). Due to conductance on the crystalline bit of almost 4 orders of magnitude greater than for the amorphous region, a maximum measured

conductance for the crystalline phase of 20.30 μS at -1.44 V, versus 5.26 nS at -1.94 V for the amorphous phase.

3.5. Nanoscale Conductance Mapping

The obvious challenge with simple I-V spectra such as in Figure 7 is that in order to spatially resolve nanoscale specimen features many hours are required to sequentially collect thousands of closely packed voltage sweeps, as exemplified in Table I. When implementing the mSPM technique for conductance mapping, on the other hand, the tip is simply continuously scanned, while the voltage is changed only occasionally and subtly (e.g. at the start of each new frame, by a small ΔV). Settling times are therefore completely avoided, providing extensive benefits even at moderate scanning speeds. For example, a single image frame when scanning with a 10 Hz line rates (Table I, data row 6) requires 25.6 seconds (0.43 minutes, data column 3), providing a full spatial resolution I/V-xyz map in only ~13 minutes for 30 consecutive images or voltage steps (data column 4). , This is compared to 109.2 minutes (i.e. 1.8 hours) for an extremely difficult to achieve rate of 10 pixels/second of I-V spectra (data row 2). Employing recent advances in high speed SPM [44], with line scanning rates up to thousands of Hz, allows even more impressive enhancements, literally requiring just 7.7 seconds at 1 kHz line rates for a sequence of 30 images, or 1.3 minutes at a more commonly manageable 100 Hz scanning rate, such that high spatial and voltage resolution I/V data is achieved by NCM.

Figure 8 displays a montage of 15 such c-AFM images extracted from a sequence of 30 consecutive scans, each with incremented voltages from 10 mV up to 300 mV as indicated. All of the frames are acquired in the same 1.5 μm x 1.5 μm area, with a moderate 10 Hz line scan rate equivalent to spending 391 μsec per pixel. Collectively this amounts to just 12.8 minutes to acquire all 65,536 I-V spectra with 30 voltage steps each. This amounts to an 85x improvement

when compared to the 1 Hz acquisition rate for a single pixel as displayed in Figure 7. To put this into better perspective, the 13 minute NCM experiment would require more than 18 hours to equivalently complete with traditional point by point I-V mapping.

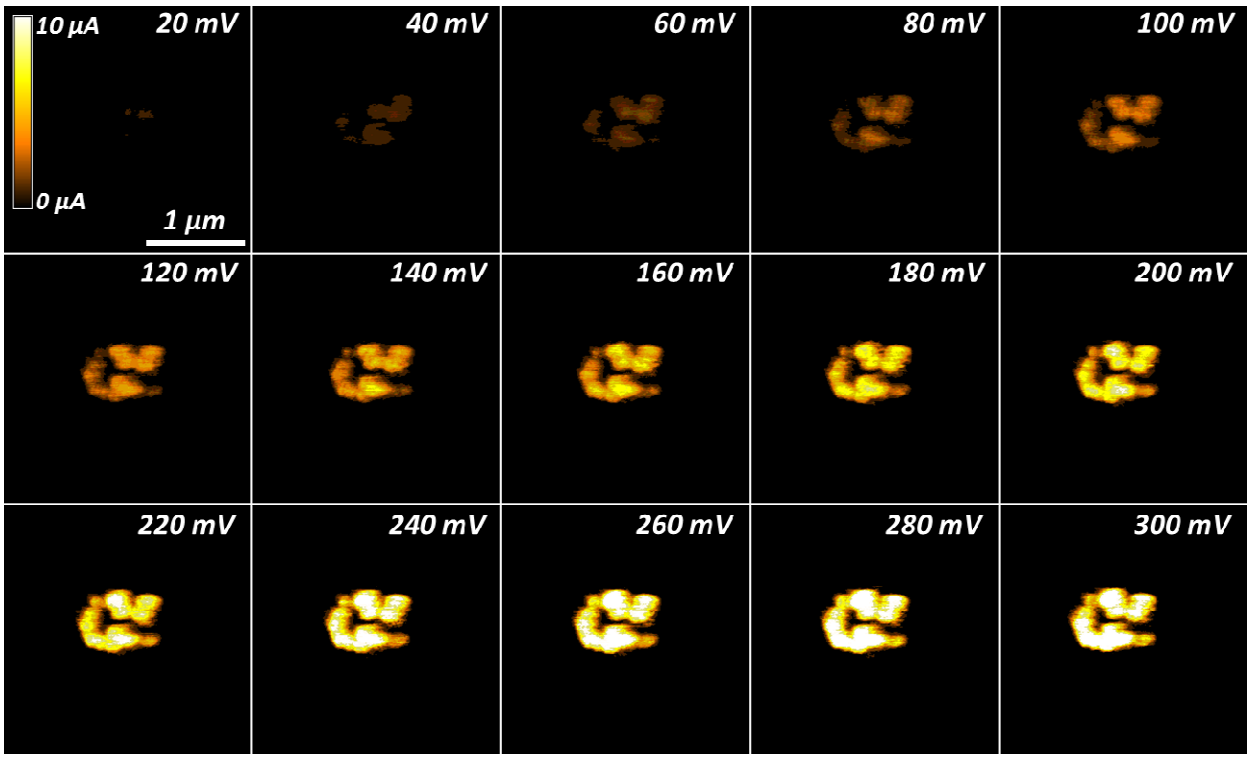

Figure 8: Montage of current images at distinct applied voltages as labeled, representing a subset of 30 total frames for the same 1.5 µm x 1.5 µm area, all imaged at a line rate of 10 Hz. The field of view displays a conducting crystalline region in an otherwise amorphous GeSe thin film.

Despite the minimal spatial drift offered by this higher speed approach compared to pixel-by-pixel based spectra, image-by-image drift naturally still occurs, at least to some extent. Therefore, before assembling I-V curves by stacking the frames of Figure 8, simultaneously acquired topographic data is used to align the individual frames based on image correlation functions in standard image processing software (e.g. ImageJ, NIH). The positions of each frame are consequently slightly shifted in *x* and/or *y* directions as needed, in this case by a maximum of 60 nm and 6 nm for the fast and slow scan directions, respectively. Practically, any locations

which are not imaged in every single frame are truncated from the final results, typically representing a few percent of image pixels around the image periphery (of course depending on the magnitude and direction of lateral drift throughout the experiment). Furthermore, such drift could also be minimized by real time scanning corrections with suitable software and closed loop scanners.

After such drift correction, the matrix of acquired I-V curves can be used to map a variety of transport properties for the specimen, providing both nanoscale spatial resolution, as well as high confidence in the positional accuracy of the corresponding I-V results. For example, a map of the conductance can be calculated by fitting the shape of each I-V curve, Figure 9(a), with pixel dimensions here of just 6 nm x 6 nm. Consistent with the standard current image of Figure 6(c), a higher conductivity is apparent in Figure 9(a) for the central crystalline bit as compared to the surrounding amorphous film. The random scatter in each I-V curve used to calculate the conductance is quantified in Figure 9(b and c), which respectively present the 95% confidence error and the coefficients of determination (R^2) for the conductance map. On average, the 95% confidence error amounts for less than 15% of the calculated conductance values. The average coefficient of determination for the conducting bit is 0.88 ± 0.11, clearly confirming the ohmic nature of the I/V response within the crystalline region over the voltage range considered (0-300 mV). However, other I-V relationships in the event of Schottky, thermionic, tunneling, or spin dependent conditions, could alternately be calculated, providing corresponding maps of such features of more complex local materials behavior.

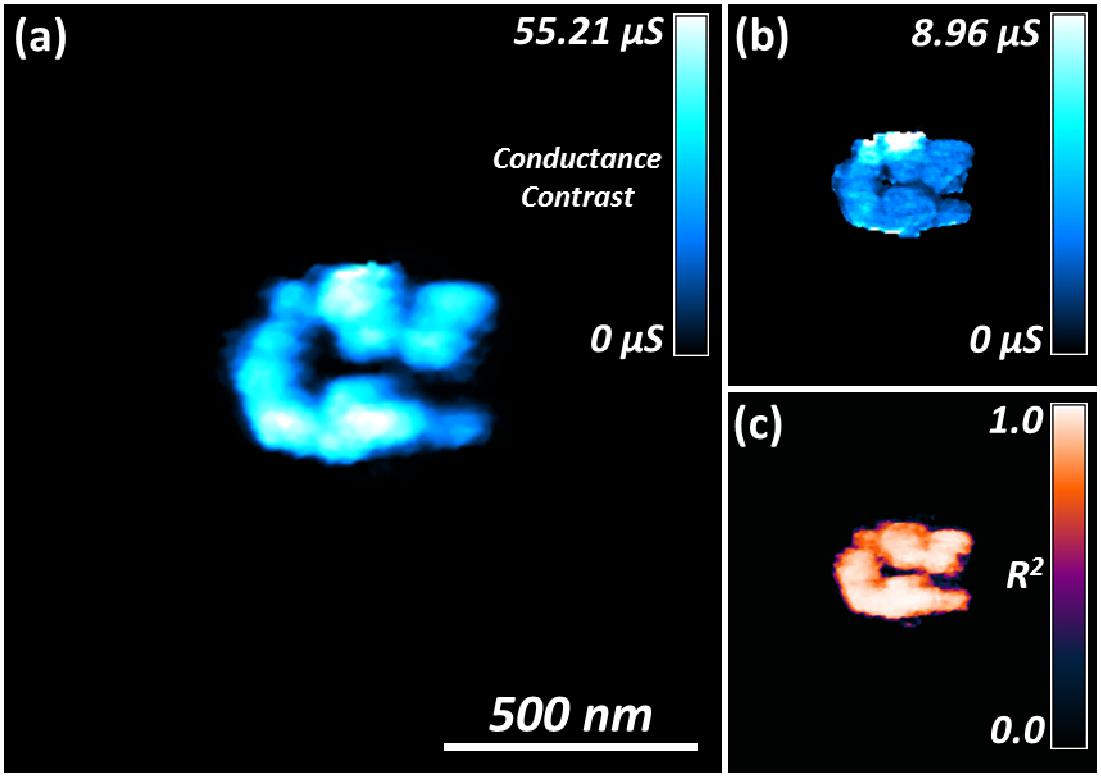

Figure 9: 1.39 µm x 1.49 µm map of conductance resolved down to 6 nm x 6 nm, based on 60,672 I-V curves from the dataset of Figure 8, all acquired by SPM in <13 minutes (a). The corresponding 95% confidence interval is also mapped (b), as is the coefficient of determination, R^2, for the measured conductance (c).

The acquired current with standard I-V spectra has been compared to the NCM method, Figure 10. I-V curves were acquired at ten spots on the crystalline bit. All ten I-V measurements were acquired within the marked dashed box of Figure 10(a). However, seven of the ten measurements were at the noise floor of the current detector, indicating that thermal drift pushed the probe into the amorphous region. The three I-V measurements with an appreciable current signal (true position on the crystalline bit) are presented as I-V Spot 1, 2, and 3 in the legend of Figure 10(b). Subsequent imaging was performed to construct the conductance map in Figure 10(a). The average conductances of the three standard I-V curves in Figure 10(b) are 112 ± 28 nS, 333 ± 44 nS, and 29 ± 18 nS. The average conductance of the I-V curve extracted from the NCM method is 605 nS ± 187 nS.

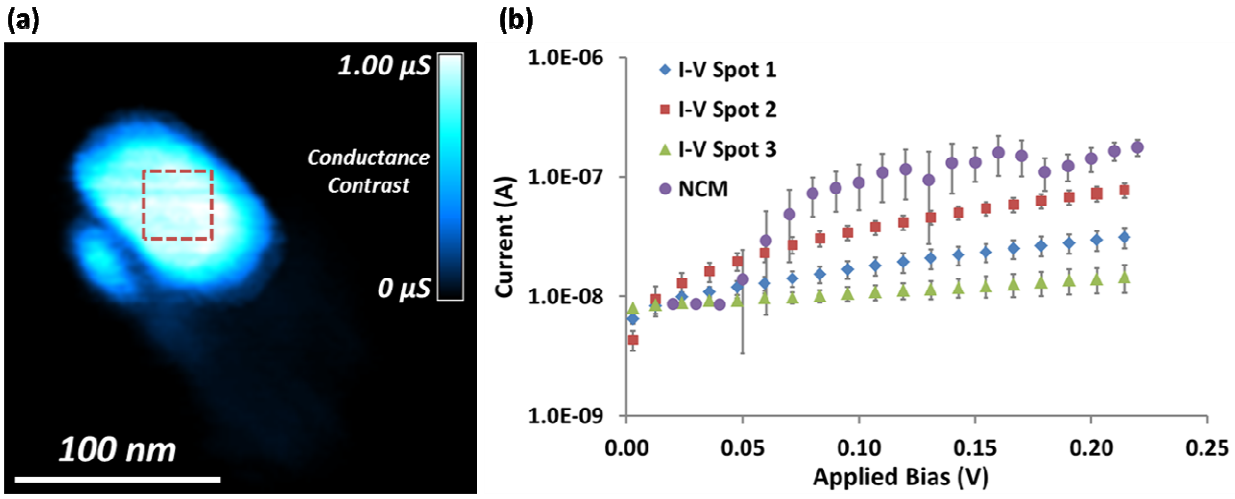

Figure 10: Subset of 312 nm x 329 nm map of conductance calculated from 23 c-AFM images with line scan rate of 10 Hz (a). Images were acquired from 0mV to 220 mV bias with 10mV steps. Current vs. applied bias for standard I-V curves and NCM extracted I-V curve of the crystalline bit (b). Standard I-V curves were acquired from -2 V to +2 V with 3 cycles at a 3 Hz ramp rate. The NCM I-V curve is an average of 20 x 20 pixels from the box in (a).

Due to the ~4 order of magnitude difference in conductance between the crystalline and amorphous phases, it was impractical to simultaneously resolve both the subtle conductivity variations within the amorphous phase, and the maximum conductivity in the crystalline phase. Separate results have thus been acquired in the same manner, but with the current detector set at its highest sensitivity (5 pA to 10 nA), in order to investigate the amorphous phase of the GeSe film alone, with no crystalline bit present. Figure 11 displays a montage of 10 c-AFM images extracted from a complete sequence of 19 consecutive scans, each with incremented voltages from 0 V up to 3.6 V (only those up to 1.8 V are shown). All images have been acquired from the same 4 µm x 4 µm region. A modest 10 Hz line scan rate was implemented for all acquired images, as with Figure 8. The total linear drift was just 16 nm and 86 nm in the fast and slow scan directions, respectively, leading to a final conductance map with 65,280 points (237 by 254 pixels).

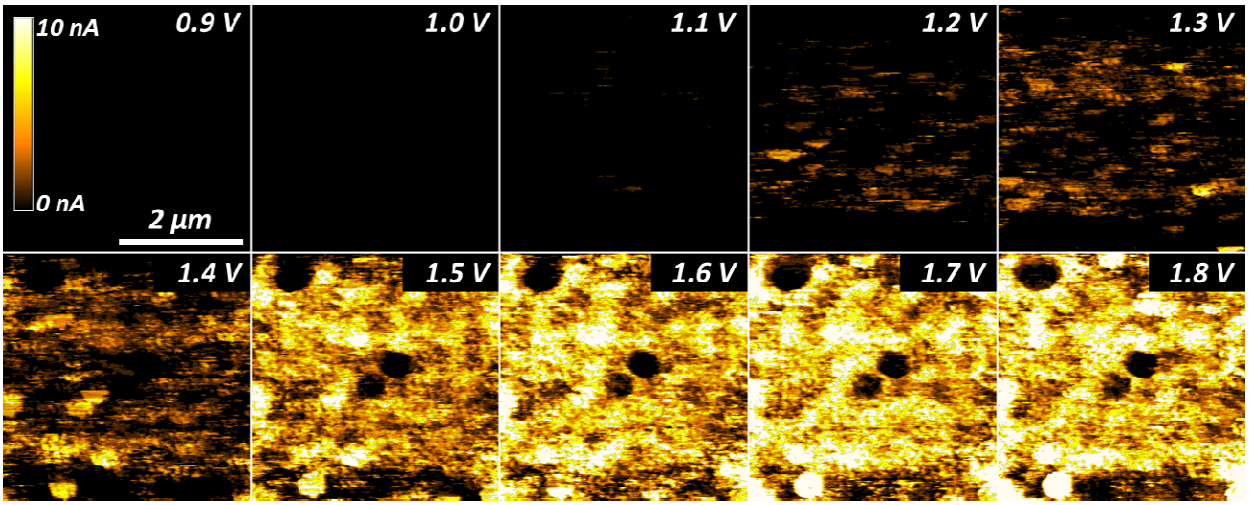

Figure 11: Montage of current images at distinct applied voltages as labeled, representing a subset of 19 total frames for the same 4.0 µm x 4.0 µm area, all imaged at a line rate of 10 Hz. The field of view displays the amorphous GeSe thin film with no crystalline bit present.

Interestingly, unlike the crystalline phase, we found that the amorphous phase does not conduct current appreciably until a spatially dependent threshold "turn-on" voltage is reached, Figure 12(a). This turn-on voltage is characteristic of traditional semiconductor behavior [45,46], and is easily determined from the I-V curves extracted from each pixel of Figure 11. Figure 12(b) displays a map of the corresponding conductance map of the amorphous GeSe film, calculated based on the I-V slope beyond the turn-on voltage only (thus avoiding artificial offsets in the conductance due to varying "turn-on" potentials). As suggested by the early frames in the Figure 11 montage, the turn-on voltage can be as low as 1.1 V within the amorphous film. For some regions, however, no current was detected even during the maximum applied bias of 3.6 V, indicating an even stronger local turn-on voltage. This ability to map local electronic transport is clearly important for applications such as resistive or phase change data storage systems, where uniformity from one nanoscale bit to another will be crucial in terms of ultimate operating speeds, power requirements, and reliability.

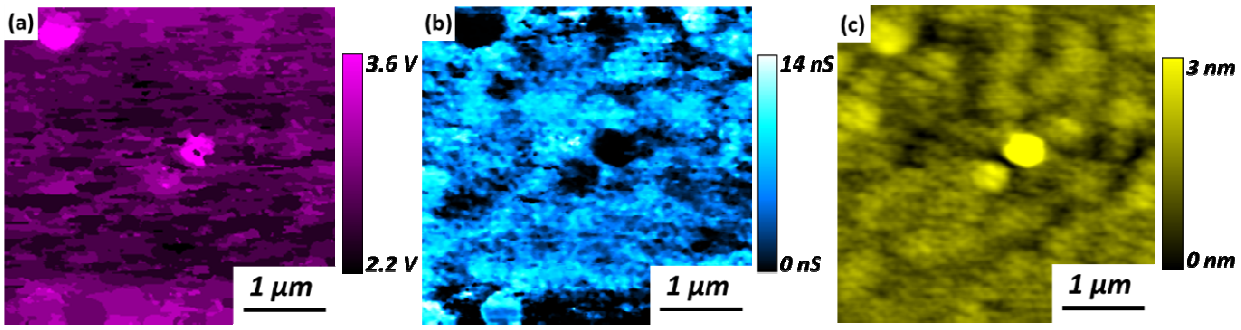

Figure 12: 3.98 µm x 3.83 µm map of the 'turn-on' voltage for an amorphous GeSe film, based on 65,280 I-V curves from the dataset of Figure 11, all acquired by SPM in just 8 minutes (a). The corresponding conductance (b) and topography (c) is also shown, resolved down to 16 nm x 16 nm.

Of course, such spatial resolution might not be achieved using traditional I-V methods, in which case the mean response of many I-V spectra, and/or a histogram, would typically be reported. Similar histograms from the NCM conductance maps are shown for the crystalline, and separately the amorphous phases, Figure 13(a-b). The mean conductance for the crystalline region alone in Figure 9(a) is 25.0 ± 15.9 µS, while the mean conductance for the amorphous film in Figure 12 is 5.0 ± 2.9 nS. As expected from the standard I-V curve measurements, the crystalline phase has a conductance that is more than 3 orders of magnitude higher than the amorphous phase. As with all histogram analyses, the relative ratio and distribution of properties can thus be visualized, for example to assess a relative areal fraction of switched material when normalized by the analyzed area. With the new NCM approach presented here, though, such distributions of conductivity behavior can now also be precisely coupled spatially to various nanoscale specimen features, providing valuable benefits for heterogeneous specimens in general.

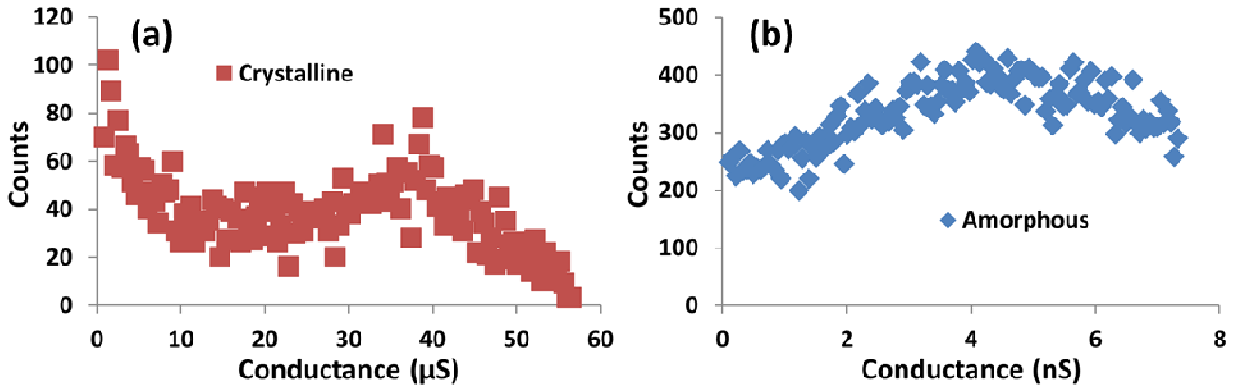

Figure 13: Histograms of local conductance values from the crystalline region in Figure 9(a), and the amorphous region in Figure 12.

3.6. Conductance Mapping Artifacts

While applying the NCM approach as well as any of the other AFM-based current measurement schemes, there are several possible artifacts that one must consider. First, it is critical that the tip maintain a constant applied normal load (i.e. contact or setpoint force). Varying this applied normal load from location to location could cause the contact area to change [40], possibly causing the detected current to shift higher or lower than anticipated [3] especially if the correlation between contact area and current is non-linear [47,48]. Even more critical, though, is that this constant force should be both high enough to produce a consistent current measurement (generally sufficient to push through any surface contamination), while remaining reasonable such that the tip and/or specimen are not plastically deformed or modified. Fortunately, negligible variations in image quality and feature size/shape have been documented over each set of images on the GeSe film. This suggests that the scanning conditions are stable and nondestructive. These conditions are apparent in the consecutive images depicted in Figure 8 and Figure 11, as sub-20 nm features are consistently resolved.

The second possible common artifact is due to changes in contact area during scanning related to topographic features or regions with dramatically different mechanical properties. This latter

concern is negligible for the GeSe specimens considered here, as the amorphous and crystalline regions are uniformly stiff versus the comparatively compliant AFM probe. With polymer specimens, however, such variations must rigorously be accounted for. General topographic variations, on the other hand, are ubiquitous in AFM imaging, most apparent here when comparing the amorphous GeSe current maps of Figure 11 with the local topography (Figure 12(c)). Areas with higher topography consistently display a lower current then their lower topographic counterparts, likely due to the decreased contact area between the tip and local convex surface. Consistent with this observation, local areas of the sample that are concave with spatial dimensions similar to the probe tend to display a higher relative measured current. These contact area effects are unavoidable in I-V detection and c-AFM, but can be diminished by utilizing sharper AFM probes.

The third potential artifact with current or conductance mapping concerns specimen stability. Certain specimens are susceptible to oxidation, thermal variations, and humidity (or lack thereof). The water meniscus that develops at the tip sample junction for ambient measurements influences current measurements as well via the relative contact area [49] and can even lead to electrochemical reactions. The efficient frame-by-frame approach of NCM, especially if leveraging high speed SPM, minimizes this issue by making the measurements faster (with less time for oxidation or humidity variations to intercede). Moreover, any specimen changes that do occur due to the environment negligibly influence the I-V response from one pixel to another, since the sample state is essentially identical for every single pixel for a single image (at a single voltage). Of course, such environmental effects can still shift the magnitude of the measured current for every pixel in any given image (voltage), with the current response for the final image frames sampling a possibly environmentally damaged surface while the initial specimen may be

pristine. If such 'drift' in the environmental response is uniform, though, then it can easily be corrected. Moreover, it is trivial to test for such effects by comparing single I-V spectra acquired before and after NCM maps. Pixel-by-pixel spectra, on the other hand, can be extremely problematic in such circumstances since the first pixel measured at one corner of an area may be for an ideal specimen, while the last pixel from the opposite corner may be after substantial specimen degradation, requiring much more challenging pixel-dependent corrections. Regardless, to alleviate any such artifacts for the results presented here on GeSe films, all data was acquired while the experimental chamber was continuously purged with Argon.

In a related sense, simple voltage sweeps can be damaging to the region beneath the probe for some specimens, possibly influencing nearby regions as well through percolation paths, charging, or even breakdown events. Scanned instead of pixel-by-pixel I-V data therefore presents an additional benefit, for example through images with consecutively stronger voltages, because any breakdown events at certain pixels do not completely hinder future I-V spectra for adjacent pixel measurements—spectra for all pixels (at least to the same maximum voltage) have already been acquired. NCM results are correspondingly more comparable to macroscopic I-V measurements of practical devices, where the ensemble behavior of adjacent regions, especially their inter-related response, defines the overall device properties.

Since updated topographic and current maps are continuously acquired with NCM, the influence of any of the artifacts discussed above can additionally be observed in real time. Experimental parameters can then easily be corrected, measurements restarted, or details modified. Sample, tip, or system problems are substantially more difficult to identify and/or correct during consecutive pixel-by-pixel acquisition of I-V spectra.

3.7. Conclusion

Nanoscale Conductance Mapping (NCM) is an important tool for efficiently mapping electronic transport in heterogeneous materials with nanoscale resolution. It is inherently more efficient than pixel-by-pixel I-V acquisition schemes, particularly when implemented leveraging high speed SPM. Here it is employed to map electron transport for crystalline and amorphous phases of a GeSe phase change film. As confirmed with single I-V spectra, the mapped conductance for the crystalline phase is more than 3 orders of magnitude stronger than the amorphous phase. Meanwhile, the amorphous region exhibits variations in conductance, and separately an effective "turn-on" voltage, that are spatially independent. NCM is therefore promising for investigating the influence of phases, defects, interfaces, and/or topographic features on electronic transport in heterogeneous materials, particularly those with highly varying conductivity regions such as MEMS/NEMS devices, phase change memories, and nanostructured photovoltaics.

3.8. Experimental

All experiments are performed at room temperature with an Asylum Research Cypher AFM. The specimen is enclosed in the scanning chamber with a constant flow of Argon gas at 20 CFH to minimize specimen oxidation and provide a constant water meniscus at the tip/specimen junction. Current detection is performed with an Asylum Research ORCA cantilever holder, which features a dual gain current sensitivity of 1 μA/V (low gain) and 1 nA/V (high gain). The current resolution for the low and high gain is 1 nA and 5 pA, respectively.

Diamond coated silicon cantilevers (Nanosensors, CDTP-NCHR) are employed throughout, with a quoted tip length of 10-15 μm, cantilever length of 125 ± 10 μm, and resonant frequency of 275-720 kHz.

The amorphous GeSe film was prepared by chemical vapor deposition in a plasma discharge stainless steel reactor on a conducting back electrode. Both the amorphous GeSe film and back electrode were deposited on a silicon wafer for mechanical stability. A low pressure plasma was created by an rf discharge between two parallel plate electrodes, where both silicon substrates were fixed. The precursor gases used for the deposition were GeH_4 and H_2Se, and deposition was continued until a GeSe film thickness of 50 nm [50].

For the "turn-on" voltage map of the amorphous GeSe film in Figure 12(a), the calculated threshold voltage corresponds to when the current rises above 100 pA. This is approximately 20 times higher than the noise floor of the high gain detector.

3.9. References

1. G. Binnig, C. F. Quate, and C. Gerber, Physical Review Letters **56** (9), 930 (1986).
2. P. Fiorenza, R. Lo Nigro, V. Raineri, and D. Salinas, Microelectron Eng **84** (3), 441 (2007).
3. P. Dewolf, J. Snauwaert, T. Clarysse, W. Vandervorst, and L. Hellemans, Applied Physics Letters **66** (12), 1530 (1995).
4. C. Shafai, D. J. Thomson, M. Simardnormandin, G. Mattiussi, and P. J. Scanlon, Applied Physics Letters **64** (3), 342 (1994).
5. K. N. Chappanda and M. Tabib-Azar, presented at the Sensors, 2011 IEEE, 2011 (unpublished).
6. A. Bayerl, M. Lanza, M. Porti, F. Campabadal, M. Nafria, X. Aymerich, and G. Benstetter, Microelectron Eng **88** (7), 1334 (2011).
7. H. R. Moutinho, R. G. Dhere, C. Ballif, M. M. Al-Jassim, and L. L. Kazmerski, J Vac Sci Technol A **18** (4), 1599 (2000).
8. B. Alperson, S. Cohen, I. Rubinstein, and G. Hodes, Physical Review B **52** (24), 17017 (1995).
9. B. J. Leever, M. F. Durstock, M. D. Irwin, A. W. Hains, T. J. Marks, L. S. C. Pingree, and M. C. Hersam, Applied Physics Letters **92** (1) (2008).
10. B. D. Huey, D. Lisjak, and D. A. Bonnell, J Am Ceram Soc **82** (7), 1941 (1999).
11. B. D. Huey and D. A. Bonnell, Solid State Ionics **131** (1-2), 51 (2000).
12. B. D. Huey and D. A. Bonnell, Applied Physics Letters **76** (8), 1012 (2000).
13. Haeri Kim, Seungbum Hong, and Dong-Wook Kim, Applied Physics Letters **100** (2) (2012).
14. Hyoungsoo Ko, Kyunghee Ryu, Hongsik Park, Chulmin Park, Daeyoung Jeon, Yong Kwan Kim, Juhwan Jung, Dong-Ki Min, Yunseok Kim, Ho Nyung Lee, Yoondong Park, Hyunjung Shin, and Seungbum Hong, Nano Letters **11** (4), 1428 (2011).

15. B. J. Bae, S. H. Hong, S. Y. Hwang, J. Y. Hwang, K. Y. Yang, and H. Lee, Semicond Sci Tech **24** (7) (2009).
16. S. Gidon, O. Lemonnier, B. Rolland, O. Bichet, C. Dressler, and Y. Samson, Applied Physics Letters **85** (26), 6392 (2004).
17. T. Gotoh, K. Sugawara, and K. Tanaka, Jpn J Appl Phys 2 **43** (6B), L818 (2004).
18. H Wong, Simone Raoux, SangBum Kim, Jiale Liang, John P Reifenberg, Bipin Rajendran, Mehdi Asheghi, and Kenneth E Goodson, Proceedings of the IEEE **98** (12), 2201 (2010).
19. C. D. Wright, M. Armand, and M. M. Aziz, Ieee T Nanotechnol **5** (1), 50 (2006).
20. H. F. Hamann, M. O'Boyle, Y. C. Martin, M. Rooks, and K. Wickramasinghe, Nat Mater **5** (5), 383 (2006).
21. D. L. Klein and P. L. Mceuen, Applied Physics Letters **66** (19), 2478 (1995).
22. F. Hauquier, D. Alamarguy, P. Viel, S. Noel, A. Filoramo, V. Huc, F. Houze, and S. Palacin, Appl Surf Sci **258** (7), 2920 (2012).
23. N. Gosvami, K. H. A. Lau, S. K. Sinha, and S. J. O'Shea, Appl Surf Sci **252** (11), 3956 (2006).
24. M. Schloffer, C. Teichert, P. Supancic, A. Andreev, Y. Hou, and Z. H. Wang, J Eur Ceram Soc **30** (7), 1761 (2010).
25. H. J. Lee, J. Lee, and S. M. Park, J Phys Chem B **114** (8), 2660 (2010).
26. D. A. Bussian, J. R. O'Dea, H. Metiu, and S. K. Buratto, Nano Letters **7** (2), 227 (2007).
27. A. Alexeev, J. Loos, and M. M. Koetse, Ultramicroscopy **106** (3), 191 (2006).
28. T. W. Kelley and C. D. Frisbie, J Vac Sci Technol B **18** (2), 632 (2000).
29. G. Binnig, H. Rohrer, Ch Gerber, and E. Weibel, Physical Review Letters **49** (1), 57 (1982).
30. M. Salmeron, D. F. Ogletree, C. Ocal, H. Wang, x, C, G. Neubauer, W. Kolbe, and G. Meyers, Journal of Vacuum Science & Technology B: Microelectronics and Nanometer Structures **9** (2), 1347 (1991).
31. M. C. Hersam, A. C. F. Hoole, S. J. O'Shea, and M. E. Welland, Applied Physics Letters **72** (8), 915 (1998).
32. H. N. Lin, H. L. Lin, S. S. Wang, L. S. Yu, G. Y. Perng, S. A. Chen, and S. H. Chen, Applied Physics Letters **81** (14), 2572 (2002).
33. P. De Wolf, R. Stephenson, T. Trenkler, T. Clarysse, T. Hantschel, and W. Vandevorst, J Vac Sci Technol B **18** (1), 361 (2000).
34. H. R. Moutinho, R. G. Dhere, C. S. Jiang, M. M. Al-Jassim, and L. L. Kazmerski, Thin Solid Films **514** (1–2), 150 (2006).
35. Y. Otsuka, Y. Naitoh, T. Matsumoto, and T. Kawai, Jpn J Appl Phys 2 **41** (7A), L742 (2002).
36. Elena T. Herruzo, Hitoshi Asakawa, Takeshi Fukuma, and Ricardo Garcia, Nanoscale **5** (7), 2678 (2013).
37. W. Allers, A. Schwarz, U. D. Schwarz, and R. Wiesendanger, Review of Scientific Instruments **69** (1), 221 (1998).
38. Boris J. Albers, Marcus Liebmann, Todd C. Schwendemann, Mehmet Z. Baykara, Markus Heyde, Miquel Salmeron, Eric I. Altman, and Udo D. Schwarz, Review of Scientific Instruments **79** (3), 033704 (2008).
39. M. Z. Baykara, T. C. Schwendemann, E. I. Altman, and U. D. Schwarz, Adv Mater **22** (26-27), 2838 (2010).

40. B. D. Huey, Annual Review of Materials Research **37**, 351 (2007).
41. James L. Bosse, Sungjun Lee, Bryan D. Huey, Andreas S. Andersen, and Duncan S. Sutherland, Small (2013).
42. W. Ho, J Chem Phys **117** (24), 11033 (2002).
43. D. S. Jeong, H. Lim, G. H. Park, C. S. Hwang, S. Lee, and B. K. Cheong, Journal of Applied Physics **111** (10) (2012).
44. L. M. Picco, L. Bozec, A. Ulcinas, D. J. Engledew, M. Antognozzi, M. A. Horton, and M. J. Miles, Nanotechnology **18** (4) (2007).
45. A. M. Cowley, Journal of Applied Physics **37** (8), 3024 (1966).
46. HC Card and EH Rhoderick, Journal of Physics D: Applied Physics **4** (10), 1589 (2002).
47. WA Keenan, PA Schumann, AH Tong, and RP Phillips, presented at the The Electrochemical Society, 1969 (unpublished).
48. H. K. Henisch, Journal of The Electrochemical Society **103** (11), 637 (1956).
49. A. L. Weisenhorn, P. Maivald, H. J. Butt, and P. K. Hansma, Physical Review B **45** (19), 11226 (1992).
50. E. Márquez, P. Nagels, J. M. González-Leal, A. M. Bernal-Oliva, E. Sleeckx, and R. Callaerts, Vacuum **52** (1–2), 55 (1999).

Chapter 4: Multidimensional SPM Applied for Spectroscopic Piezoresponse Force Microscopy

4.1. Abstract

Based on the multidimensional Nanoscale Conductance Mapping (NCM) approach in Multidimensional SPM Applied for Nanoscale Conductance Mapping, spectroscopic Piezoresponse Force Microscopy (sPFM) is used to investigate the electromechanical properties of heterogeneous piezoelectric materials. The technique employs a sequence of piezoresponse force microscopy images, acquired in a single area, but with incrementally higher applied frequency. This generates a matrix of amplitude versus frequency spectra, providing nanoscale maps of the maximum amplitude and resonant frequency for adjacent grains in a polycrystalline film. The technique has been demonstrated for a $BaTiO_3$ thin film, with results similar to those acquired by point-by-point measurements, but acquired with higher spatial resolution and less spatial drift. Unlike other methods, the sPFM technique does not require additional hardware for the constant resonant peak tracking capabilities. It is therefore promising for investigating the electromechanical properties of heterogeneous materials used in capacitors and memory applications.

4.2. Introduction

The electromechanical and electrostatic properties of piezoelectric materials have been characterized with several modes of atomic force microscopy for the past two decades. These include both noncontact methods such as electrostatic force microscopy (EFM) [1] and scanning surface potential microscopy (SSPM) [2], as well as contact methods such as piezoresponse force microscopy (PFM) [3-5]. These techniques are implemented to understand the structure-

processing-property relationship for optimized electronic device design. Such investigations are relevant to ferroelectric memory or data storage systems [6], capacitors, and in more recent applications, ferroelectric tunnel junctions [7,8], and photovoltaics [9,10]. In these devices, the nanoscale spatial distribution in the electromechanical response is critical for their operation, and may be difficult to fully characterize with traditional piezoresponse force microscopy (PFM) methods. In specific applications, spatially mapping the magnitude of the electromechanical response (piezoelectric amplitude) on the nanoscale is required for performance considerations. With standard PFM characterization, an AC bias is applied across the sample with a constant amplitude (no modulation) and constant frequency (ideally at resonance). The electromechanical response will result in picometer scale oscillation of the sample, which is captured in the AFM cantilever deflection signal. A lock-in amplifier can be used to extract these small oscillations from the deflection signal, provided that a reference frequency is provided. The magnitude of the amplitude signal from the lock-in amplifier is directly related to the magnitude of the piezoelectric effect, which can be used to determine grain boundary locations and performance within each grain. The topography (Figure 14(a)) and PFM (Figure 14(b)) image for a $BaTiO_3$ sample is presented, demonstrating the variation in the piezoresponse in the *x*-*y* plane.

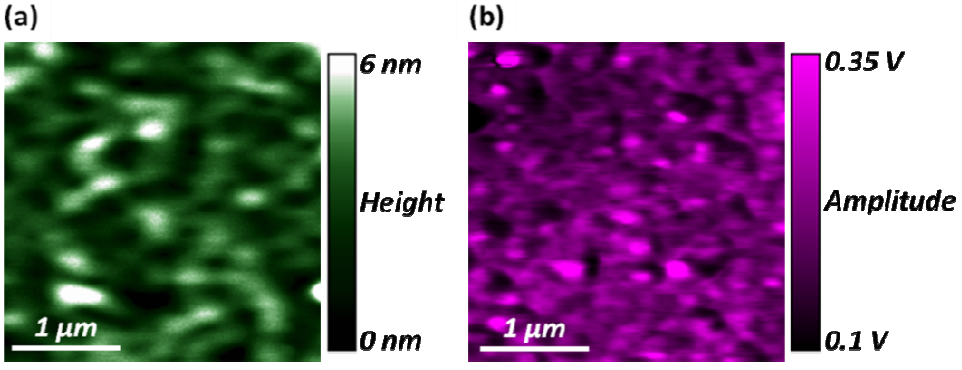

Figure 14: AFM topography (a) and PFM (b) image of a $BaTiO_3$ ferroelectric thin film, acquired at 1.73 MHz (10 Hz line scan rate, $2V_{PP}$ AC bias, 0V DC bias). The frequency is at the resonant peak for only some grains (not for all), which is a disadvantage of traditional PFM imaging.

Unfortunately, the standard PFM imaging method does not capture the entire picture in terms of performance. The magnitude of the first harmonic component of cantilever deflection is maximized when the measurement is taken at the contact resonant peak for the tip/sample combination. For a homogeneous material, this may be approximately constant over a typical imaged area. However, for heterogeneous films, such as a polycrystalline piezoelectric film, the resonant peak and corresponding piezoresponse amplitude for the tip/sample combination may vary with grain orientation or other factors [11,12]. This issue is well known, and the resonant frequency of each grain may be determined by collecting amplitude-*vs.*-frequency spectra (i.e. "frequency sweeps") where the AFM tip is engaged without scanning, and the piezoelectric amplitude is recorded as the frequency is swept between a lower and upper limit specified by the operator. Although this method sacrifices the inherent imaging capabilities of the AFM, it can be recovered by collecting more frequency sweeps after repositioning the probe and acquiring spectra across an area of interest. Unfortunately, the precise locations of these spectra acquired in a pixel by pixel fashion are not at the precise location one would expect, due to thermal drift in the AFM system [13]. Additionally, this approach may take much longer to acquire, as pixel by pixel frequency acquisition is not incorporated into standard software for AFM operation.

Accordingly, this work acquires high resolution multidimensional results (still *x, y, z,* amplitude, and frequency), but leverages the primary rastering/imaging quality of AFM. Specifically, numerous consecutive PFM images are acquired recording piezoelectric amplitude in the *x-y* planes, each with distinct frequencies, and then the stack of images are reassembled into a 3-d data set of amplitude versus area and frequency (Figure 15). The array of frequency sweeps, 65,536 for a standard 256 by 256 pixel stack of PFM images, can then be used to calculate the maximum piezoelectric amplitude and corresponding frequency for the imaged area, with the

same nanoscale spatial resolution as the individual images. The resolution of the frequency is determined by the number of image frames and the frequency span. With the following method, thermal drift problems become practically negligible within any single image as each frame is acquired in seconds to minutes. Feature tracking from one image to the next (usually in topography) can be applied to correct for the nanometer scale thermal drift between each image frame. This multidimensional SPM approach is therefore suited for investigating heterogeneous piezoelectric materials and devices, where the electromechanical response may vary the imaged area.

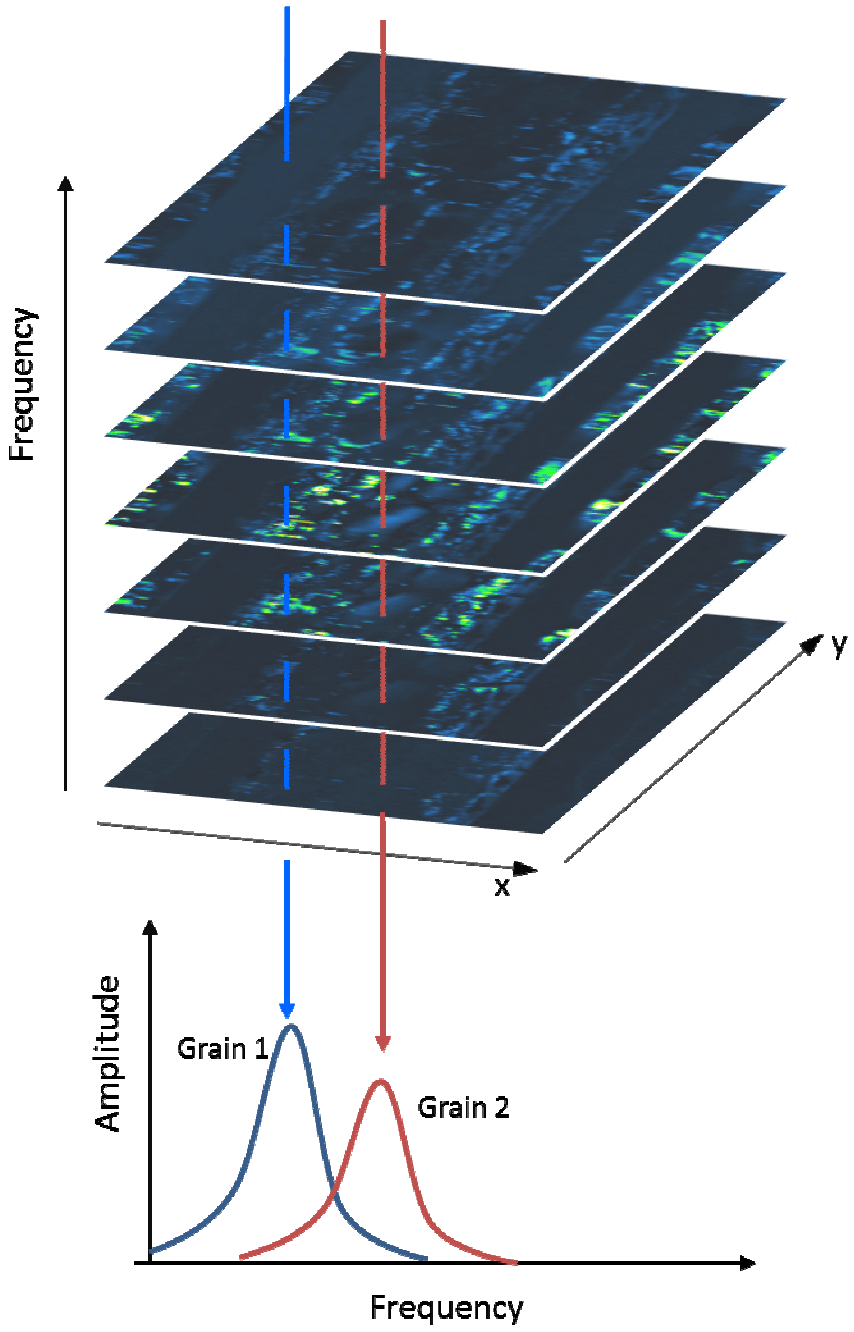

Figure 15: Sketch of spectroscopic Piezoresponse force microscopy (sPFM) technique for a heterogeneous, polycrystalline piezoelectric thin film. Consecutive PFM images are acquired with incrementally higher applied frequency. Amplitude versus frequency plots ("frequency sweeps") are then extracted for each pixel to efficiently quantify the maximum piezoelectric amplitude and corresponding resonance frequency.

4.3. Spectroscopic Piezoresponse Force Microscopy

Prior to acquiring a series of images for the sPFM technique, the upper and lower frequency limits must be defined. To determine this frequency range, without having either too few/many images or too small/large of a frequency increment, a frequency sweep was performed at a single point to determine the approximate piezoelectric response of the cantilever/sample combination. The resonant peak at this point was centered at 1.73 - 1.74 MHz, with a 100 kHz width. For the sPFM experiment, the frequency range and increment was selected as 1.50 - 1.85 MHz and 10 kHz, respectively.

Figure 16 displays a montage of 12 PFM images extracted from a sequence of 36 consecutive scans, each with incremented frequency from 1.66 MHz to 1.77 MHz as indicated. All of the image frames were acquired in the same 3 μm x 3 μm area, with a 10 Hz line scan rate. Each frame has also been corrected for drift by stacking and aligning to simultaneously acquire topographic data using image correlation functions in image processing software (Image J, NIH). The position of each frame is shifted in the x and/or y direction, with a maximum for this data set of 715 nm and 645 nm for fast and slow scan directions, respectively. The stack of image frames was truncated from a 256 x 256 pixel area down to 194 x 200 pixels as a result of the drift correction. Each frequency sweep matrix as a function of area was analyzed (National Instruments LabVIEW) to determine the maximum piezoresponse amplitude, Figure 17(a), and the corresponding frequency, Figure 17(b). These extracted parameters have been displayed in the form of a map, with spatial resolution of 12 nm per side. The piezoresponse amplitude at the resonance peak for each grain in the $BaTiO_3$ film is 0.221 ± 0.044 V (106 ± 21 pm), and the resonance peak varies by 80 kHz. These results are expected, and demonstrate sPFM's unique ability to measure the local variations in the piezoelectric response of heterogeneous materials.

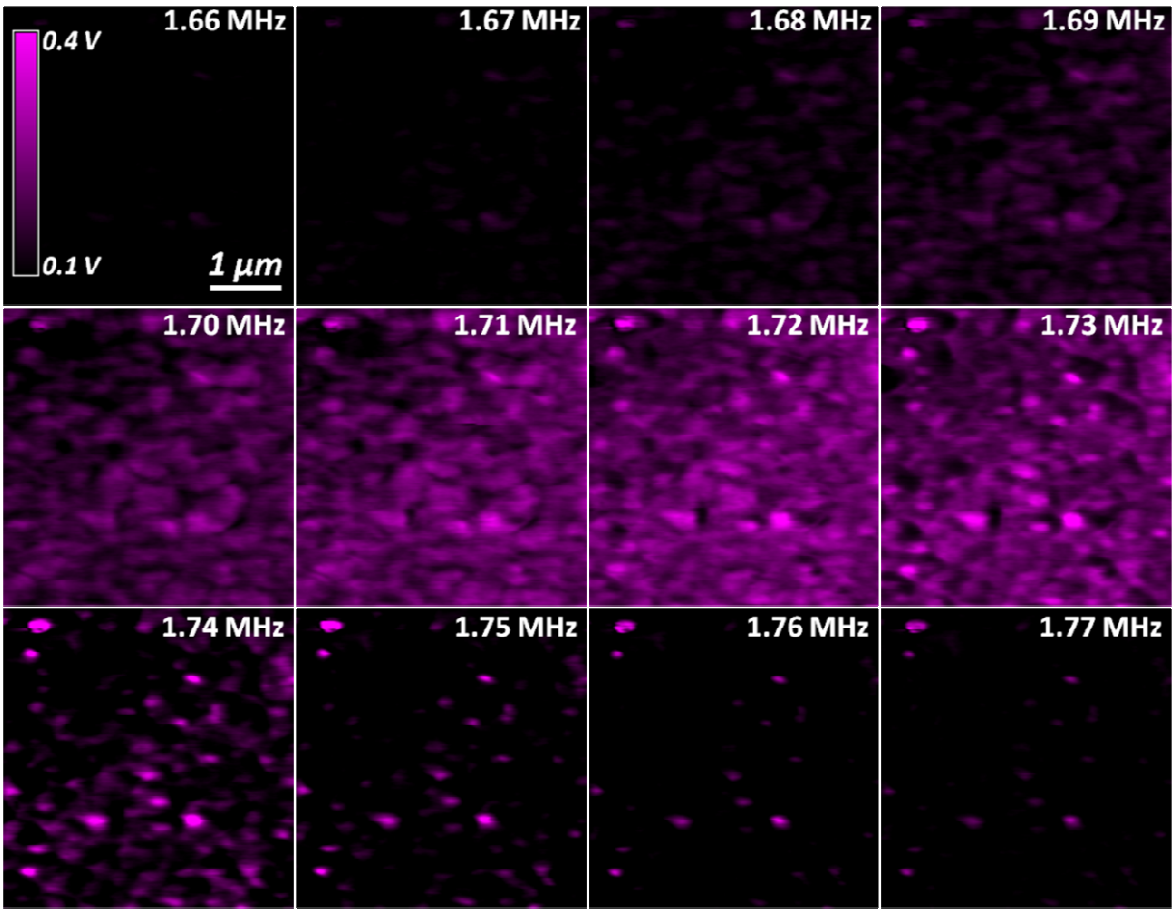

Figure 16: Montage of PFM images at distinct applied frequencies as labeled, representing a subset of 36 total frames for the same 3 µm x 3 µm area, all imaged at a line rate of 10 Hz. The field of view displays the piezoresponse of columnar (001) grains in a polycrystalline $BaTiO_3$ thin film.

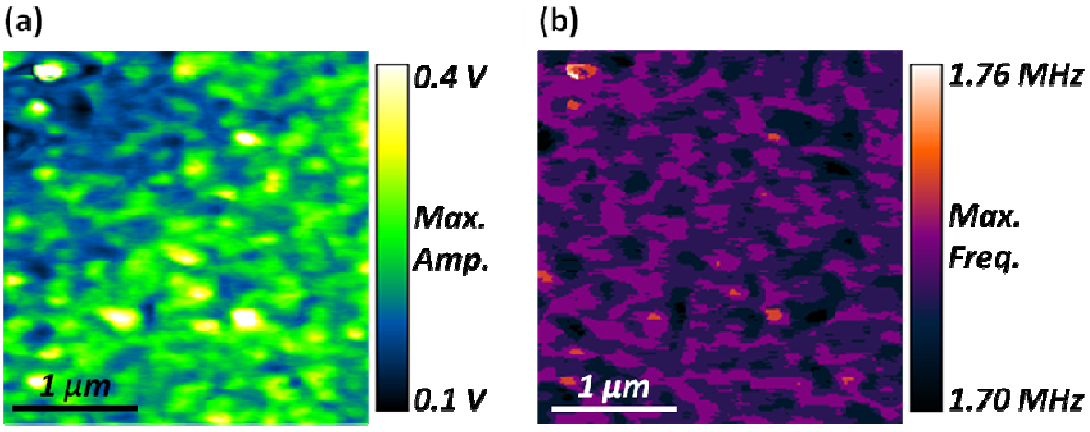

Figure 17: 2.34 µm x 2.27 µm map of maximum piezoresponse amplitude (a) and corresponding frequency (b), resolved down to 12 nm x 12 nm. These maps are based on 38,800 I-V curves from the dataset of Figure 16.

4.4. Conclusion

Spectroscopic Piezoresponse Force Microscopy (sPFM) has been demonstrated as an effective extension of multidimensional scanning probe microscopy that allows for the efficient mapping of electromechanical coupling in polycrystalline piezoelectric materials with nanoscale resolution. Building on the methodology of Nanoscale Conductance Mapping (NCM), this technique is more efficient than pixel-by-pixel data acquisition, and utilizes the inherent rastering properties of the AFM. The sPFM technique has been employed to map the maximum piezoresponse amplitude and corresponding frequency for a $BaTiO_3$ thin film, with the resonant peak varying by over 80 kHz for grains over a 3 x 3 μm area. Spectroscopic PFM is therefore promising for investigating the electromechanical properties of piezoelectric films, particularly those with a polycrystalline structure found in commercial capacitors and memory applications.

4.5. Experimental

All experiments were performed at room temperature with an Asylum Research Cypher AFM. Diamond coated silicon cantilevers (Nanosensors, CDT-FMR) were employed throughout, with a quoted tip length of 10-15 μm, cantilever length of 225 ± 10 μm, and resonant frequency of 65 - 155 kHz.

The ferroelectric $BaTiO_3$ thin film with conducting back electrode was mounted onto a metal sample holder with conducting silver paint and a wire for grounding to the bottom electrode. A 2V peak-to-peak sine wave was applied to the sample from an external function generator (Agilent Technologies, 33220A), and connected to the AFM cantilever holder by a soft flexible wire. The normal deflection signal of the cantilever was connected to the input of the lock-in amplifier (Zurich Instruments, HF2LI), and the component of the deflection signal due to the sample piezoelectric actuation was extracted by comparing the input to the external function

generator reference signal. The piezoelectric actuation amplitude was acquired with lock-in averaging times and sensitivities of 200 μs and 100 V/V_{RMS}, respectively.

4.6. References

1. H. Bluhm, A. Wadas, R. Wiesendanger, K. P. Meyer, and L. Szczesniak, Physical Review B **55** (1), 4 (1997).
2. M. Nonnenmacher, M. P. Oboyle, and H. K. Wickramasinghe, Applied Physics Letters **58** (25), 2921 (1991).
3. T. Keiji, K. Keiko, T. Kazuyoshi, and M. Hiroshi, Japanese Journal of Applied Physics Part 1-Regular Papers Short Notes & Review Papers **33** (5B), 3193 (1994).
4. O. Kolosov, A. Gruverman, J. Hatano, K. Takahashi, and H. Tokumoto, Physical Review Letters **74** (21), 4309 (1995).
5. A. Gruverman, O. Auciello, and H. Tokumoto, J Vac Sci Technol B **14** (2), 602 (1996).
6. J. F. Scott and C. A. P. Dearaujo, Science **246** (4936), 1400 (1989).
7. M. Y. Zhuravlev, R. F. Sabirianov, S. S. Jaswal, and E. Y. Tsymbal, Physical Review Letters **94** (24) (2005).
8. E. Y. Tsymbal, A. Gruverman, V. Garcia, M. Bibes, and A. Barthelemy, Mrs Bull **37** (2), 138 (2012).
9. I. Grinberg, D. V. West, M. Torres, G. Y. Gou, D. M. Stein, L. Y. Wu, G. N. Chen, E. M. Gallo, A. R. Akbashev, P. K. Davies, J. E. Spanier, and A. M. Rappe, Nature **503** (7477), 509 (2013).
10. Yongbo Yuan, Zhengguo Xiao, Bin Yang, and Jinsong Huang, Journal of Materials Chemistry A **2** (17), 6027 (2014).
11. S. V. Kalinin and D. A. Bonnell, Physical Review B **63** (12) (2001).
12. S. V. Kalinin and D. A. Bonnell, Physical Review B **65** (12) (2002).
13. G. Binnig, C. Gerber, E. Stoll, T. R. Albrecht, and C. F. Quate, Europhys Lett **3** (12), 1281 (1987).

Chapter 5: High Speed Friction Microscopy and Nanoscale Friction Coefficient Mapping

5.1. Abstract

As mechanical devices in the nano/micro length scale are increasingly employed, it is crucial to understand nanoscale friction and wear especially at technically relevant sliding velocities. Accordingly, a novel technique has been developed for Friction Coefficient Mapping (FCM), leveraging recent advances in high speed AFM. The technique efficiently acquires friction versus force curves based on a sequence of images at a single location, each with incrementally lower loads. As a result, true maps of the coefficient of friction can be uniquely calculated for heterogeneous surfaces. These parameters are determined at a scan velocity as fast as 2 mm/s for microfabricated SiO_2 mesas and Au coated pits, yielding results that are identical to traditional speed measurements despite being ~1000 times faster. To demonstrate the upper limit of sliding velocity for the custom setup, the friction properties of mica are reported from 200 μm/sec up to 2 cm/sec. While FCM is applicable to any AFM and scanning speed, quantitative nanotribology investigations of heterogeneous sliding or rolling components are therefore uniquely possible, even at realistic velocities for devices such as MEMS, biological implants, or data storage systems.

5.2. Foreword

As part of my undergraduate honors thesis, and extensive work by former Huey AFM labs member Dr. Sungjun Lee, a high-speed AFM was fabricated with scanning capabilities approaching 2000 Hz line rate (4 frames per second). Combined with the multidimensional NCM methodology (Chapter 3:), a similar technique has been developed called Friction Coefficient

Mapping (FCM), which quantitatively maps tribological properties with nanoscale spatial resolution. The following chapter discusses the application of this scanning method to various materials, along with limitations and scanning artifacts.

5.3. Introduction

Literally for centuries [1], studies have been conducted into friction, the related phenomena of wear, adhesion, and lubrication, and ultimately materials and component design to optimize sliding or rolling performance. Such tribological investigations are especially relevant to micro- and nano-electromechanical systems (MEMS/NEMS), which despite their widespread application in accelerometers, DLP projectors, ink-jet or fuel-injector heads, etc., can be hampered due to the relatively high adhesion forces at such small length scales [2-8]. The study of nanotribology aims to characterize, understand, and control these effects, and is principally conducted with variations of atomic force microscopy (AFM) [9,10]. However, MEMS/NEMS operate with velocities of tens of millimeters per second or more, significantly faster than the speed of most AFM systems [10]. Moreover, as device complexity continues to increase, heterogeneities in the local friction response are also increasingly relevant, but are difficult to quantify using present methods. Accordingly, this work is concerned with the development and application of a quantitative friction mapping method [11,12], operating at technically relevant sliding velocities, and suitable for real, heterogeneous surfaces.

AFM-based nanotribology is primarily accomplished using lateral force measurements, acquired by monitoring lever torque during contact-mode scanning perpendicular to the lever axis. So called Lateral Force Microscopy (LFM) [13,14] images are then based on a friction signal calculated at any given position from the difference in torsional contrast when scanning in opposite directions. This is performed with a fixed normal load, and typically at a low speed of

~1-10 μm/sec, ultimately yielding an LFM image that maps local friction behavior, although the quantitative nature of such images is limited due to the number of fixed variables.

To address this issue [14-19], the same lateral friction force signal is recorded as described above, but also for a range of normal loads approaching loss of contact. The coefficient of friction is then calculated from the slope of the lateral versus normal forces. Other parameters can also be extracted, including the force at zero normal load, the attractive force at zero friction, and any points of discontinuity. However, this approach generally provides a value instead of an entire image, as it is typically based on averaging the friction signal from multiple pixels, scan lines, or image frames, then incrementally changing the force, acquiring LFM data again, etc. It is thus primarily applicable to relatively homogeneous specimens where changes in location do not appreciably influence the adhesion characteristics.

To address the need for quantitative friction coefficient mapping, the current work uniquely leverages a custom high speed SPM system [20,21] to essentially combine LFM imaging and force-dependent friction measurements. Based on a sequence of high speed images, each acquired in the same area but with incrementally lower applied loads, this efficiently provides a 3-d dataset of friction versus area as sketched in Figure 18. A similar but standard-speed approach apparently developed in parallel was recently reported, though it notably does not measure the actual lateral friction and hence cannot extract friction coefficients [11]. Furthermore, it does not implement high speed imaging, and hence the data density is relatively sparse and does not allow velocity dependent studies over several orders of magnitude as reported here.

The array of friction-force curves which FCM provides, 65,536 of them for standard 256x256 pixel LFM images, thus provides a high data density of friction information for the imaged area.

Nanoscale maps of the coefficient of friction, friction at zero load, and/or load at zero friction can therefore be uniquely and efficiently generated, most importantly for surfaces with nanoscale heterogeneities in phases, topography, defects, etc. Tip speeds up to 2 cm/s are specifically considered with results that agree with previously reported models and experiments, demonstrating nanotribology investigations over several orders of magnitude of sliding velocity.

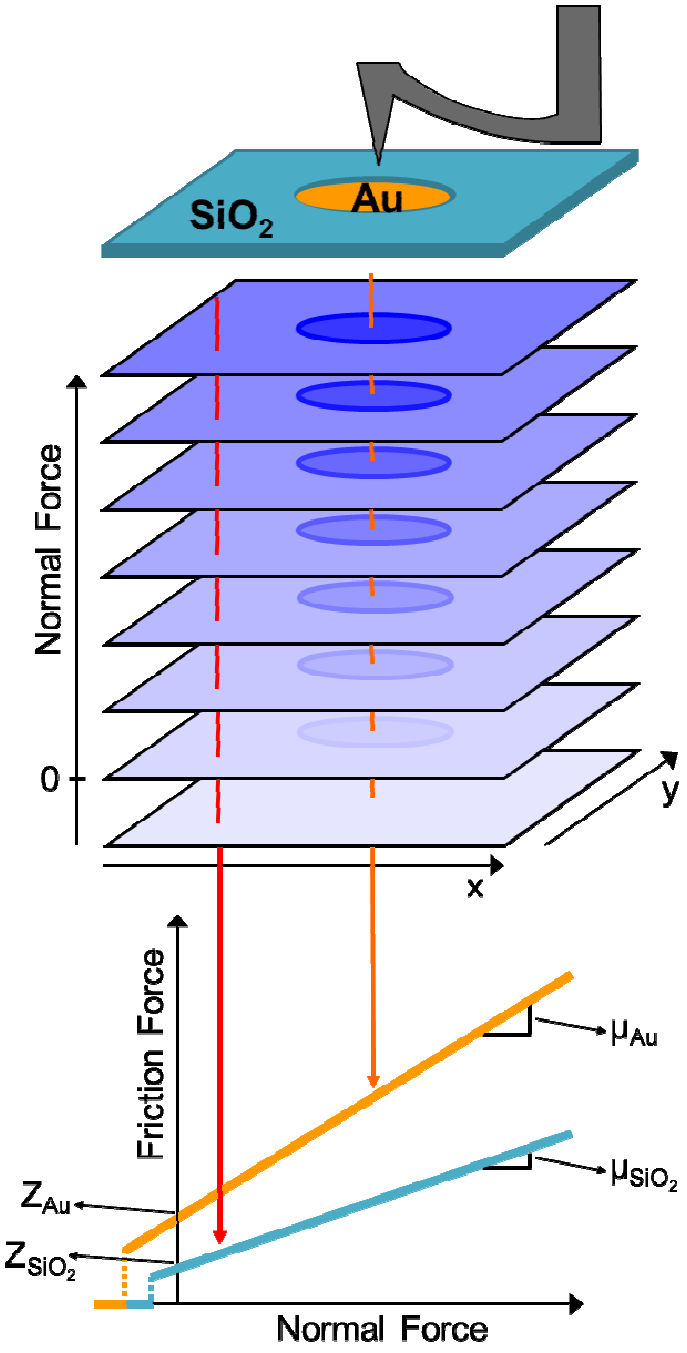

Figure 18: Sketch of the high speed Friction Coefficient Mapping approach for a heterogeneous SiO_2/Au specimen. Lateral force microscopy images are acquired with incrementally lower applied loads until loss of contact occurs. Friction force curves are then extracted for each pixel to quantify local friction properties.

5.4. Standard Speed Friction Measurements

Figure 19(a) typifies a common application of AFM based friction studies. As revealed by an SEM image, Figure 19(b), the specimen is a nanopatterned surface fabricated by sparse colloidal lithography. This surface has pits in a 14nm thick electron beam evaporated SiO_2 layer, revealing 300 nm diameter circular patches of an underlying granular thin film of Au deposited on a silicon wafer (substrate).

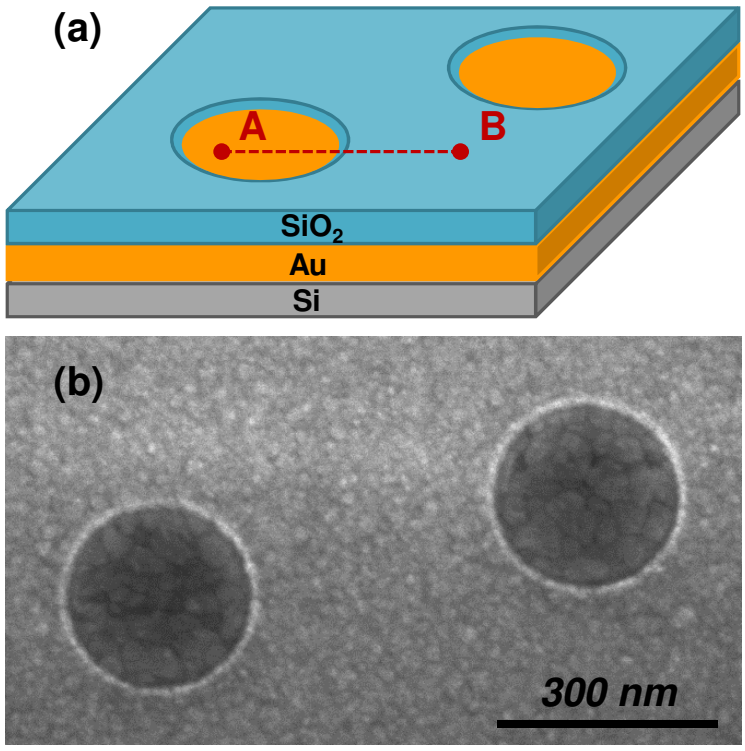

Figure 19: Sketch (a) and SEM image (b) of a model nanostructured specimen with Au bottomed pits in a SiO_2 film.

The AFM based topography for such a specimen, Figure 20(a), mimics the SEM contrast. Simultaneously acquired qualitative friction images, i.e. normal speed (4 µm/sec) LFM images, expectedly display contrast due to the distinct materials (Au and SiO_2) as well as edge effects

due to the topographic step, Figure 20(b). Nanostructuring of the friction response for the SiO_2 layer is also apparent, with feature dimensions as small as 10 nm clearly resolved related to the nanoscale grains of the polycrystalline SiO_2 film. The grain structure of the sputter deposited Au film is visible at the bottom of the pits as well. Of course, intermittent or non-contact AFM based phase imaging can provide similar qualitative images of friction, as it too can relate to local adhesion. Truly measuring the friction coefficient throughout the imaged area is challenging, however, especially for nanostructured surfaces where the roughness and variability hinders local friction quantification.

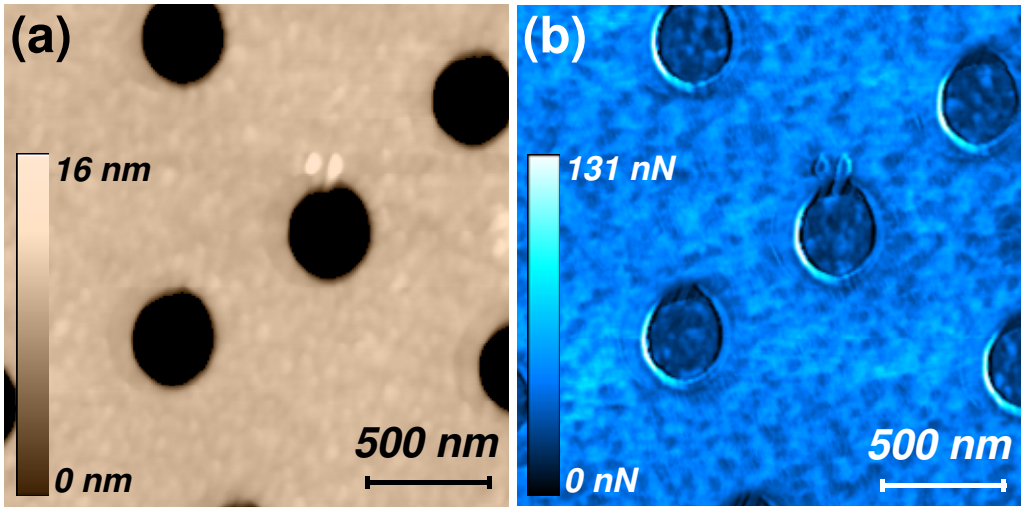

Figure 20: Standard speed AFM (a) and LFM (b) images (2 µm x 2 µm, 4 µm/s sliding velocity) of Au coated pits surrounded by SiO_2.

The traditional approach to quantifying lateral force data is to continuously re-scan a single line traversing multiple phases, e.g. between points A (Au) and B (SiO_2) as sketched in Figure 19(a), but crucially for a range of normal loads. Friction-force curves for each region are then typically generated by plotting the response from the distinct regions [17,18], e.g. the left (Au) and right (SiO_2) halves of the repeated friction lines at the corresponding normal forces. Accordingly,

Figure 21 presents the lateral friction with normal loading from 530 nN down to 2.75 nN, based on 96 force steps (lines of data) of -5.55 nN each applied along a single 500 nm line. Overlain error bars indicate a negligible standard deviation in the measured lateral force for each normal load. This implies a relatively uniform friction response in the distinct sample regions, at least within the 200-250 nm linear regions of each phase that were sampled. Standard deviations for the normal force error are too insignificant to see (<1%).

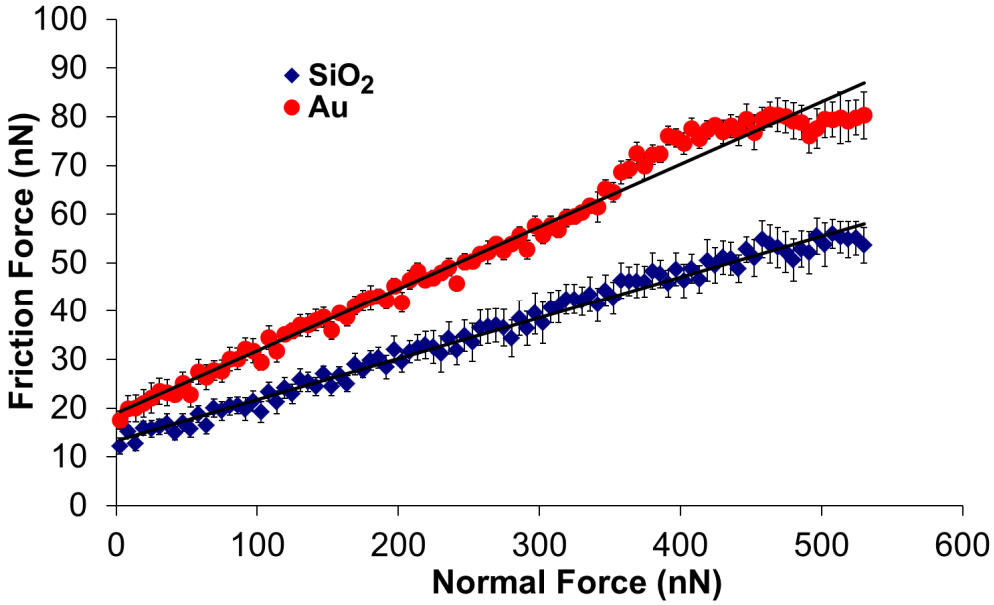

Figure 21: Friction force curves for SiO_2 and Au acquired at standard speeds (10 µm/s) for comparison with high speed results (standard deviation error bars are shown). The coefficient of friction for Au and SiO_2 over the entire loading range is 0.13 ± 0.01 and 0.08 ± 0.02, respectively, while the friction at zero applied force is 19 ± 4 nN and 13 ± 5 nN.

The friction coefficient (slope), and friction at zero load (offset), are clearly distinguishable for the two specimen regions. Based on least squares fitting of the entire dataset (overlaid) the Au phase exhibits a higher coefficient of friction than the SiO_2 phase (0.13 versus 0.08), with a ratio of the mean values of 1.52:1. Au also exhibits a higher friction at zero applied force with a mean ratio of 1.42:1.

The nonlinearity between 350 and 500 nN for Au is unexpected, and deserves future study particularly to assess the possibility that this indicates some sample wear at such high loads. Even so, however, in this instance it happens to be the case that fitting the purely linear region of the Au curve (from 0 to ~350 nN of normal force only) leads to identical coefficients of friction (within significant digits) as for the entire loading range (0 to ~550 nN normal force). The linear fit R^2 values are also equivalent, with 0.98 and 0.99 considering the entire loading range for Au and SiO_2 respectively, as compared to 0.99 and 0.98 for the loading range from 0 to 350 nN.

The obvious disadvantage to this line-by-line approach is that subtle variations in friction along the measured line may correlate to specific regions, phases, structures, etc., instead of simply expanding the error bars. Naturally the friction data could be separated into more than 2 subsets, which is conceptually identical and certainly feasible. However, generally this would be impractical as it requires unique computational solutions for any given region of a sample. Moreover, it presumes the ability to distinguish the unique regions, a particular challenge along just 1 dimension. Finally, the method is susceptible to position drift as well, with the tip practically scanning a slowly shifting line, contributing to possible load-dependent error for inhomogeneous surfaces or in the event of wear. The ability to image the friction coefficient is therefore paramount.

5.5. Friction Coefficient Mapping

The results presented above implemented a relatively standard sliding velocity of 10 μm/sec, based on a line rate of 10 Hz. However, measurements at much higher velocities are feasible with high speed SPM, employing line scanning rates on the order of hundreds to thousands of Hz that correspond to sliding velocities approaching cm/s instead of μm/s. This speed enhancement makes it experimentally practical to rapidly acquire multiple images of the friction signal at

distinct normal loads as explained for Figure 18, instead of simply detecting friction for a single scan line (or part of one) as in

Figure 21. Accordingly, Figure 22 displays a montage of 10 LFM images extracted from a complete sequence of 28 consecutive scans, each with decremented normal loads from 765 nN down to -3 nN as indicated. All are from a single, 1 µm x 1 µm region with a circular pit present near the image center, for the same specimen as considered in Figure 19-Figure 21. The crucial distinction is that here, a 1000 Hz line rate was employed throughout. This is 500 times faster than with Figure 20, requiring only 7 seconds for the entire 28-image experiment.

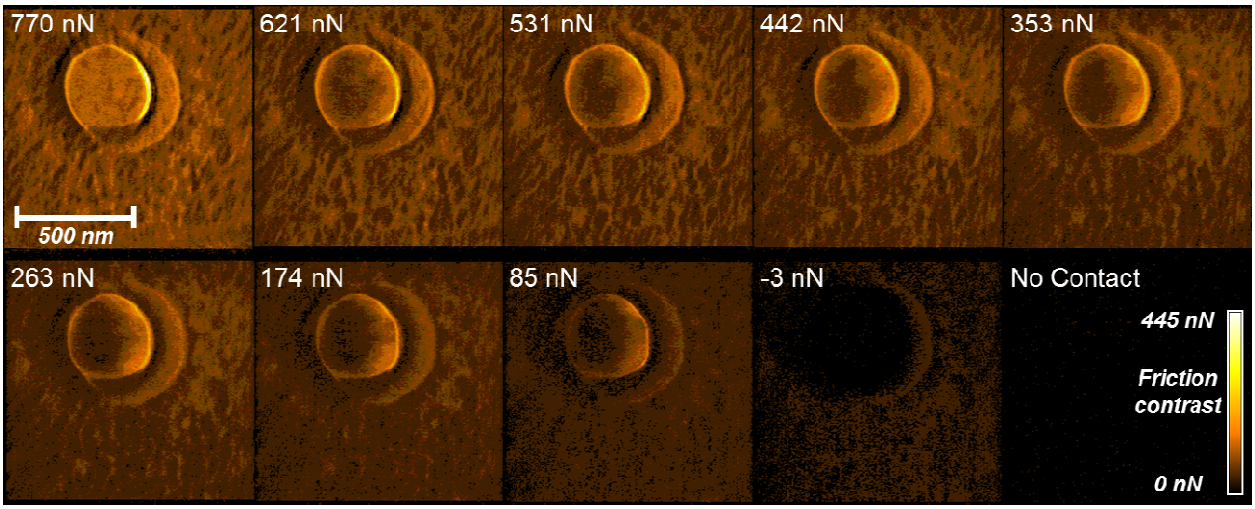

Figure 22: Montage of high speed friction images at distinct normal loads as labeled, representing a subset of 28 total images for the same 1 µm x 1 µm area, all imaged with a tip velocity of 2000 µm/sec based on a line rate of 1000 Hz.

Extracting the friction versus normal force from each point in the 250x250 pixel images of Figure 22 therefore can provide up to 62,500 friction-force curves, each similar to those presented in

Figure 21. After standard drift correction for the 28 sequential images (forces) as described in the experimental section, the slope of each curve (i.e. for each pixel) can easily be calculated. This is

presented in Figure 23(a), a map of the coefficient of friction, with spatial resolution of just 4 nm x 4 nm. Random scatter in each friction versus normal force curve is quantified in Figure 23(b and c), which respectively present the 95% confidence error and the coefficients of determination (R^2) for the friction coefficients. Due to the observed nonlinearity in the friction versus normal force curve for Au above ~350 nN during traditional friction measurements (i.e. Figure 21), the FCM-determined coefficient of friction, 95% confidence error and R^2 values, are conservatively assessed based only on the linear friction regime (<350 nN).

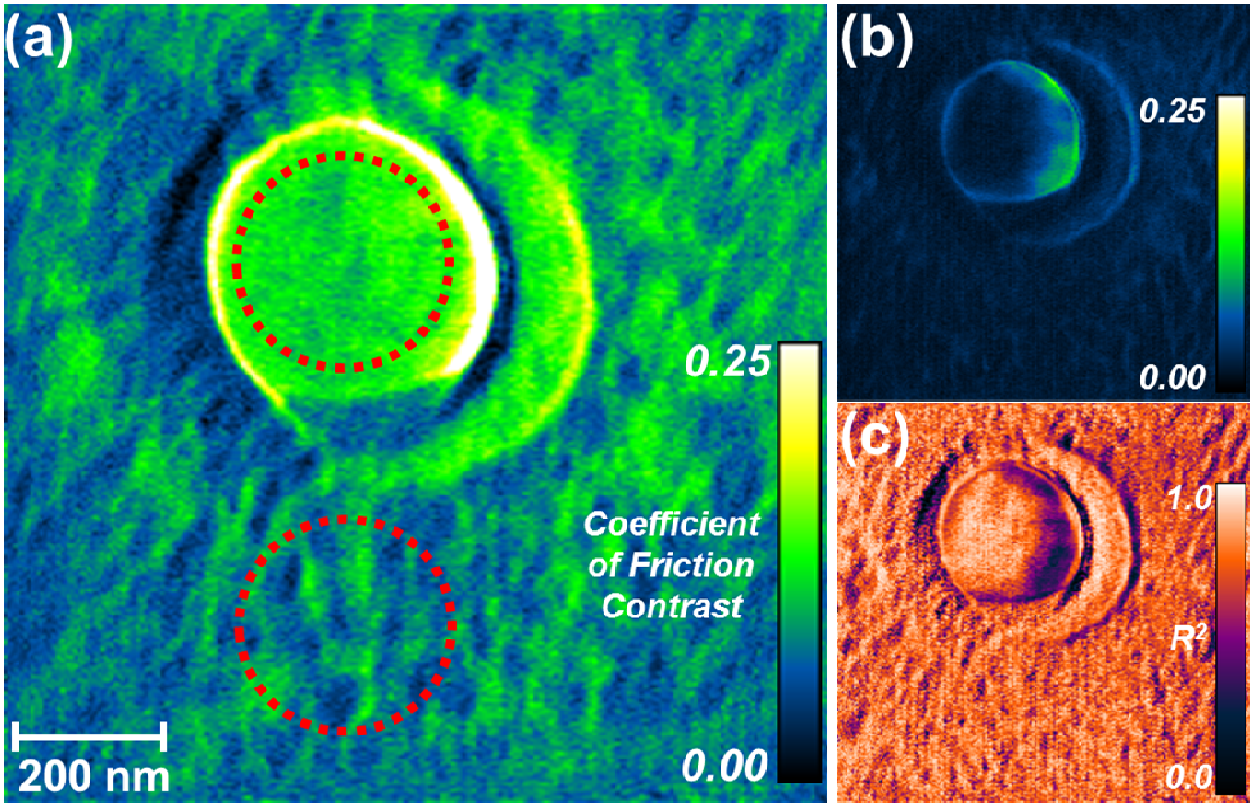

Figure 23: 968 nm x 956 nm map of the coefficient of friction resolved down to 4 nm x 4 nm, based on 57,838 friction force curves up to normal loads of 350 nN from the dataset of Figure 22, all acquired by high speed SPM in just 7 seconds with a 2 mm/sec tip velocity (a). The corresponding 95% confidence interval (b) and coefficient of determination, R^2, (c) of the coefficient of friction map are also shown.

As with the standard LFM image of Figure 20, higher friction is apparent in Figure 23 for the Au-coated pit-region compared to the surrounding SiO_2. Comparing equal areas for these two phases, as sketched in Figure 23, histograms of the results indicate a mean coefficient of friction

for the SiO_2 region of 0.12 ± 0.01 (standard deviation), while for the Au pits it is 0.08 ± 0.02. But, since the friction coefficient is now mapped, it is also uniquely revealed that friction is more uniform in the pits, as compared to the surrounding SiO_2 where nanostructuring is clearly visible (similar to the LFM image of Figure 20). Using traditional nanotribology methods, such heterogeneities due to varying friction and/or adhesion either would have been averaged out (as with

Figure 21), caused increased apparent error (standard deviation bars in

Figure 21), or more perniciously skewed the results higher or lower than the statistical mode (if the position dependent response were not as symmetric as occurs here, especially in the SiO_2).

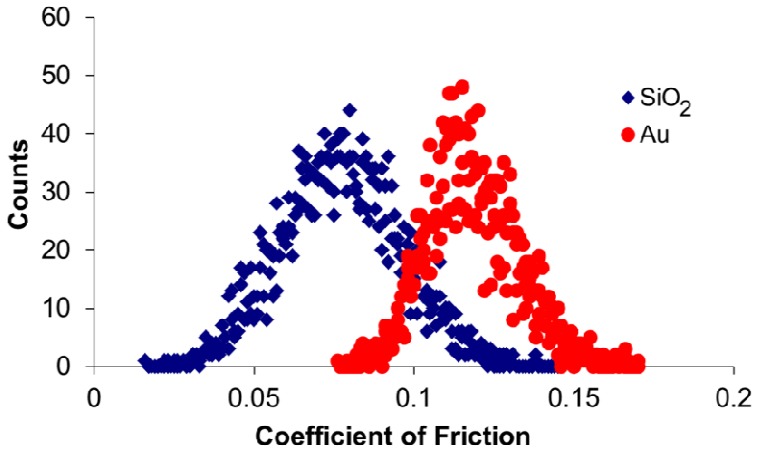

Figure 24: Histogram of local friction coefficients from equal areas (0.047 µm^2) in the two distinct phases of Figure 23.

It is insightful to compare these high speed results with standard speed friction measurements. The ratio of mean friction coefficients for the Au pit vs. the surrounding SiO_2 for the high sliding velocity of ~2 mm/s (from Figure 24) is 1.52:1. At a more common 10 µm/s (200 times slower, from

Figure 21) the mean ratio was identical within significant digits. Results from the high speed FCM approach are therefore consistent with traditional speed friction measurements, both visually and quantitatively, with the benefit that they efficiently and spatially resolve the friction.

5.6. Velocity Dependence of Friction

Extending this concept further, high speed SPM can be employed for nanoscale friction investigations at sliding velocities approaching those comparable with actual sliding or rolling applications. Sliding speeds as low as 4 nm/s [14,22-24] and as high as 200 mm/s have been reported elsewhere [9,10], while scan lengths from 2 nm [14] to 1 mm [10] have been considered. Studies at these extremes are typically for only a fixed (or just a few arbitrary) load(s), though, instead of the broad range of consecutive loads that are necessary to accurately calculate the friction coefficient and other friction parameters. The highest velocity investigations [9,10] reported are also for a single scan line (i.e. non-imaging), and hence are not as applicable for heterogeneous surfaces.

Here, the high speed capabilities of the custom SPM system are leveraged to study friction for sliding velocities ranging from ~200 μm/s up to ~2 cm/s. For each speed, the friction force was recorded while scanning at a line rate of 1000 Hz just as in Figure 23, except the scan size was decremented for each new frame, ultimately encompassing 22 distinct sliding velocities. This was performed on a freshly cleaved mica specimen, providing a homogeneous surface exhibiting a few atomic terraces. As before, such topographic features caused variations in the normal load, though again normal forces were simultaneously measured and subsequently employed to calculate the correct local friction contrast. Averaging the results from each image for simplicity (since spatially they are nearly featureless), Figure 25 displays this mean friction signal normalized by the normal load as a function of sliding velocity. A standard deviation of less than

±5% within the area measured was found at every velocity, accounting for the variations in normal load.

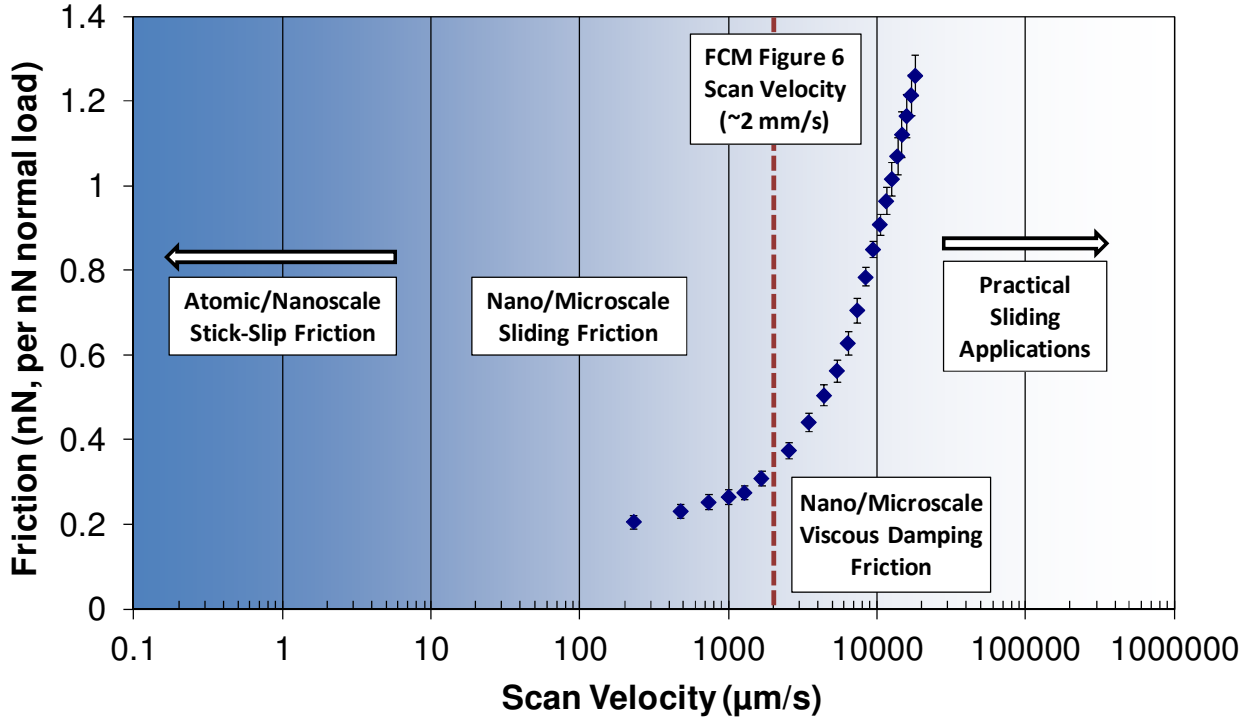

Figure 25: Friction Force normalized by normal load, versus sliding velocity, for a diamond coated probe on a cleaved mica substrate, noting ranges of relevant friction behavior and the speed used for Figure 23. The Friction Forces were recorded at a line rate of 1000 Hz.

The dominant friction mechanisms for the data points considered in Figure 25 are sliding friction and viscous damping effects. Atomic scale stick-slip mechanisms, on the other hand, are unlikely to play a role [25,26] unless much lower velocities (and forces) were employed as noted in the plot. Future work specifically investigating the relevant mechanisms, e.g. considering stress-modified thermal activation, would be insightful, but the present effort is focused on the imaging and speed capabilities of FCM in general.

Clearly, for low speeds the friction increases linearly versus the logarithm of scan velocity. This suggests a sliding friction mechanism as indicated in Figure 25, agreeing with previous observations over similar ranges using standard friction microscopy approaches [22-24,26].

Under sliding friction conditions, the AFM probe is travelling with a low enough sliding velocity to cause adequate interaction with the substrate, where the tip is fixed in the minimum of the interaction potential (the "stick" state). As the probe travels further, the tip "slips" to the next interaction potential minimum. During this period, the "slip" velocity of the tip is much higher than the sliding velocity. It is during this "slip" motion that most of the energy is dissipated, and is therefore independent of the sliding velocity of the probe for a wide range of sliding velocities [23]. As the velocity increases further, on the other hand, the friction increases faster, with a higher slope versus the log of velocity that continued to the highest speed achieved in our work, 2 cm/sec. Based on modeling or non-imaging friction measurements, such an increase in friction at higher speeds is generally attributed to viscous damping forces [10,23,24]. During this regime, the tip has a reduced ability to displace adsorbed molecules on the substrate, resulting in higher friction force. Such effects have been reported to be stronger for scanning in inert atmospheric conditions [27], but the experiments performed here up to substantially higher speeds display the viscous damping effect under ambient conditions as well.

With the continued development of small and/or higher precision lateral or rotational actuators, such friction mapping and variable speed measurements are clearly useful for investigating the friction at practically relevant sliding velocities.

5.7. Friction Mapping Artifacts

Three primary artifacts are important to consider in terms of error in any friction measurements. First, the tip may not properly maintain a constant normal load in all locations. This would cause the locally applied normal force to be different from that anticipated based on the simple AFM setpoint value, shifting the affected friction points laterally on their corresponding friction versus normal force curves (Figure 21). This can easily be accounted for, though, by simultaneously

recording the normal deflection along with the torsional (LFM) signal during scanning, in fact as performed here. As a result, the precisely known normal load is incorporated at every image pixel, for every frame in the montage of Figure 22, therefore yielding more precise friction–force curves throughout the imaged area. One practical consequence is that the overall range of normal loads differs somewhat from location to location. Still, it is trivial during analysis to simply consider a uniform loading range for each image pixel when calculating maps of the friction coefficient (slope of each pixel's force-friction curve) or other friction parameters.

This correction does not account for the second category of artifacts, however, those due to changes in topography [28] and contact area [29] during scanning. Indeed, edge effects are clearly present at the pit circumference where topographic discontinuities are greatest (the nearly continuous bright ring around the pit). This has been attributed to the ratchet mechanism of friction, and also due to additional torsion created by tip collision with upward sloping asperities, neither of which can be corrected by the standard "trace minus retrace" friction compensation [28]. Such a variation in friction due to the ratchet mechanism is proportional to the slope of the topography, which reaches a maximum of 5° and 12° for the SiO_2 and Au regions, respectively, and a maximum of 37° at the SiO_2/Au interface. The maximum corresponding friction variations due to the ratchet mechanism (Equation 3 in [28]) are therefore predicted to be 1%, 4%, and 56% for the SiO_2, Au, and SiO_2/Au interface, respectively. Much greater variations are detected within in all three regions, however, related to the distinct material responses within the SiO_2 and Au regions, and caused by tip collision effects at the topographic interface. Such collision effects are difficult to quantify as noted in [27] since they nonlinearly depend on several factors including applied normal load, scan velocity, and tip geometry.

Additional crescent shaped features, with apparently enhanced friction to the right of the pit and depressed friction at the left, are also visible. Their symmetric but opposite contrast evidences their origin: the inherent necessity in friction imaging of subtracting lateral signals from opposite scanning directions, combined with the fact that the normal and hence lateral loads are slightly different when approaching versus just climbing out of the pit at high speeds. Such effects can be diminished with sharper AFM probes or slower scanning, respectively, but are generally unavoidable in all variations of AFM. For flat surfaces, on the other hand, friction artifacts from topography and contact area are expected to be negligible (e.g. the cleaved mica substrate in Figure 25). Any heterogeneity in the friction contrast should therefore be material dependent under these conditions.

The third common artifact source, tip and/or sample wear, is also a general challenge in SPM, conceivably worsened by high speed imaging as employed here. In the present measurements, the highest normal loads are applied first with subsequent images employing consecutively lower loads. Therefore, any sample damage will predominantly occur in the first, high-load image(s). Wear of course is a progressive phenomenon, but since it is load dependent it will predominantly occur in the first images as well, likely explaining the nonlinear response observed in the high-load early images of the traditional friction measurement of Figure 21. For the tip, the poly-crystalline diamond coating ensures that minimal blunting will occur after the first high-load images. Corroborating these assumptions, the topography images and cross-sections from the dataset analyzed to construct Figure 22-Figure 24 show no appreciable changes, even for the finest features. This implies that the tip and sample are stable under such conditions. Certainly, sub 20 nm features are consistently resolved throughout the multiple images that are compiled to generate Figure 23.

5.8. Conclusion

This work discusses a new Atomic Force Microscopy based method enabling areal Friction Coefficient Mapping (FCM) with nanoscale spatial resolution. As presented, the FCM method leverages high speed SPM imaging at 4 full frames per second. In general, however, FCM is applicable with any speed of AFM imaging, simply requiring more patience and drift stability (or corrections) for standard AFM conditions. For example, an experiment with equivalent force and pixel resolution as that in Figure 23 would require a tolerable but inconvenient 117 minutes (1000 times longer) for 1 Hz scan rates. The Friction Coefficient Mapping presented here is therefore a widely applicable advance, compatible with future as well as legacy AFM instruments.

Results acquired for a mica substrate support a transition between two friction regimes as sliding velocities vary from 200 to as high as 20,000 μm/s. Meanwhile, the ratio of friction coefficients between distinct phases in a nanostructured Au and SiO_2 test specimen remained equal over 2 orders of magnitude of tip speeds. FCM therefore allows novel friction studies of heterogeneous surfaces, at velocities ranging from traditional speeds to those approaching realistic sliding or rolling applications (cm/s). The velocity dependence of discrete components can further be investigated to understand the influence of distinct phases, defects, interfaces, and/or topographic features, of growing importance for realistically heterogeneous surfaces in applications such as MEMS/NEMS, bio-materials, and data storage systems.

5.9. Experimental

All experiments are performed at room temperature in ambient air using an Asylum Research Cypher AFM. The AFM's internal feedback system is employed throughout in order to try to maintain a constant normal force between tip and surface via the built-in proportional-integral-

derivative (PID) controller feedback loop. For optimal speed, however, all other AFM functions are performed externally based on a National Instruments PXIe-1062Q chassis implementing custom National Instruments LabVIEW code. This includes recording both normal (deflection) and lateral (torsion) cantilever signals with a PXIe-6124 acquisition card (4 channel, simultaneous sampling, up to 4 megasamples/s). A PXI-5421 arbitrary waveform generator (16 bit, up to 100 megasamples/s) is also used to externally drive the X and Y piezoactuators of the AFM, synchronized to the data acquisition board via an 80 MHz clock.

During highest speed scanning, performed 'open loop' (i.e. without position feedback), the actual scanning amplitude (image size) and phase (image registry) will depend on the resonant response of the actuator for the fast scan direction. To accommodate this, the lateral scales of all topography, normal deflection, and lateral friction images are calibrated post-imaging based on simultaneously acquired position sensor data, all with respect to closed loop, slow speed images acquired over known distances on calibration standards.

Diamond coated silicon cantilevers (Nanosensors, CDT-FMR-8) are employed throughout, with a quoted tip length of 10-15 µm, cantilever length of 225 ± 5 µm, and resonant frequency of 60-100 kHz. Each cantilever's spring constant was calibrated in situ, following the "wedge method" common for lateral spring constant calibration [19]. This method incorporates the normal spring constant (determined in situ via the widely employed thermal-tune method) [30], normal and lateral sensitivity of the detecting quadrant photodiode, and ratio of normal to lateral forces when scanning sloped surfaces. The calibration specimen is a MikroMasch TGG01 characterization grating, with precise surface slopes defined by exposed Si [111] planes [31]. Typical measured values of the lateral spring constant are 80.6 – 90.9 N/m, the normal spring constant is 5.5 – 6.2 N/m, the normal sensitivity ranges from 250 - 295 nN/V, and the lateral sensitivity is 4280 nN/V.

Since the various specimens studied are relatively smooth (mica, microfabricated semiconductor structures), imaging is assumed to be achieved with a single asperity protruding from the nanoscale roughness of the diamond coated tips.

For Friction Coefficient Mapping (Figure 23), the 28-image sequence was acquired at 4 frames per second. Drift of the imaged area is therefore minimal during the 7 second experiment, a substantial benefit for high speed SPM. Nevertheless, since the analysis assumes identical locations for any given pixel in every image, standard drift correction algorithms were employed using common image processing software (ImageJ, Matlab). Tracking topographic features, this yielded a linear drift for the entire experiment of just 32 nm and 44 nm (8 and 11 image pixels) in the fast and slow scan directions, respectively. Pixel shifting to align the consecutive images, and truncating any pixels that therefore were not imaged throughout the experiment, leads to final friction maps with 53,352 points (242 by 239 pixels).

Between each frame, the normal force was decremented by ~31 nN in normal force without stopping the scanning process. The vertical feedback loop transitioned within at most 12 milliseconds (12 scan lines), though friction loops are stable throughout this process. There is no impact on the calculated friction coefficient, however, since it is based on the actually measured normal and lateral forces for every pixel. The normal forces were applied from highest to lowest so that any abrupt damage, or gradual wear, for tip or sample occurs primarily in the first (highest load) imaging frames, and therefore does not introduce appreciable error into the multi-image procedure and analysis.

Due to the large normal load range implemented in the experiment, cantilever torsion and its impact on pixel registry has also been considered. The maximum cantilever torsion based on all factors in this experiment (scan size, tip geometry, normal/lateral force, etc.) is just 1 pixel along

each scan direction [32]. This corresponds to a registry error of at most 2 pixels since friction is measured by relating trace (-1 pixel) and retrace (+1 pixel) scans. This misregistry has been accounted for where applicable in the image analysis, but is practically negligible.

The coefficient of friction is calculated for each pixel based on the local linear fit of the friction versus the normal force, using the least squares method. Since the results are spatially resolved, the 95% confidence interval for the coefficient of friction, accounting for data scatter, can also be uniquely visualized, Figure 23(b). There is an average 95% confidence interval of 0.02 ± 0.01 in the SiO_2 region of interest, and 0.03 ± 0.01 in the Au region of interest. The coefficient of determination, R^2, has also been calculated from each linear fit and is compiled in Figure 23(c). The average R^2 values for the Au and SiO_2 regions of interest are 0.76 ± 0.15 and 0.74 ± 0.11, with a corresponding mode of 0.87 and 0.81, respectively.

The fact that the coefficient of determination is less than 1 could result from either random scatter for each pixel's friction-force data, or from a poor linear fit due to a nonlinear actual response. Accordingly, the skewness of the data to the linear fit has also been calculated for each pixel. Histograms of this skewness for the Au and SiO_2 regions are Gaussian peaks with averages and standard deviations of 0.01 ± 0.51 and -0.02 ± 0.32, respectively. Spatial preferences for the skewness are also negligible excepting edge effects (i.e. any given pixel can skew slightly positive or slightly negative, independent of Au, SiO_2, etc.). Since the skewness is evenly but randomly distributed about zero, this confirms random scatter around the linear least squares fits at each pixel. Practically, this means that acquiring more images at distinct normal loads would improve the coefficient of determination (R^2) and 95% confidence for each pixel. But this would yield only marginal real benefits since the crucial parameter, the magnitude of the friction coefficients, will remain essentially unchanged.

For velocity dependent friction (Figure 25), only the central 50 pixels from each image line (each speed) are used for calculation to conservatively avoid any edge effects as the tip accelerates or decelerates during highest speed scanning. Since the friction data is acquired along 250 scan lines, 12,500 pixels are thus analyzed for each point in the plot.

The patterned SiO_2/Au specimen was prepared by Sparse Colloidal Lithography using monolayers of polystyrene (PS) colloids prepared by electrostatic self-assembly as a shadow-mask, described thoroughly elsewhere [33,34]. Briefly, a Si wafer substrate was sputter coated with 30 nanometers of Au (2nm Ti adhesion layer). The surface was functionalized with a polyelectrolyte triple layer by sequential deposition of positive PDDA (poly(diallyldimethylammonium chloride), negative PSS (poly(sodium-4-styrenesulfonate)) and positive PAX (polyaluminium chloride) monolayers by electrostatic self-assembly giving a stable positive charge at neutral pH. An array of 300 nanometer colloidal PSS spheres was then assembled from solution forming a short range ordered array of particles with spacing determined by the electrostatic repulsion between already adsorbed and later arriving colloids. After a thermal treatment step in water to prevent rearrangement of the film by capillary forces during drying, a polycrystalline SiO_2 layer is deposited by electron beam stimulated thermal evaporation. The PSS colloids are subsequently removed by tape striping, leaving a short range ordered array of ~300 nm pits in the SiO_2 layer with Au at their base.

5.10. References

1. D. Dowson, *History of Tribology*. (Longman, University of California, 1979), p.677.
2. Sriram Sundararajan and Bharat Bhushan, Wear **217** (2), 251 (1998).
3. Sriram Sundararajan and Bharat Bhushan, Wear **225–229** (0), 678 (1999).
4. I.; Chandross Szlufarska, M.; Carpick, R.W., J. Phys. D: Appl. Phys. **41** (12), 123001 (2008).
5. D. S. Grierson, E. E. Flater, and R. W. Carpick, J Adhes Sci Technol **19** (3-5), 291 (2005).
6. R. Maboudian, W. R. Ashurst, and C. Carraro, Tribol Lett **12** (2), 95 (2002).

7. R. Maboudian and R. T. Howe, J Vac Sci Technol B **15** (1), 1 (1997).
8. H. J. Butt, B. Cappella, and M. Kappl, Surf Sci Rep **59** (1-6), 1 (2005).
9. N. S. Tambe and B. Bhushan, Nanotechnology **16** (10), 2309 (2005).
10. Tao Zhenhua and Bharat Bhushan, Rev. Sci. Instrum. **77** (10), 103705 (2006).
11. R. Alvarez-Asencio, J. S. Pan, E. Thormann, and M. W. Rutland, Tribology Letters **50** (3), 387 (2013).
12. S. Breakspear, J. R. Smith, T. G. Nevell, and J. Tsibouklis, Surf Interface Anal **36** (9), 1330 (2004).
13. O. Marti, J. Colchero, and J. Mlynek, Nanotechnology **1** (2), 141 (1990).
14. C. Mathew Mate, Gary M. McClelland, Ragnar Erlandsson, and Shirley Chiang, Phys. Rev. Lett. **59** (17), 1942 (1987).
15. R. W. Carpick, N. Agrait, D. F. Ogletree, and M. Salmeron, J Vac Sci Technol B **14**, 1289 (1996).
16. M. Enachescu, R. J. A. van den Oetelaar, R. W. Carpick, D. F. Ogletree, C. F. J. Flipse, and M. Salmeron, Phys. Rev. Lett. **81** (9), 1877 (1998).
17. Guangtu Gao, Rachel J. Cannara, Robert W. Carpick, and Judith A. Harrison, Langmuir **23** (10), 5394 (2007).
18. J. Hu, X. d Xiao, D. F. Ogletree, and M. Salmeron, Surf. Sci. **327** (3), 358 (1995).
19. D. F. Ogletree, R. W. Carpick, and M. Salmeron, Rev. Sci. Instrum. **67** (9), 3298 (1996).
20. Bryan D. Huey, Annu. Rev. Mater. Res. **37** (1), 351 (2007).
21. B. D. Huey, R. N. Premnath, S. Lee, and N. A. Polomoff, J. Am. Ceram. Soc. **95** (4), 1147 (2012).
22. T. Bouhacina, J. P. Aime, S. Gauthier, D. Michel, and V. Heroguez, Phys Rev B **56** (12), 7694 (1997).
23. O. Zworner, H. Holscher, U. D. Schwarz, and R. Wiesendanger, Appl Phys a-Mater **66**, S263 (1998).
24. E. Gnecco, R. Bennewitz, T. Gyalog, Ch Loppacher, M. Bammerlin, E. Meyer, and H. J. Güntherodt, Phys. Rev. Lett. **84** (6), 1172 (2000).
25. E. Gnecco, R. Bennewitz, T. Gyalog, and E. Meyer, J Phys-Condens Mat **13** (31), R619 (2001).
26. D. Gourdon, N. A. Burnham, A. Kulik, E. Dupas, F. Oulevey, G. Gremaud, D. Stamou, M. Liley, Z. Dienes, H. Vogel, and C. Duschl, Tribology Letters **3** (4), 317 (1997).
27. P. Bilas, L. Romana, F. Bade, K. Delbe, and J. L. Mansot, Tribology Letters **34** (1), 41 (2009).
28. Sriram Sundararajan and Bharat Bhushan, J. Appl. Phys. **88** (8), 4825 (2000).
29. K. Kanaga Karuppiah, Angela Bruck, and Sriram Sundararajan, Tribol Lett **36** (3), 259 (2009).
30. C. P. Green, H. Lioe, J. P. Cleveland, R. Proksch, P. Mulvaney, and J. E. Sader, Rev Sci Instrum **75** (6), 1988 (2004).
31. MikroMasch.
32. O. Sul, S. Jang, and E. H. Yang, Meas Sci Technol **20** (11) (2009).
33. Jenny Malmstro□m, Brian Christensen, Hans P. Jakobsen, Jette Lovmand, Rasmus Foldbjerg, Esben S. Sørensen, and Duncan S. Sutherland, Nano Lett. **10** (2), 686 (2010).
34. Per Hanarp, Duncan S. Sutherland, Julie Gold, and Bengt Kasemo, Colloids Surf. A **214** (1–3), 23 (2003).

Chapter 6: Error-Corrected AFM: A Simple and Broadly Applicable Approach for Substantially Improving AFM Image Accuracy

6.1. Abstract

Atomic Force Microscopy (AFM) has become an indispensable tool for imaging the topography and properties of surfaces at the nanoscale. A ubiquitous problem, however, is that optimal accuracy demands smooth surfaces, slow scanning, and expert users, contrary to many AFM applications and practical use patterns. Accordingly, a simple correction to AFM topographic images is implemented, incorporating error signals such as deflection and/or amplitude data that have long been available but quantitatively underexploited. This is demonstrated to substantially improve both height and lateral accuracy for expert users, with a corresponding 3-5 fold decrease in image error. Common image artifacts due to inexperienced AFM use, generally poorly scanned surfaces, or high speed images acquired in as fast as 7 seconds, are also shown to be effectively rectified, returning results equivalent to standard 'expert-user' images. This concept is proven for contact mode AFM, AC mode, and high speed imaging, as well as property mapping such as phase contrast, with obvious extensions to many specialized AFM variations as well. Conveniently, as this correction procedure is based on either real time or post-processing, it is easily employed for future as well as legacy AFM systems and data. Such Error Corrected AFM therefore offers a simple, broadly applicable approach for more accurate, more efficient, and more user-friendly implementation of AFM for nanoscale topography and property mapping.

6.2. Foreword

While scanning at speeds in excess of 2000 μm/s to acquire the lateral friction images for the SiO_2/Au regions in Chapter 5:, it was apparent that the topography images were featureless, even

though a ~13 nm height 'step' exists between both phase regions. This disparity was found captured within the cantilever deflection error signal, typically only utilized for the tip/sample vertical feedback loop and thrown away. By simply calibrating this error signal and adding to the height signal, the true topography signal was restored. The following chapter demonstrates this Error-Corrected AFM technique for contact and noncontact modes, and proposes broad applicability to other AFM variations.

6.3. Introduction

Atomic Force Microscopy has become a relatively mature technology since its invention more than 25 years ago [1], with extensive development and application for a wide range of conditions and disciplines. Several details about AFM imaging are curious and ubiquitous, however, yet have essentially been unaddressed throughout this time. For instance, height as well as property data are never truly identical when scanning in opposite directions, even after accounting for scanner artifacts. Cases where surface tracking notably suffers have become particularly apparent for highly 3-dimensional surfaces, and especially as high speed scanning has become more common.

Physically, the reasons for the direction dependent disparities are simple: AFM results are sensitive to the tip-sample contact force, and this can be substantially shifted when preceding or following an abrupt step, when the tip contact area changes from one location to the next, or even when scanning up or down a slope. Conveniently, though, many properties measured by AFM are predictably related to these parameters, a fact that this work recognizes and leverages initially to enhance height and phase contrast, but which in fact are broadly applicable to a wide range of specialized AFM variations.

Specifically, as is well known, the cantilever-based probe implemented in most AFM systems deflects upon interactions between the integrated tip and attractive or repulsive forces. Similarly, the resonant frequency of the lever (and amplitude, and phase) shifts when the tip is in the presence of a force gradient. These various 'error signals,' usually deflection for contact mode, or amplitude for intermittent or non-contact (AC) modes, are therefore used to sensitively maintain a user-specified tip-sample interaction. This is achieved by continually comparing them to a setpoint value in a feedback loop which controls the height of the probe. When scanning a homogeneous surface with purely topographic features, changes in the error signal are therefore caused by changes in the local surface height. Accordingly, the AFM probe is lifted above a protrusion or pushed into a depression, and the necessary actuation to return to the setpoint is recorded as the local 'height.' Industry, academia, and increasingly even manufacturing settings rely on this approach to visualize surfaces, measure roughness, assess critical dimensions, etc. But universally, we all essentially ignore the deflection or amplitude signals other than using them visually (or occasionally more actively) [2,3] to tweak feedback settings and thereby try to maintain a subjectively 'better' topographic image of the surface. Therefore, our hypothesis is that summing the calibrated deflection and/or amplitude at any given time with the simultaneous vertical actuation (height) will provide a 'corrected height' that is a more consistent measure of the real surface topography. To demonstrate this principle, raw and corrected height images are displayed for a tip characterization grating at various line scan rates and feedback loop settings. The technique is also applied to a SiO_x/Au thin film, evidencing effectiveness at high line scan rates.

Admittedly, it is surprising that this exceedingly simple idea is not already widely applied. More than likely, if seriously considered at all,[1] summing the height and error signals probably appeared to be simply a subtle improvement in comparison to the ongoing development of literally hundreds of new AFM variations and their ever-widening applications. Moreover, the deflection and amplitude signals are, in their raw form, in arbitrary units which depend on the specific AFM configuration, probe, and optical detector alignments. On early AFM systems, these sometimes had to be reconfigured daily, hourly, or even more often. With today's stable instruments and robust probes, however, the calibration steps necessary to convert deflection and/or amplitude signals to actual nanometer units which can be summed as proposed are reasonably straightforward and infrequent. Regardless, the seemingly subtle improvements this approach provides can in fact be dramatic for real surfaces, during practical measurements, and especially under aggressive scanning conditions. These enhancements are particularly apparent for high-speed scanning [4,5], which is increasingly promoted in industry and academia due to the improved efficiency and novel new studies it allows [6-10].

6.4. Deflection Correction for Advanced AFM Imaging

Figure 26 provides an example of the need for height correction at increased line scan rates. The specimen is an NT-MDT TGT1 test grating, which consists of an array of sharp protrusions on a Si wafer [11]. Standard-speed, contact-mode AFM topography images (1 Hz line rates) for trace (Figure 26(a)) and retrace (Figure 26(b)) directions indicate that the protrusions are ~550 nm tall, with a 3 µm or 2.1 µm periodicity depending on orientation. Although visually similar, images of the simultaneous deflection for trace and retrace scans, Figure 26(c) and 1(d), evidence up to a

[1] Following completion of this research, a patent from D.R. Marshall (5,260,572) was discovered that describes a similar concept of combining deflection and height information (D. R. Marshall, Patent No. 5260572 (1993). However, there is no actual data in the patent filing, and no known related publications ensued.

±50 nm variation to the left and right of the protrusions. This confirms substantial error in the raw height at these locations. Figure 26(e) and (f) present the corrected height, from summing the raw height signals with their corresponding deflection. A schematic of a typical trace line scan for a simple topographic step is presented in Figure 26(g) to demonstrate how Error Corrected AFM improves the measured topography.

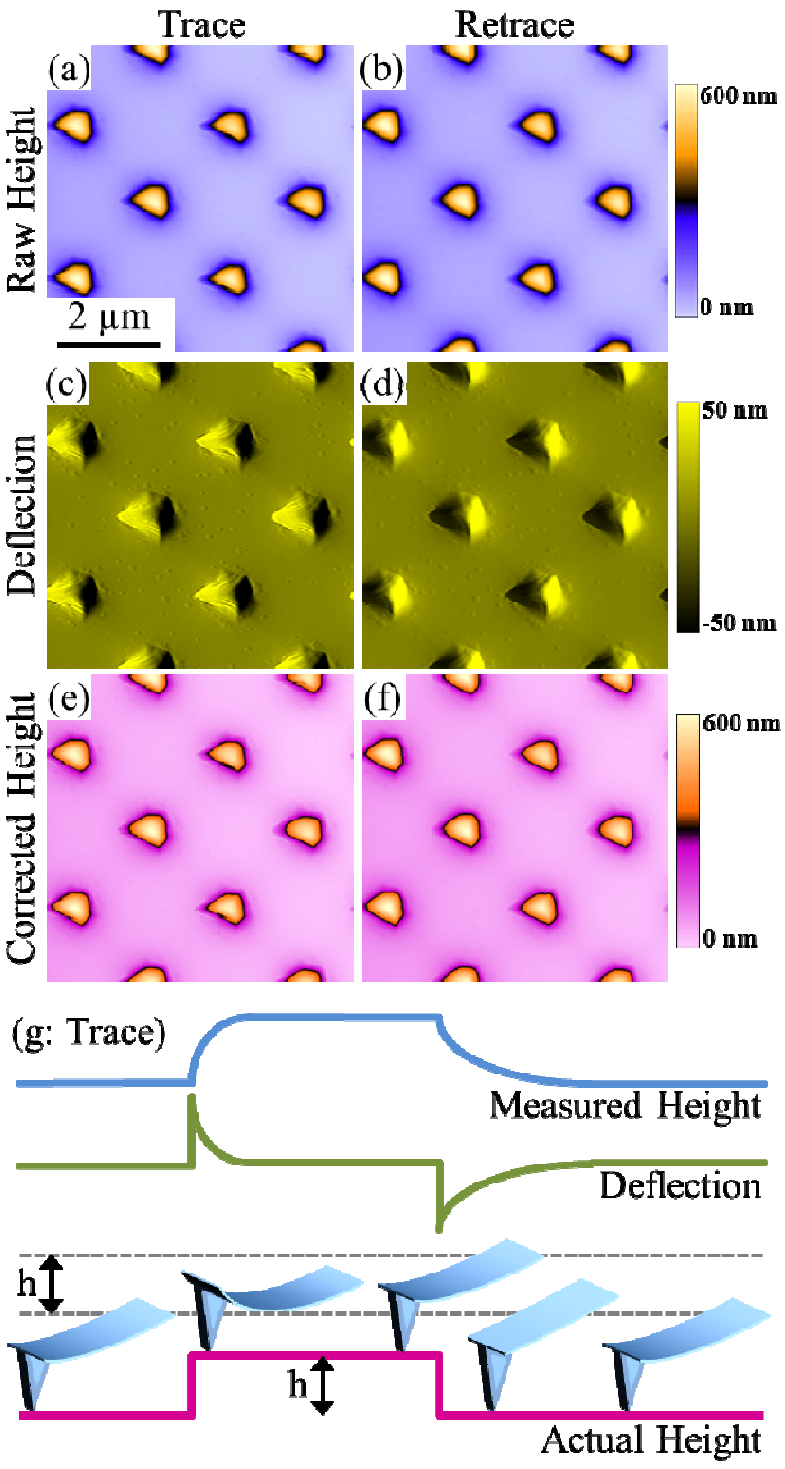

Figure 26: AFM images of a TGT1 characterization grating for trace and retrace signals acquired at a 6 Hz line scan rate and 6 µm scan size. The raw height images for trace (a) and retrace (b) are added to the deflection images (c-d) to produce the corrected height images (e-f). A schematic of a typical trace line scan and cantilever response is presented to demonstrate how measured topography is corrected by Error Corrected AFM (g).

Differences between the corrected and standard topographic maps are difficult to discern visually. Therefore, to more clearly assess the impact of this height correction, a single line scan intersecting several protrusions is extracted as a cross-section from Figure 26 where sketched, Figure 27. As the AFM tip traverses from left to right on the trace path, it is in contact with the flat substrate and is deflecting with a constant repulsive setpoint force, Figure 27(b). However, as the topography of the sample increases at the base of the test grating protrusions, the deflection of the cantilever abruptly increases. In response to this increase in deflection, the z-piezoactuator lifts to try to return to the setpoint deflection value, but never does before the apex is reached. Then, as the AFM probe traverses the peak, the deflection of the cantilever now drops below the setpoint value, and the z-piezoactuator correspondingly extends to try to return to the deflection setpoint. Of course such z-piezoactuation signals are recorded as the "height" as in Figure 27(a). Such data is used ubiquitously in the nanoscience community to present and investigate surface topography.

Obviously, there are problems with this simple approach. The speed at which the deflection is returned to its setpoint depends on the parameters of the feedback loop (typically a PID controller). Accordingly, the raw height images for trace and retrace actually slightly lag the true topography, as is very clearly shown in Figure 27(a). Beyond the sometimes substantial error this creates for measured feature heights, it also causes uphill slopes to appear to exist further right and left of their precise location for trace and retrace scans, respectively. Naturally, the opposite is true for downhill slopes. Trace and retrace data is correctly aligned, however, once the height and deflection are summed, Figure 27(c). Therefore, beyond simply correcting the vertical height, this new approach also corrects the lateral location of surface features.

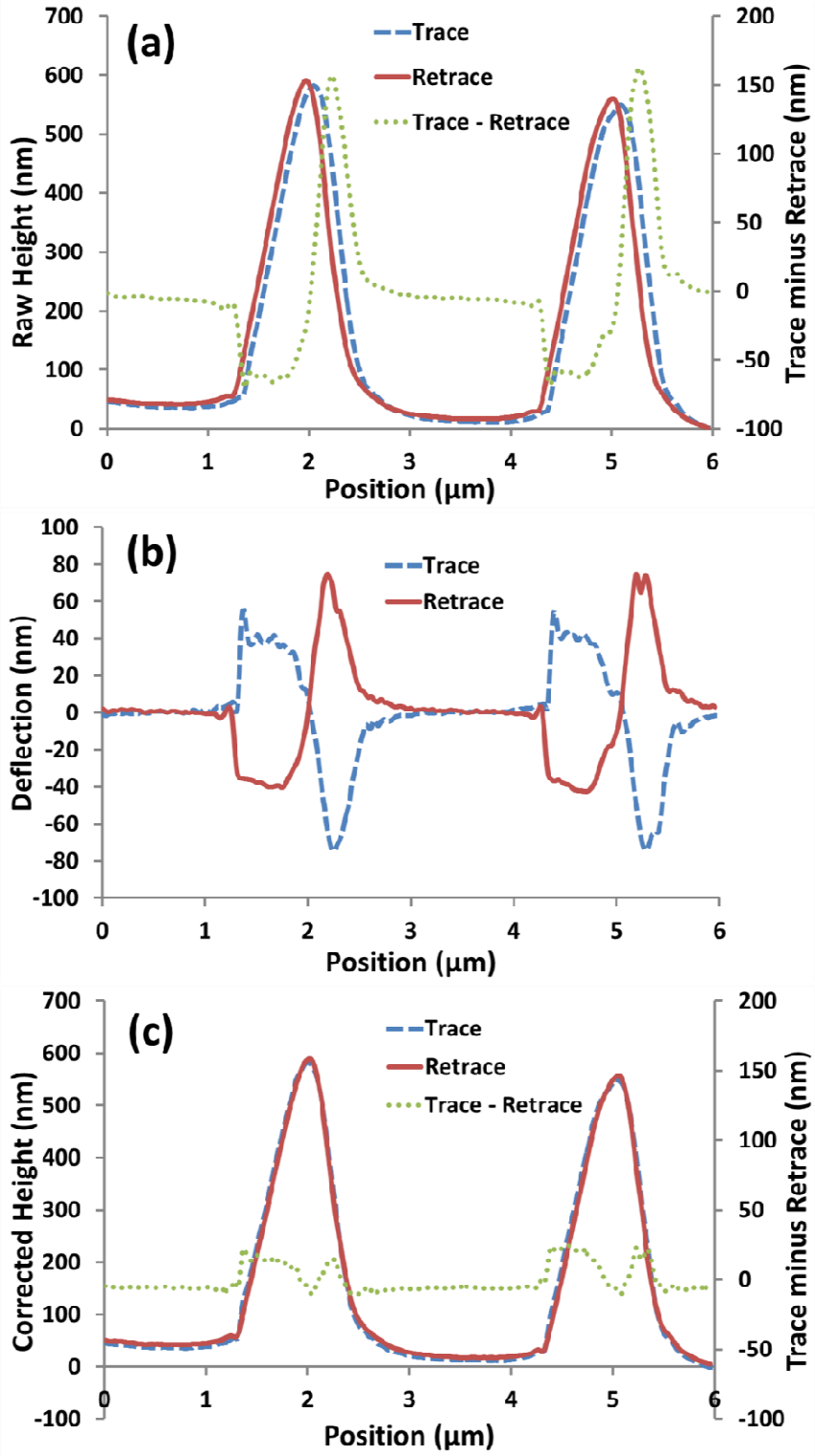

Figure 27: Raw height (a), deflection (b), and corrected height (c) trace and retrace signals from Figure 1. The trace and retrace signals are subtracted to generate a 'TMR' signal for raw and corrected height data, revealing a substantial improvement for the corrected (c) versus standard (a) topography in both height as well as lateral accuracy.

To quantify the error in topography before and after the deflection correction, each retrace signal has been subtracted from its corresponding trace signal yielding Trace Minus Retrace data ('TMR'). This TMR reveals maximum errors of more than 30% of the peak height for the raw cross-section of Figure 27(a), versus less than 5% for the corrected height, Figure 27(c).

Extending this concept to the entire images of Figure 26, Figure 28(a) presents calculated TMR maps for the raw height data, while Figure 28(b) displays TMR for the error-corrected height, with overall root mean squared deviations of 21.4 and 6.6 nm, respectively. Notably, this is for data acquired under 'optimal' imaging conditions, i.e. with a slow line scan rate (1 Hz) and strong feedback gain settings. For comparison, images equivalent to Figure 1 were next acquired with a higher line scan rate and purposely poor surface tracking (6 Hz line scan rate and a weak feedback gain). It is difficult to visually assess differences in the images themselves, but the TMR maps clarify the significant differences. Figure 28(c) presents the raw height TMR, with an abysmal standard deviation of 95.9 nm due to the poor scanning conditions. Figure 28(d), on the other hand, displays the corrected height TMR, with a substantially improved standard deviation of only 18.7 nm for the entire image.

This result implies that there is less topographic error in the 'poorly' scanned image after correction, than there is for a 'well' scanned standard height image acquired at lower scan rates. This has two very important implications for the AFM community. First, the height corrections proposed enable much higher scanning rates and hence throughput without sacrificing image quality (in fact improving it over standard practices). Second, corrected height AFM images can be remarkably insensitive to feedback loop settings, even poor ones, meaning that training of AFM users and the development of new instrumentation could be dramatically simplified.

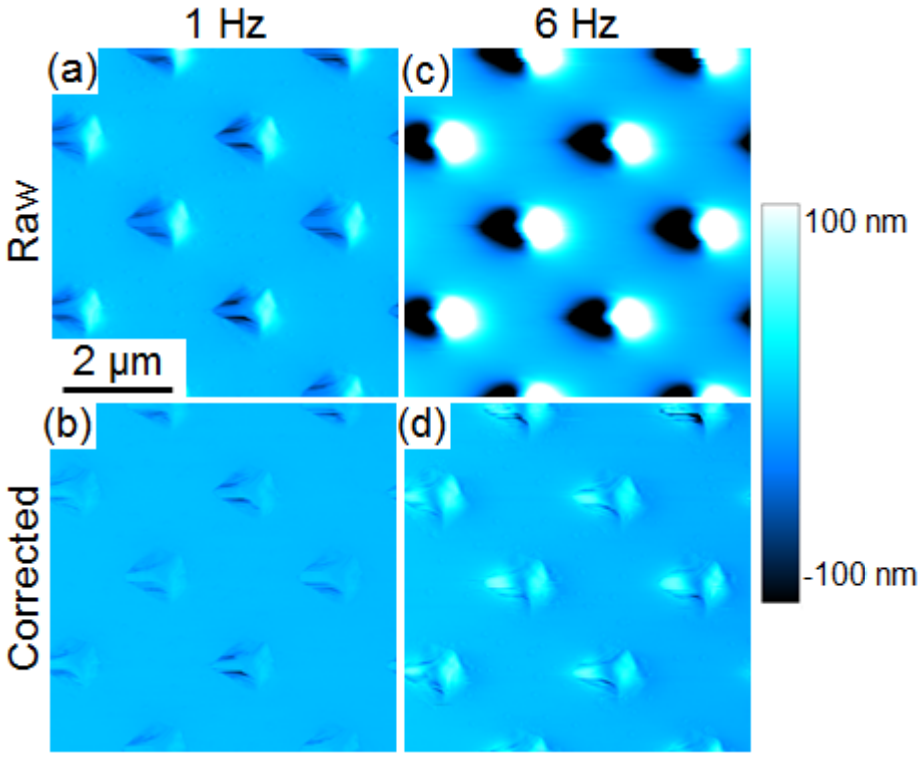

Figure 28: TMR images are shown for raw (a) and corrected (b) heights from normal scanning with a 1 Hz line rate and optimized vertical feedback loop, as well as for raw (c) and corrected (d) 6 Hz line scan rates with inferior feedback settings. The TMR standard deviations (error in measured topography) for the 1 Hz images are 21.4 nm and 6.6 nm for raw and corrected topography, respectively, but are are 95.9 nm and 18.7 nm for the lower quality 6 Hz images. Even at higher scan rates and worse tracking conditions, the corrected images are thus improvements over slower, more standard AFM height images.

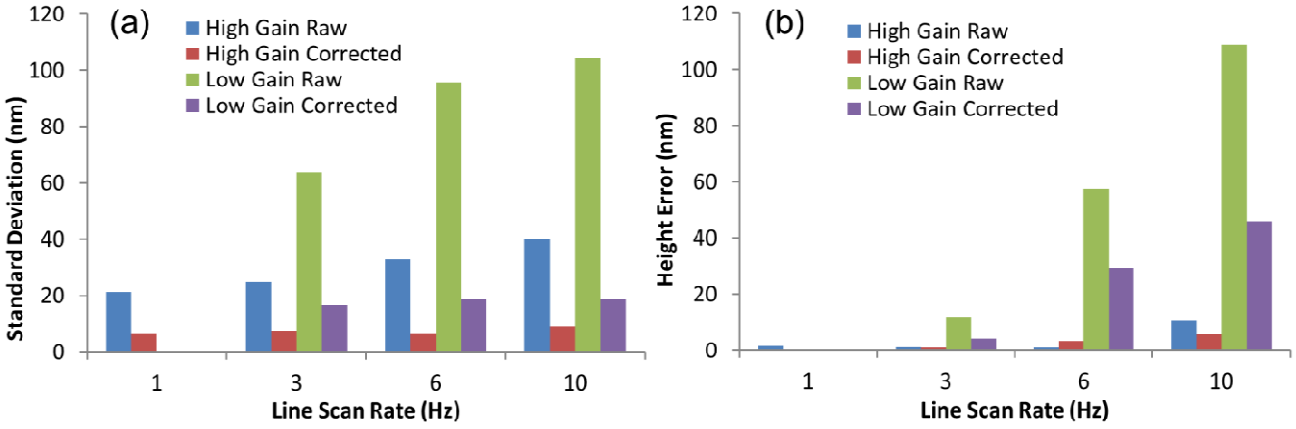

Figure 29: Standard deviation of the TMR images (a) and height error of the sharp protrusion heights (b) as a function of line scan rate and vertical feedback loop settings for a TGT1 test grating. The corrected height images with ineffective (low) feedback gains exhibit a lower error in topography than their raw, optimized (high) gain counterparts, allowing high quality corrected images to be obtained even at high line scan rates.

Figure 29(a) clarifies these points further, plotting the standard deviations of raw and corrected height TMR maps for four different line rates from 1 to 10 Hz, with both optimized ('high gain') and poor ('low gain') surface tracking. As expected, increasing the scan rate or detuning the feedback loop causes an increased standard deviation, hindering the ability to reliably map the surface with raw height data (i.e. as in most AFM applications). But the corrected height images are improved by 3.8x, 5.1x, and 5.5x, respectively for 3, 6, and 10 Hz line rates, even though the scans are not optimally acquired ('low gains'). The same trend is observed for optimal feedback loop settings ('high gain', i.e. just before high frequency ringing in the images, typically where a well-trained AFM user will operate). In this case, standard deviations improved by 3.2x (1 Hz), 3.4x (3 Hz), 4.9x (6 Hz), and 4.5x (10 Hz). In every circumstance, therefore, the corrected result is again markedly better than the normally acquired, 1 Hz, high gain data that the nanoscience community has widely accepted as a high quality, expert image for more than 25 years.

In addition to quantifying topographic errors with TMR maps, the absolute height of the sharp protrusions were measured for all line scan rates and gain settings of Figure 29(a), and compared to the height measured during a scan with optimized conditions (1 Hz, high gain, deflection corrected), Figure 29(b). The absolute heights are quite stable with a high gain, resulting in errors of less than 2% for even the highest scan rate of 10 Hz. However, as the gains are lowered, the errors in the height-only signal increase to 11% and 20% for 6 Hz and 10 Hz raw data, respectively. These inaccuracies diminish to 5% and 8% (a 49% and 58% improvement) for error-corrected 6 Hz and 10 Hz data, respectively.

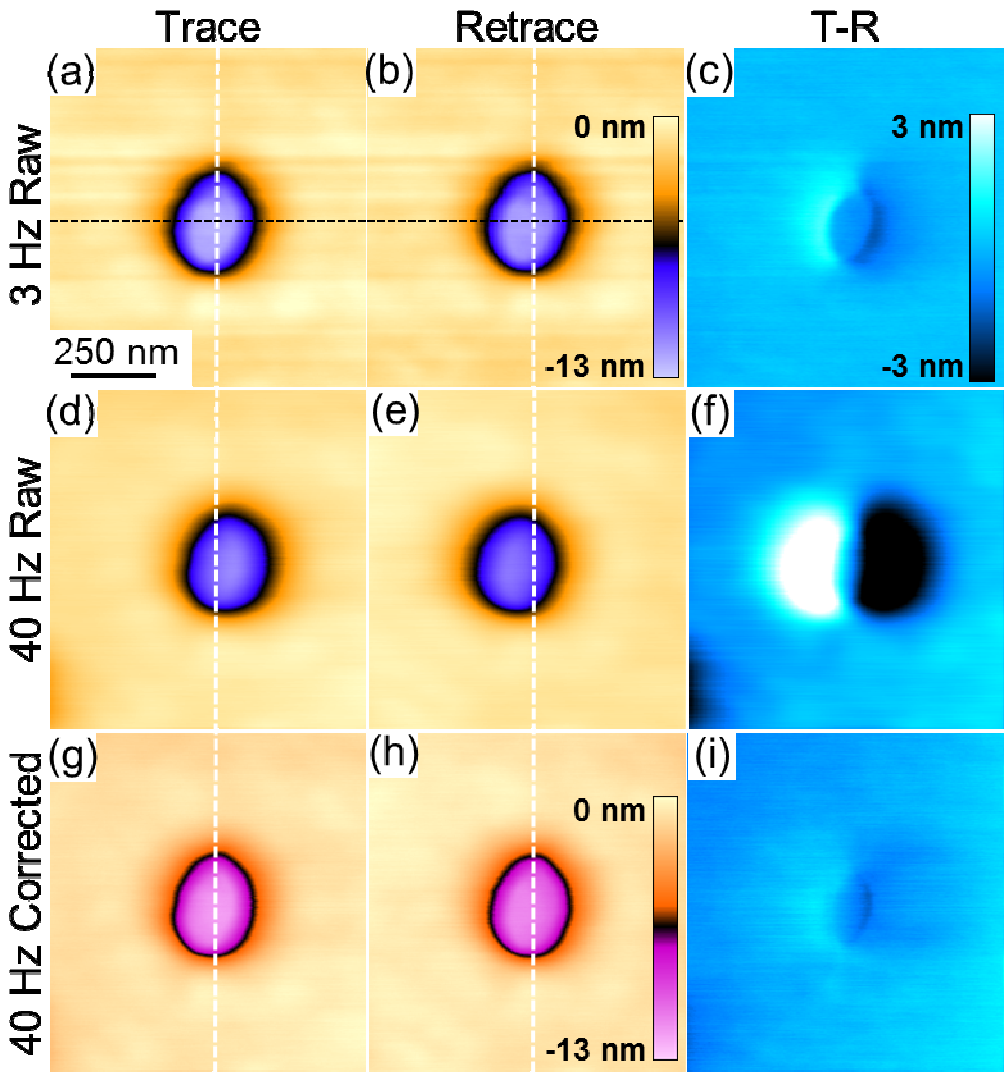

Figure 30: Raw height trace (a) and retrace (b) images acquired at 3 Hz on a SiO2 thin film with ~300 nm diameter nanopatterned pits. Raw height trace (d) and retrace (e) images acquired at 40 Hz are also displayed for the same location, along with corresponding corrected height trace (g) and retrace (h) images. TMR images calculated for the raw 3 Hz (c), raw 40 Hz (f), and corrected 40 Hz (i) signals are displayed as well. Lateral shifts apparent in the raw trace and retrace images acquired at 40 Hz (d-e) again are eliminated upon deflection correction (g-h). The standard deviations for 3 Hz raw, 40 Hz raw, and 40 Hz corrected TMR images are 0.32 nm, 1.44 nm, and 0.42 nm, respectively.

To push the limits of this approach further, height correction was applied on a nanopatterned surface at two distinct scan rates, 3 Hz and 40 Hz, for the same spatial location and uncommonly with the same exact feedback loop settings for each (Figure 30). In other words, one condition is relatively normal, while the other would be considered either extremely aggressive or downright

terrible. The specimen itself exhibits circular pits in a 14nm thick electron beam evaporated SiO_2 layer, revealing 300nm diameter circular patches of Au from an underlying thin film deposited on a silicon wafer (substrate) [12,13]. Raw height images for the trace and retrace signals at 3 Hz, Figure 30(a) and (b), exhibit a minimal horizontal shift, highlighted by the overlain vertical dashed lines. On the other hand, raw height trace and retrace images at 40 Hz, Figure 30(d) and (e), display a much greater lateral shift in the apparent feature location, far more extreme than the cases of Figure 26-Figure 28. The corresponding raw height TMR images are also shown for the 3 Hz and 40 Hz data, Figure 30(c) and (f), respectively. Clearly, the high scan rate TMR reveals drastic errors, with a standard deviation of 1.4 nm compared to 0.3 nm for the low rate data under more typical AFM conditions.

Nevertheless, after height correction the image quality returns for the 'poorly' scanned, high speed conditions, Figure 30(g,h), now appearing essentially identical to the raw height acquired at a careful 3 Hz line rate. TMR is similarly equivalent to the optimal slow image, Figure 30(i), with a standard deviation of 0.4, meaning an improvement of 3.5x compared to the raw high speed data. Putting this into context, standard images like Figure 30(a-c) require minutes to tens of minutes to acquire, whereas Figure 30(d-i) were obtained in less than just 7 seconds.

As with Figure 26-Figure 27, cross sections of these results are displayed in Figure 31(a) for the location noted. Once again, the edges are not correctly tracked in the raw high speed data, and the relatively flat base of the pit is barely resolved. With height correction, however, the results are extremely similar to that acquired 13 times slower. The left and right pit walls are aligned well, and the flat Au layer at the base of the SiO_2 pit is captured. Notice however, that the diameter between the left and right pit walls for the corrected 40 Hz signal is slightly lower than the 3 Hz signal. Also, the base of the SiO_2 pit is approximately 0.7 nm higher for the corrected

40 Hz signal. These subtle effects, unrecognizable without performing the new error correction procedure, are likely due to non-linear hysteresis and/or creep effects of the vertical and horizontal piezoactuators [14,15], but for most applications are negligible especially when balanced against the improved efficiency and ease of scanning.

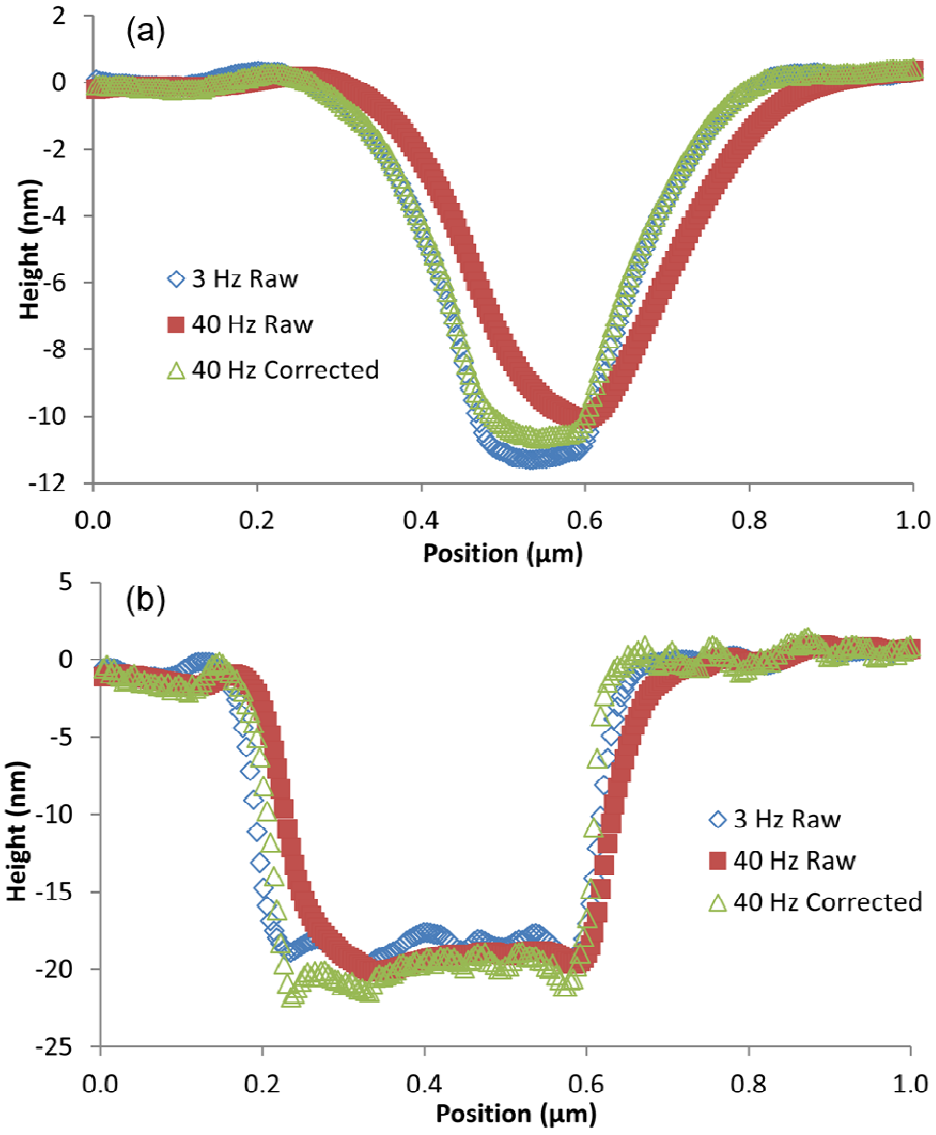

Figure 31: 3 Hz raw, 40 Hz raw, and 40 Hz corrected contact mode height trace signals (a) from Figure 30(a,d,g) where indicated by the dashed line, with equivalent 3 Hz raw, 40 Hz raw, and 40 Hz corrected AC-mode height trace signals (b) from Figure 32(a,d,g) at line scan 132. In both Contact mode and AC mode, the edges are not correctly tracked for the raw 40 Hz data, and the relatively flat base of the pit is not resolved, but upon correction the pit walls are again aligned and the shape of the Au layer at the base of the SiO_2 pit is revealed.

6.5. Amplitude Corrections for Advanced AC-Mode AFM

The same concept outlined above is equally applicable to AC-mode AFM imaging, whereby an AFM probe is oscillated at a fixed frequency and the AC amplitude indicates tip-sample interactions. Recording this amplitude during scanning, but now subtracting instead of adding it to the raw height data, provides AC corrected height images. Compared to the summation utilized for deflection based corrections (contact mode), the subtraction is necessary with AC-mode AFM because lever amplitude decreases as the tip presses into the surface, whereas the deflection increases for the same conditions. Similar to Figure 30, this is clear when contrasting slow raw height images, Figure 32(a,b), with faster raw height data (d,e), and especially with the fast corrected height (g,h). Figure 31(b) displays cross sections of these results with profiles as expected, similar to those for the paired Figure 30-Figure 31(a). Again, the corrected height doesn't just better resolve the z-dimension, but also returns feature edges to their correct locations, and helps reveal structures in the pits and on the surface.

On the other hand, there does appear to be a slight overshoot of the pit depth in Figure 31(b). This is caused by the fact that the amplitude does not rigorously vary linearly with changes in the tip-sample separation as assumed. Moreover, this variation may be slightly different on the SiO_2 mesa compared to the Au coated pit, as these surfaces are mechanically distinct [16]. Such differences amount here to less than 5% of the measured pit depth, however, a worthwhile tradeoff given the 13.3x improvement in imaging speed to just 7 seconds per frame. Meanwhile, the much more glaring difference in pit geometries for the contact and AC mode data, including a larger diameter and more abrupt edges with AC imaging, is totally independent of the correction routine. Instead, it is simply caused by the combination of using a higher aspect ratio

AFM probe for Figure 31(b) and Figure 32, and from employing AC imaging which generally allows a sharper probe to be maintained [17].

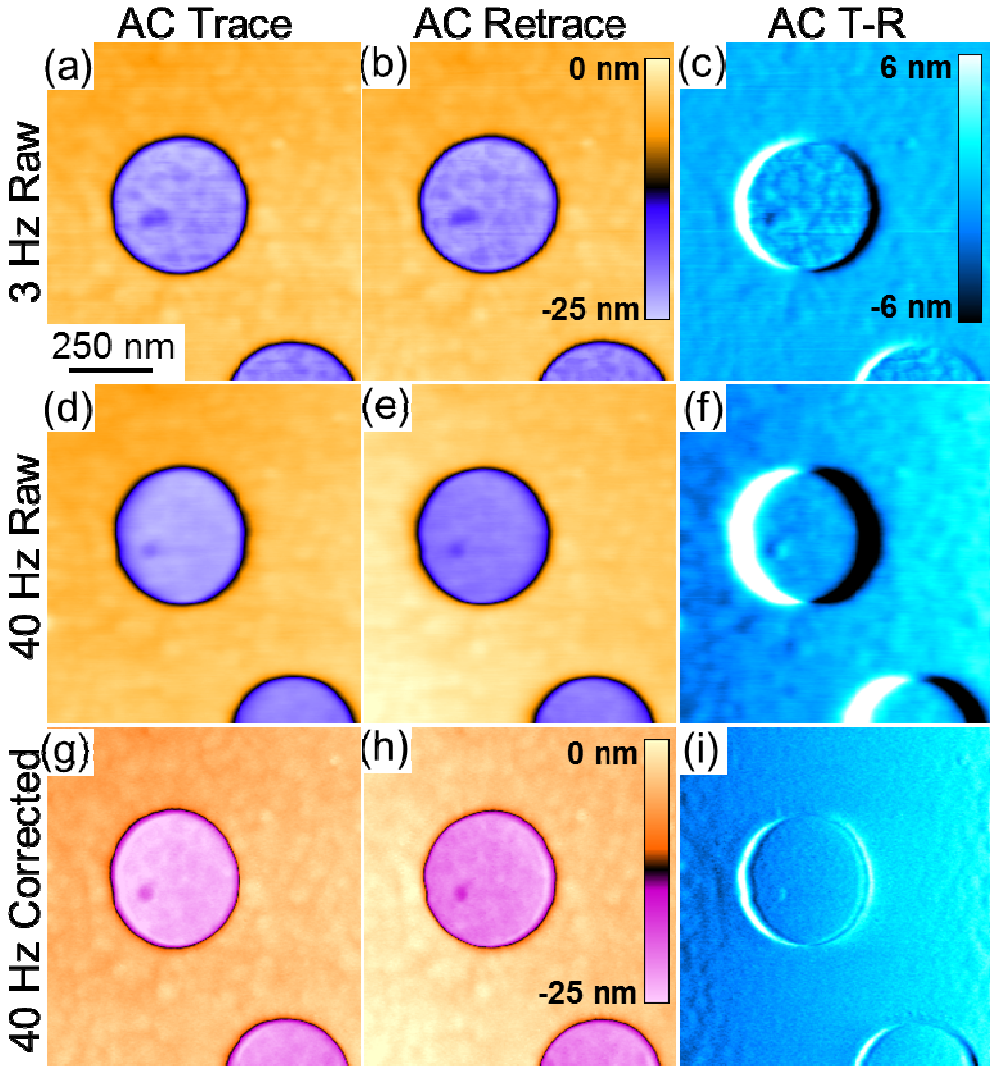

Figure 32: Raw AC mode height trace (a) and retrace (b) images acquired at 3 Hz for the same specimen as in Figure 30. 40 Hz, raw AC mode height trace (d) and retrace (e) images are also displayed for the same location, along with amplitude corrected trace (g) and retrace (h) 40 Hz height images. The TMR images for raw 3 Hz (c), raw 40 Hz (f), and corrected 40 Hz (i) height signals again reveal that the correction approach recovers features which appear lost with poor scanning for the standard height signal. The standard deviations for 3 Hz raw, 40 Hz raw, and 40 Hz corrected TMR images are 1.33 nm, 3.15 nm, and 1.66 nm, respectively.

The TMR maps for the AC AFM data are especially revealing. Beyond the standard deviation for the high speed images being corrected substantially as anticipated, features apparent in the

standard raw image (a,b) are lost in the fast raw image (d,e) but are regained upon correction (g,h). This is true for the surface roughness within the Au coated pits and the surrounding SiO_2 mesas, and for the sharp transition regions in between. Of course any simultaneous lever deflection can additionally be added or subtracted for even further correction. Typically this is rare for standard AC imaging conditions (and was here), but may become relevant for some scanning at high speeds, for increasingly challenging surfaces, or with less carefully set feedback parameters. Again, the proposed correction approach can therefore simplify, and accelerate, future AFM use.

6.6. Broad Applicability of Error Corrected AFM

Finally, since AFM is practically used to map an extensive range of surface properties far beyond simple topography, it is relevant to discuss applications of this approach to other AFM variations. Generally, the main reason that amplitude and/or deflection based corrections of raw height data are feasible and effective is that any change in height during scanning causes a calibrate-able change in deflection or amplitude. Conveniently, for many other AFM implementations, this criteria still holds. As one example, phase contrast in AC-AFM can vary linearly with small changes in the amplitude signal. Magnetic Force Microscopy and Electric Field Microscopy, for instance, leverage uniform amplitude/phase relationships to map local magnetic or electric fields, respectively [18,19]. In a simpler but much more common case, phase contrast also changes due to purely topographic influences on the AC-amplitude (due to coupling between phase, amplitude, and cantilever resonance). Knowing the functional relationship between phase and amplitude will thereby allow the phase signal to be corrected at least to first order, thus improving property measurements as well as topography.

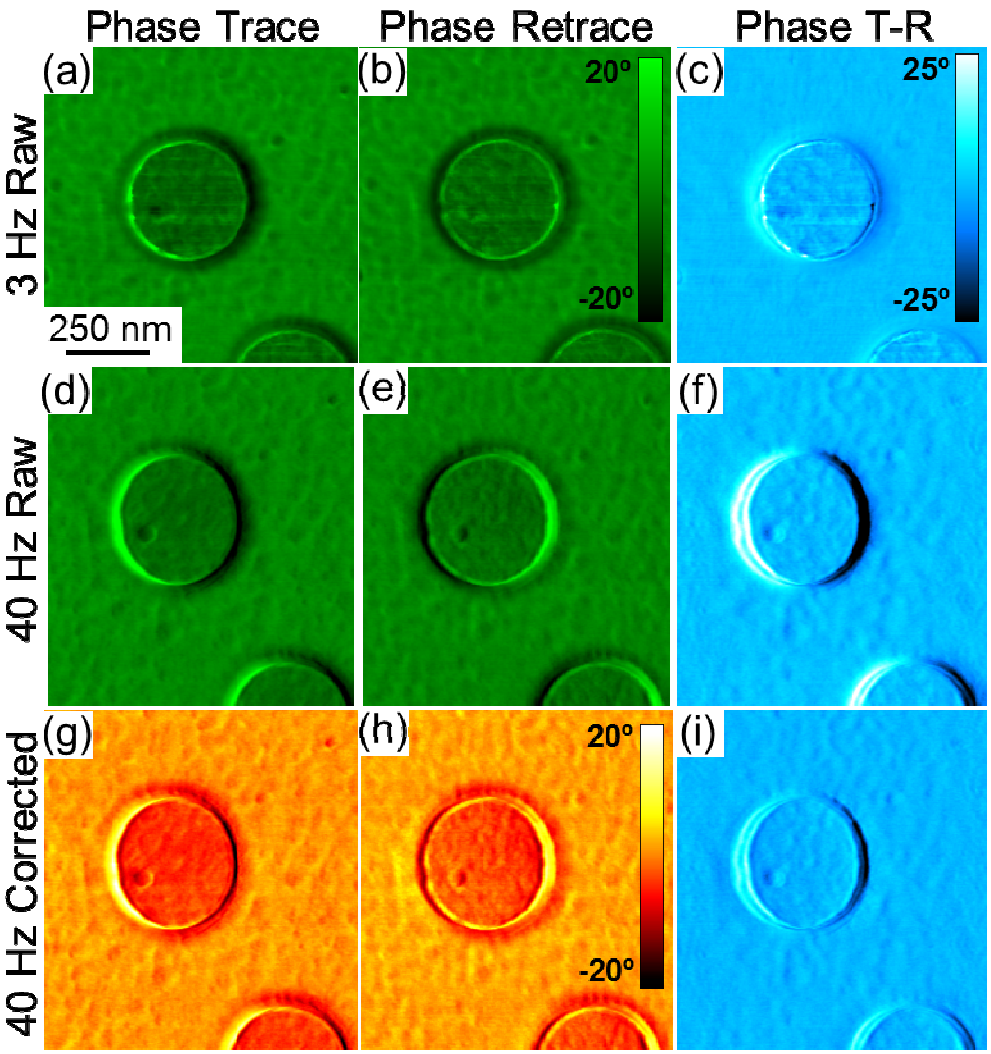

Figure 33: Phase contrast acquired simultaneously to all panels in Figure 32. This includes the raw AC mode phase trace (a) and retrace (b) images at 3 Hz, raw AC mode phase trace (d) and retrace (e) images at 40 Hz, and amplitude-corrected height trace (g) and retrace (h) images for the 40 Hz case. Corresponding TMR images for the raw 3 Hz (c), raw 40 Hz (f), and corrected 40 Hz (i) phase signals again reveal improvements by the amplitude correction procedure, here primarily by reducing artifacts especially at pit edges. The standard deviations for 3 Hz raw, 40 Hz raw, and 40 Hz corrected TMR images are 2.40º, 5.56º, and 3.02º, respectively.

Figure 33 presents corresponding trace and retrace images of raw phase contrast under normal, slow conditions (a,b), phase images acquired at faster speeds (d,e), and fast corrected phase images (g,h). The image rates are identical to those in Figure 32 as this data was in fact acquired simultaneously. Although the improvement is not as profound as with contact or AC mode topography, it is substantial for areas where the tip is not optimally interacting with the surface—

edge effects to the left and right of the pits are particularly suppressed, leading to edge error that is better than the standard imaging conditions (a,b). For property maps, the primary benefit of Error Corrected AFM will thus likely be in improving signal accuracy during such transients, which are often the locations of greatest scientific interest (interfaces, feature edges, etc.).

The corrected image could be still further enhanced if a more exact relationship than a simple linear assumption were employed to correlate amplitude and phase data. As long as that relationship can be known or predicted for this or any other data acquired by an AFM--and it usually is, otherwise the AFM mode would not be very effective--similar corrections are foreseeable to a broad range of AFM variations. Furthermore, since this approach can be achieved entirely in post-processing, it can be easily implemented for new as well as legacy AFM data and systems.

There are three important limitations to this approach that deserve attention. First, the benefits of Error Corrected AFM reach a limit whenever the tip truly leaves contact with the surface. Nevertheless, up to that point image contrast will still be better than standard imaging where one purely tracks the topography, phase, or other signals. On re-acquiring the surface, the accuracy of these signals will also return more rapidly. Second, the height correction method demonstrated here cannot remove artifacts introduced into the deflection and hence apparent height by friction forces. These effects couple through lever torsion as the scan angle approaches 90º (perpendicular to the long axis of the cantilever), and as the coefficient of friction between AFM probe and sample increase [20]. If scanning at 0º as performed here, on the other hand, friction induced lever buckling can occur. Both of these effects are negligible (sub-nm) for the experimental conditions implemented here, however [21]. Third, while the approach improves image accuracy especially for non-expert users, it cannot prolong the lifetime of the tip apex.

The newfound tolerance to poor surface tracking could even accelerate probe and/or specimen damage due to more aggressive scanning. Since the topography and other property maps are inherently better, though, and quality higher speed images are more feasible, any such damage will more readily be observable and hence correctible by modifying scanning settings and habits (automatically, or by users). Tip deconvolution [22] processes will be more accurate as well, since the surface is more accurately mapped from the outset. Of course images from ultra-sharp tips will still require expert scanning, and will still benefit, but less attention can now be paid to imaging with more blunt or wear-resistant probes (silicon nitride, diamond [23], silicon carbide [24], etc.). As nanotechnology becomes increasingly ubiquitous, simplifying AFM for non-experts without sacrificing image accuracy will enable much more widespread applications of scanning probe microscopy in general.

6.7. Conclusion

An astonishingly simple method is presented to substantially improve Atomic Force Microscopy images and operation. This Error Correction AFM approach is proven to enhance topographic contrast with both contact and AC-mode imaging, correcting normal as well as lateral flaws resulting from poor scanning conditions. Improperly set feedback parameters, a major limitation to more widespread use of AFM, can thus be overcome, simplifying future AFM operation, training, and development. The method is especially effective with high speed imaging conditions, demonstrated for images acquired in less than 7 seconds. The concept is also generally applicable to a wide range of property mapping capabilities, extending from simple phase imaging to the literally hundreds of variations of AFM that exist. Error Correction AFM can therefore significantly enhance the ease of use for current and future AFM's, the accuracy of

their results, their efficiency, and hence their expanding applicability to solve diverse challenges at the nanoscale.

6.8. Experimental

This work was implemented on an Asylum Research Cypher AFM. Contact mode measurements were performed with NanoSensors CDT-CONTR probes with a range of imaging parameters as described. AC-mode AFM was achieved with AppNano ACCESS-UHF probes. All analysis was performed in post-processing using simple additions of simultaneously acquired topography and deflection signals (contact mode), or subtractions of topography and amplitude signals. The deflection and amplitude signals were calibrated from their detected units of volts to relevant units of nm using widely implemented procedures. Specifically, the tip is brought into contact with a relatively non-compliant surface (glass), and then the z-actuator is extended a known distance (nominally <10 nm). The corresponding change in cantilever deflection or amplitude is recorded in volts, which must be the same as the actuated distance in nm assuming the tip does not slide or indent into the substrate. This reveals the optical lever sensitivity in nm/V. The same process was followed for AC mode calibration, though the phase signal was also recorded to determine the slope of the change in phase versus change in amplitude used for Figures 6-8. In each of the experiments, feedback gain settings have been specified as ‘low’ (poor) or ‘high’ (optimized). Although such parameters are completely system dependent, in our case for contact mode scanning on the TGT1 characterization grating the ‘high’ gain setting corresponds to a 20, 50, 80, and 100 integral gain for 1 Hz, 3 Hz, 6 Hz, and 10 Hz scan rates, respectively. The ‘low’ gain setting corresponds to an integral gain value of 15 for all scan rates. For contact mode scanning on the SiO_2 thin film, an integral gain of 20 was used for both 3 and 40 Hz scan rates.

For AC-mode scanning on the SiO_2 thin film, integral gains of 30 and 100 were used for 3 and 40 Hz scan rates, respectively.

For quantitative comparisons of improvements in image quality between common AFM data and the presented error corrected technique, trace and retrace images were subtracted to produce 'Trace Minus Retrace' images. Such 'TMR' cross sections or images are thus ideally featureless, with minimal standard deviations. In practice they never are, however, due to three quantifiable components. The first is the error inherent in only considering topography (height) data, which our approach substantially corrects by incorporating deflection (contact mode) or amplitude (AC-mode) signals as described in this work. The second is random instrumental noise, which leads to a non-zero baseline or standard deviation for TMR data. The third stems from system-dependent instrumental errors, typically due to either hysteresis in the x/y piezoactuators, or synchronization errors between signal detection and recording (i.e. a consistent error in pixel positions). Such error is primarily a function of scan rate, image size, or piezo offsets [14], consistent within the specific settings.

Therefore, to quantify our error-corrected AFM approach independent of the instrumentation employed, a standard one-dimensional cross correlation (LabVIEW) has been performed between trace and retrace topography images for each scan rate considered (image sizes and piezo-offsets were kept fixed). The number of pixels, and hence nanometers, of the resulting lateral shift necessary to best overlap the initial topography image is presented in Table 2. The same shift was then reasonably employed to corresponding deflection, amplitude, or phase data, regardless of gain settings as they do not influence the consistent system error. Without this procedure, the Trace Minus Retrace (TMR) image variations (e.g. Figure 28), and TMR standard deviation values (i.e. Figure 29) would indicate even greater, though system-dependent, errors

than reported, and correspondingly with still better improvements for the error correction procedure. The image correlation procedure therefore removes such instrument-specific error, leaving the improvement in AFM image quality by the presented error-correction approach to be directly analyzed.

Table 2: Number of pixels, and hence nanometers, required to shift trace and retrace images acquired for the noted scan rates in order to remove consistent error due to piezoactuator hysteresis and/or detection/position synchronization errors. The contact mode images were acquired with 1024 image pixels and a 6 µm scan size, while AC mode images were acquired with 256 image pixels and a 1 µm scan size.

	Contact Mode				AC Mode	
Scan Rate (Hz)	1	3	6	10	3	40
Shift (pixels)	4	5	7	10	5	18
Shift (nm)	23.4	29.3	41	58.6	19.5	70.3

6.9. References

1. G. Binnig, C. F. Quate, and C. Gerber, Phys Rev Lett **56** (9), 930 (1986).
2. S. Belikov C. Su, (1/2011 2011).
3. P. I. Mininni, J. R. Osborne, J. M. Young, and C. R. Meyer, Patent No. 7665349 B2 (2010).
4. N. S. Tambe and B. Bhushan, Journal of Physics D-Applied Physics **38** (5), 764 (2005).
5. Z. H. Tao and B. Bhushan, Review of Scientific Instruments **77** (10) (2006).
6. B. D. Huey, R. N. Premnath, S. Lee, and N. A. Polomoff, J. Am. Ceram. Soc. **95** (4), 1147 (2012).
7. T. Uchihashi and T. Ando, J Physiol Sci **63**, S41 (2013).
8. T. Sulchek, R. Hsieh, J. D. Adams, S. C. Minne, C. F. Quate, and D. M. Adderton, Review of Scientific Instruments **71** (5), 2097 (2000).
9. T. Ando, T. Uchihashi, and N. Kodera, Annu Rev Biophys **42**, 393 (2013).
10. T. Ando, N. Kodera, E. Takai, D. Maruyama, K. Saito, and A. Toda, P Natl Acad Sci USA **98** (22), 12468 (2001).
11. NT-MDT, (2013).
12. Per Hanarp, Duncan S. Sutherland, Julie Gold, and Bengt Kasemo, Colloids Surf., A **214** (1–3), 23 (2003).
13. Jenny Malmstro□m, Brian Christensen, Hans P. Jakobsen, Jette Lovmand, Rasmus Foldbjerg, Esben S. Sørensen, and Duncan S. Sutherland, Nano Lett. **10** (2), 686 (2010).
14. D. Croft, G. Shed, and S. Devasia, J Dyn Syst-T Asme **123** (1), 35 (2001).
15. K. K. Leang and S. Devasia, Ieee T Contr Syst T **15** (5), 927 (2007).
16. Bryan D. Huey, Annu. Rev. Mater. Res. **37** (1), 351 (2007).

17. Y. Martin, C. C. Williams, and H. K. Wickramasinghe, J. Appl. Phys. **61** (10), 4723 (1987).
18. D.. Bonnell, (Wiley-VCH, New York, 2001).
19. J. P. Cleveland, B. Anczykowski, A. E. Schmid, and V. B. Elings, Applied Physics Letters **72** (20), 2613 (1998).
20. R. Piner and R. S. Ruoff, Review of Scientific Instruments **73** (9), 3392 (2002).
21. R. J. Warmack, X. Y. Zheng, T. Thundat, and D. P. Allison, Review of Scientific Instruments **65** (2), 394 (1994).
22. U. Hubner, W. Morgenroth, H. G. Meyer, T. Sulzbach, B. Brendel, and W. Mirande, Appl. Phys. A: Mater. Sci. Process. **76** (6), 913 (2003).
23. K. H. Chung and D. E. Kim, Ultramicroscopy **108** (1), 1 (2007).
24. M. A. Lantz, B. Gotsmann, P. Jaroenapibal, T. D. B. Jacobs, S. D. O'Connor, K. Sridharan, and R. W. Carpick, Adv Funct Mater **22** (8), 1639 (2012).

Chapter 7: Physical Mechanisms of MHz Vibrations and Nonlinear Detection in Ultrasonic Force and Related Microscopies

7.1. Abstract

Use of high frequency (HF) vibrations at MHz frequencies in Atomic Force Microscopy (AFM) advanced nanoscale property mapping to video rates, allowed use of cantilever dynamics for mapping nanomechanical properties of stiff materials, sensing μs time scale phenomena in nanostructures, and enabled detection of subsurface features with nanoscale resolution. All of these methods critically depend on the generally poorly characterized HF behaviour of AFM cantilevers in contact with a studied sample, spatial and frequency response of piezotransducers, and transfer of ultrasonic vibrations between the probe and a specimen. Focusing particularly on Ultrasonic Force Microscopy (UFM), this work is also applicable to waveguide UFM, Heterodyne Force Microscopy, and Near-Field Holographic Microscopy, all methods that exploit nonlinear tip-surface force interactions at high frequencies. Leveraging automated multidimensional measurements, spectroscopic UFM (sUFM) is introduced to investigate a range of common experimental parameters, including piezotransducer excitation frequency, probed position, ultrasonic amplitude, cantilever geometry and spring constant, and normal force. Consistent with studies of influence of each of these factors, the data-rich sUFM signatures allow efficient optimization of ultrasonic-AFM based measurements, leading to best practices recommendations of using longer cantilevers with lower fundamental resonance, while at the same time increasing the central frequency of HF piezo-actuators, and only directly comparing results within areas on the order of few μm^2 unless calibrated directly or comparing with in-the-imaged area standards. Diverse materials such as Si, Cr and photoresist are

specifically investigated. This work thereby provides essential insight into the reliable use of MHz vibrations with AFM, and provides direct evidence substantiating phenomena such as sensitivity to adhesion, diminished friction for certain ultrasonic conditions, and the particular benefit of UFM and related methods for nanoscale mapping of stiff materials.

7.2. Foreword

As part of the NSF and EPSRC Materials World Network program, an international collaboration was made with Dr. Oleg Kolosov's Nanoscale Microscopy Group in the Department of Physics at Lancaster University, Lancaster, UK. This funding supported the exchange of two students to investigate the optimization of phase change memory materials for future data storage applications. Previous experiences gained with instrumentation, programming, and scanning probe microscopy were directly applied to help improve Dr. Kolosov's invention of ultrasonic force microscopy (UFM), a variant of AFM for the measurement of nanomechanical properties and subsurface artifacts. The following chapter outlines the newly developed spectroscopic ultrasonic force microscopy (sUFM) approach, and is directly applied to materials of varying mechanical properties as a proof of concept.

7.3. Introduction

The invention of the atomic force microscope (AFM) [1] and its development over the past several decades has provided a powerful means for surface characterization on the nanoscale. Various dynamic scanning modes have since been developed to measure nanomechanical properties and subsurface features with nanometer lateral resolution, with property mapping capabilities approaching video rates [2]. These scanning modes, including high frequency (HF) tapping mode [3-6], Ultrasonic Force Microscopy (UFM) [7-13], waveguide UFM [14], Atomic Force Acoustic Microscopy (AFAM) [15-19], Heterodyne Force Microscopy (HFM) [20-22],

and Scanning Near-Field Ultrasound Holography (SNFUH) [23,24] all implement HF vibrations in the MHz range for their operation. They are the only methods available to reliably map the nanoscale elastic moduli of high stiffness materials, such as oxides, metals, and semiconductors. They have also been shown to minimize tip and sample wear due to ultrasound induced lubricity, advantageous for the characterization of soft materials including cells, proteins, and polymers [25].

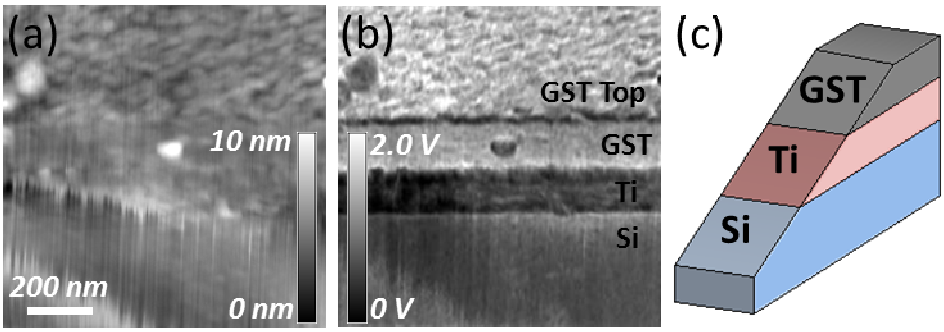

Figure 34: Typical topography image (a) and nanomechanical UFM map (b) for various materials $Ge_2Sb_2Te_5$ (GST), Ti, and Si substrate. Sample was prepared by beam exit ion cross sectioning (BEXP) [26], with schematic of sample geometry presented in (c).

For standard operation of these techniques, the piezotransducer is typically excited at a constant high frequency (ideally at or close to transducer resonance) with a constant (HFM, SNFUH, AFAM) or amplitude modulated (UFM) excitation amplitude, and the low frequency (LF) cantilever response is acquired for the surface characterization. One expanding study to cross-sections of thin films is shown in Figure 34. Detection is achieved by monitoring deflection of the AFM cantilever, usually at distinct or swept frequencies with a lock-in amplifier. Taking UFM as an example [7], its contrast originates in the nonlinear "rectification" of HF vibrations of the sample (sample UFM) or cantilever (waveguide UFM). When this vibration is amplitude modulated with a low frequency waveform, as e.g. shown at (A) in Figure 35(a), the cantilever

experiences a characteristic oscillating “ultrasonic” force at the modulation frequency, producing the UFM response U_z (B).

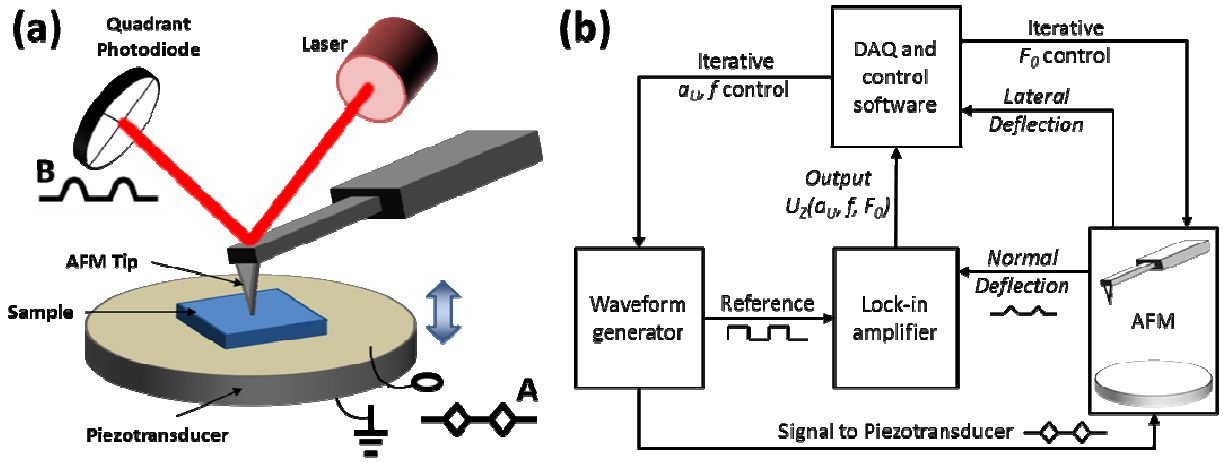

Figure 35: Schematic of UFM Operation (a) and the block diagram of data acquisition signal routes for sUFM technique (b).

Unfortunately, these and indeed any high frequency excitations in probe microscopy can excite a wide range of geometrically defined, and sometimes spectrally overlapping modes and/or overtones of the cantilever oscillations. The vibrations are further dependent on the resonant response of the driving piezotransducers (spatial and frequency), as well as the non-linear effective transfer function at the tip-sample junction. These challenges make it difficult to universally distinguish between material dependent sample properties and piezotransducer/cantilever effects, even though clear contrast has been demonstrated for many material systems experimentally and theoretically [2].

Ideally, the materials-sensitive response would only scale with material dependent mechanical property variations [2]. Therefore, it becomes important to understand how the MHz dynamics of the piezotransducer and cantilever influence the ultrasonic response as a function of the various parameters employed in any of the HF dynamic scanning modes. Accordingly, this work

presents a multidimensional spectroscopic technique, specifically applied for spectroscopic Ultrasonic Force Microscopy (sUFM), which couples AFM with external data acquisition hardware and software to automatically map the response of the cantilever (U_Z) to the nonlinearly detected ultrasonic force as a function of average normal force (F_0), piezotransducer frequency (f), and ultrasonic excitation amplitude (a_u), Figure 36.

In addition to better understanding the interplay of user selectable factors, such as F_0, f, a_u, this multiparametric approach is also used via "design of experiment" methodology allowing to isolate the trends for optimization of UFM configuration and to investigate the influence of common experimental parameters such as piezotransducer vs. cantilever resonance frequency, as well as the measurement location. Such a study allows optimization of UFM measurements, as demonstrated by applying sUFM to a diverse range of materials – metallic Cr layer, semiconducting SiO_2, and compliant developed photoresist patterns. The known relationship between UFM response and friction reduction [25,27] is investigated throughout the multidimensional experiment as well.

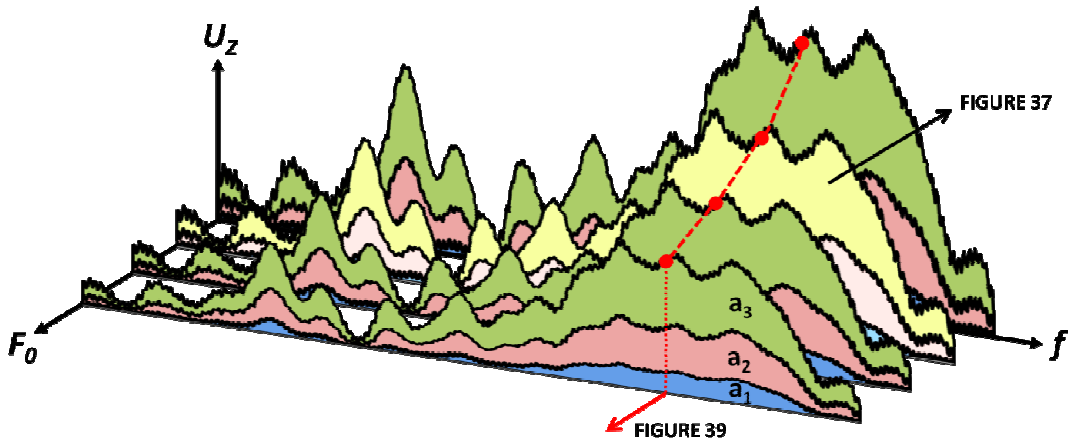

Figure 36: Schematic representation of the multidimensional spectroscopic Ultrasonic Force Microscopy (sUFM) technique. The typical ultrasonic response U_z is acquired as a function of piezotransducer frequency f, average set-point force F_0, and ultrasonic amplitude a_u. Highlighted U_z vs. f response demonstrates the Figure 37 schematic, while red (color online) dash-dot of U_z vs. F_0 demonstrates the Figure 39 schematic.

7.4. Methods

All ultrasonic force microscopy measurements were performed on Bruker Multimode (with Nanoscope IV controller) and Asylum Research Cypher AFM systems in ambient environments. Figure 35(a) presents the schematic diagram for the measurement setup. Each sample was mounted on a piezotransducer with crystalline salol (phenyl salicylate) to maximize ultrasonic contact. Soft flexible wires were soldered to both sides of the piezotransducer placed on an AFM stub, allowing an external function generator (Agilent 33220A) to excite ultrasonic vibrations in the sample at or near the resonant frequency of the piezotransducer. As is normal for UFM, the driving voltage consisted of a HF sine carrier wave with an amplitude modulation defined by a triangular-shaped arbitrary waveform, represented by signal A in Figure 35(a). The frequency of the arbitrary waveform f_m was fixed at 2.71 kHz - slightly higher than each AFM's vertical feedback loop, but not high enough to excite cantilever resonances. The displacement of the AFM tip in the z direction at the modulation frequency, originates in the "rectification" due to the nonlinear transduction of ultrasonic sample vibrations by the tip-sample junction, was then captured in the normal deflection signal (signal B in Figure 35(a)), detected by a position sensitive quadrant photodiode standard in AFM. It should be noted that in UFM the sample ultrasonic vibration occurs at very high frequency well above the cantilever resonances, with the cantilever displacement at this frequency practically negligible [28] whereas the UFM signal itself is produced by the change of average force at the modulation frequency occurring within the f_m kHz range [7]. The AFM response to the cantilever deflection at these frequencies can be directly calibrated providing data in units of vertical cantilever displacement. The normal deflection signal from the AFM was input to a lock-in amplifier (Stanford Research Systems 830), with the modulation frequency f_m as a reference signal provided by the external waveform

generator. The UFM amplitude U_z at the first harmonic of the modulation frequency was then extracted, with lock-in averaging times and sensitivities of 10 ms and 50 mV full scale, respectively. The carrier sine wave amplitude a_u and frequency f, along with tip-sample set-point force F_0, were incrementally controlled by GPIB commands from National Instruments LabVIEW software on a stand-alone computer. The ultrasonic amplitude $U_z(a_u, f, F_0)$ and lateral deflection signals were input to the software through a National Instruments PXIe-6124 data acquisition card. Figure 35(b) presents the signal routes for the sUFM scheme.

Three different AFM probes covering a range of cantilever lengths and spring constants were considered in the present work, with parameters presented in Table 3. For each, the spring constant and optical lever deflection sensitivity was calibrated in-situ using Sader method [29]. The optical lever deflection sensitivity of each probe, and the lock in sensitivity, was used to convert the ultrasonic response from arbitrary units of V_{RMS} to real dimensions of nm_{RMS}.

Two distinct piezotransducers were employed (PI, 16 mm disks, wrapped Ag electrodes) with nominal resonant frequencies of 2 MHz (0.5 mm thickness) or 4 MHz (0.25 mm thickness). With this equipment, three thin film materials were investigated. The first was a 300 nm thick SiO_2 thermal oxide on a Si wafer (IDB Technologies). The second was a 500 nm layer of S1805 photoresist spin coated onto a SiO_2 wafer then patterned by exposure to UV light and developed. The third was a 30 nm thick Cr layer, magnetron sputtered (Moorfield MiniLab) onto the SiO_2/Si wafer at a rate of 0.5 Å/s. All samples were cleaned by sequential sonication in acetone, IPA, DI water. Plasma cleaning in O_2/Ar was performed before attachment to the piezotransducers.

Table 3: Cantilevers considered in the present work. Manufacturers specifications are listed, with in-situ measurements displayed in parentheses. The cantilever designations at left are referred to throughout the paper.

Cantilever designation	Cantilever Name	Length (μm)	Force Const (N/m)	Res. Freq. (kHz)
Short	NSG03 (NT-MDT)	135 ± 5	0.35 – 6.1 (2.6)	90
Force Modulation	Multi75-G (Budget Sensors)	225 ± 5	1 – 7 (3.0)	75 ± 15
Standard	Contact-G (Budget Sensors)	450 ± 10	0.07 – 0.4 (0.2)	13 ± 4

7.5. Results and Discussion

7.5.1. Influence of Cantilever and Piezotransducer Frequency Range

Figure 36 presents the typical UFM response U_z as a function of user selectable factors – set force F_0, ultrasonic frequency f, and ultrasonic drive amplitude a_u. We found that the set force and drive amplitude influences the response in a consistent manner – an increase of a_u and decrease of F_0 leads to a monotonous increase of U_z – these will be studied in more detail later in the paper. At the same time, Figure 36 shows that frequency variation makes much more profound and less regular effect. In order to study the influence of frequency, we selected two piezotransducers of the same geometry (round disks) but of significantly (2-fold) different central frequency that nevertheless lies within the frequency range most widely used in the nonlinear UFM and HFM related methods as reported by various groups [23,30-32]. We also selected three generally used in UFM/HFM contact cantilevers types with fundamental vibrational modes from 12 to 90 KHz and spring constant differing by the order of magnitude (see Table I). We then studied sUFM response for all these piezotransducer-cantilever combinations by sweeping UFM frequency around the central frequency of each piezotransducer as well as by varying ultrasonic drive voltage.

Figure 37 exemplifies the multidimensional ultrasonic response U_z (y axes) for this study. Specifically, U_z is plotted as a function of the excitation frequency f (x axes) and ultrasonic amplitude a_u (distinct spectra), for three different cantilever types (rows) by length and resonance frequency (Table 3) and also at two piezotransducers with 2.0 and 4.3 MHz central frequency (columns). Figure 37(a-c) are collected for the short, force modulation, and standard cantilevers on a 2 MHz piezotransducer, respectively. Figure 37(d-f) are collected with the same cantilevers on a 4 MHz piezotransducer. Each measurement was performed by contacting the AFM tip to the sample at a fixed point (no sample rastering) and incrementally sweeping frequency and ultrasonic amplitude at a fixed normal force. Several observations can be made regarding the piezotransducer and cantilevers chosen. In general, as expected, the ultrasonic response increases with ultrasonic amplitude. Also, the response for the 4 MHz transducer is more uniform over a wider range of frequencies (~200 kHz versus 10-50 kHz or less for the 2 MHz transducer). The more smooth spectral response most likely originates from reduction of the HF vibration transfer to the cantilever as the frequency increases [28] and is clearly desired, as it reduces the frequency dependence for qualitative or quantitative comparisons of different materials by UFM. The response stability versus frequency is demonstrated in Figure 37(f) for a standard cantilever on 4 MHz piezotransducer. The standard deviations are 13%, 10%, and 8% of the average U_z signal for 2, 4, and 6 V_{PP} ultrasonic amplitudes.

These results prove that optimal UFM characterization should be performed with a combination of long cantilevers (low spring constants and resonant frequencies) with HF piezotransducers. Both of these selections allow better damping of spurious resonances in both the sample and the cantilever. This directly corroborates simple previous observations that higher modes of

cantilever vibration become negligible if the primary resonance frequency is low compared to the operating piezotransducer frequency [7].

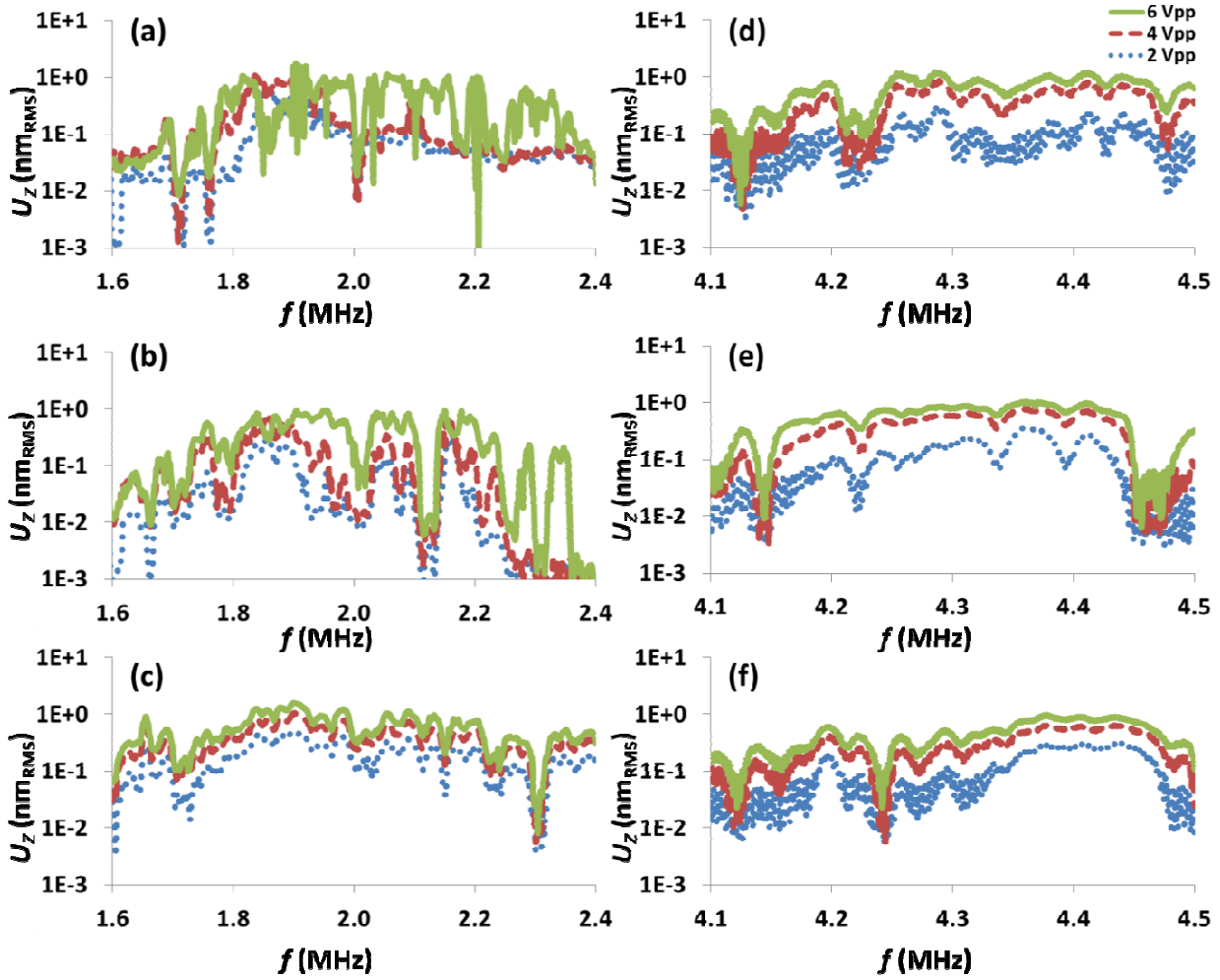

Figure 37: Ultrasonic response U_z (y axes) as a function of frequency f (x axes) and ultrasonic amplitude a_u (distinct spectra) for short (a,d), force modulation (b,e), and standard cantilevers (c,f) on 2 MHz (a-c) and 4 MHz (d-f) piezotransducers. Each U_z point is an average of lock-in output for 500 ms (50 data points with 10 ms time constant). Each frequency sweep was acquired with a constant set-point force between tip/sample of 0.5 V, corresponding to 80, 130, and 20 nN for short, force modulation, and standard cantilevers, respectively.

7.5.2. Influence of Position across Piezotransducer

Once the optimal cantilever (standard cantilever) and piezotransducer (4 MHz) combination was determined to produce an optimal U_z response, it was implemented for all subsequent measurements to further investigate the factors that influence UFM contrast and reliability.

Figure 38(a) presents the positional dependence of U_z versus excitation frequency f for 5 locations, each spaced 100 μm apart across a SiO_2 sample mounted at the center of the 16 mm diameter piezotransducer. Only data at 4 V_{PP} are shown, with other ultrasonic drive amplitudes a_u (2 and 6 V_{PP}) yielding analogous results.

While an optimal "flat" region for the U_z *vs.* f response exists for every condition, typically over a ~100 kHz frequency range for 4 MHz disc resonators as with Figure 37(d-f), the specific response is consistently found to depend on location as would be expected for the non-damped simple disk transducers [33] that are commonly used in UFM and HFM applications due to their high response and simple geometry. To investigate this effect further, Figure 38(b) displays the average of all 5 $U_z(f)$ (UFM vs frequency) curves from Figure 38(a), including standard deviation error bars. Even in the frequency range with the most consistency as a function of position, here from roughly 4.3 to 4.4 MHz, the standard deviation is at least 25% of the ultrasonic response (note the log scale).

Approaching this issue from a different perspective, Figure 38(c) presents the UFM response as a function of position for 5 discrete frequencies. At distances on the order of 1000 μm, the variability in high frequency SPM signals may thus reach an order of magnitude. The characteristic length scale of such variations is linked with the ultrasonic wavelength [33] $\Lambda = v_u / f$ where v_u is the speed of sound in the piezotransducer. For the 2 and 4 MHz PZT piezotransducers studied here, Λ is *ca.* 2000 and 1000 nm, respectively. These observations provide important factors to consider for appropriate specimen and transducer selection.

Conveniently, though, these gross variations in ultrasonic response are practically eliminated on the scale of most scanning probe microscopy measurements, which are typically 2-3 orders of

magnitude smaller (few μm) and are only a small fraction of the ultrasonic wavelength Λ. It is thus the variability of ultrasonic signals on the μm length scale that is instead relevant when comparing results within HF SPM images. To test the extent of this phenomenon, Figure 38(d) presents a UFM line scan averaged from 256 rows of a 3 μm x 3 μm UFM image for a 30 nm Cr thin film. The standard deviation of the ultrasonic response at each point, also based on 256 measurements along an essentially 3 μm long column, is between 22 and 28% of the total response with a mean of 25% (again note the log scale). Therefore, in order to determine the absolute ultrasonic response and stiffness of various materials at the nanoscale, data should only be compared within smaller images (up to 10 μm) without additional calibration. To compare measurements from separate specimens, or widely spaced positions (more than tens of μm), one should either use adjacent regions of some kind of standard reference (e.g. an underlying substrate), or independent calibration (e.g. via laser Doppler Vibrometry) [33]. Of course in the event of HF measurements where the cantilever is excited instead of the sample [14], this limitation is removed, and other challenges can instead dominate relating to varied lever actuators, as well as the waveguide efficiency and uniformity.

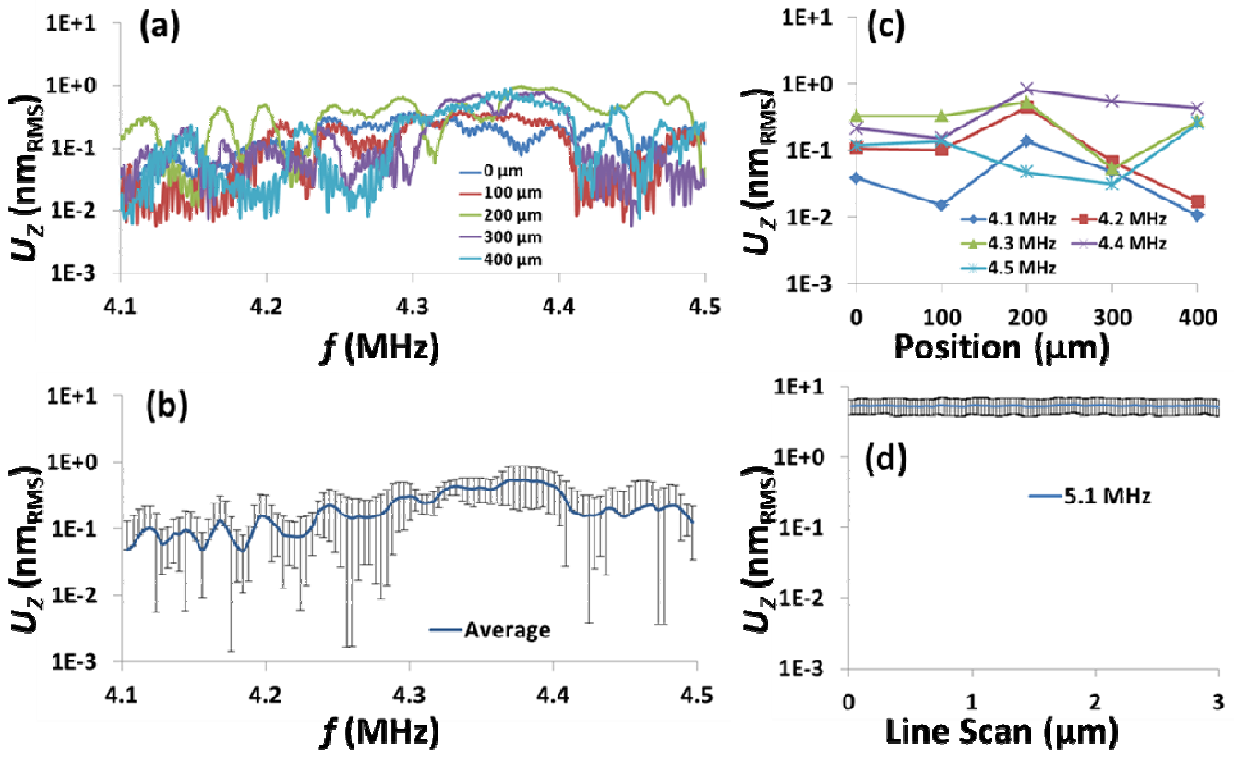

Figure 38: Positional dependence of U_z *vs.* f for a standard cantilever and SiO_2 sample across the 4 MHz transducer surface (a). Measurements were performed at 5 locations, where '0 µm' is positioned approximately in the center of the piezotransducer, and each subsequent measurement is performed 100 µm radially outward. The average of U_z *vs.* f for the 5 locations is presented with standard deviation error bars (b). The variability in U_z *vs.* position for 5 different frequencies is considered (c). The average and standard deviation of 256 line scans in a 3 µm x 3 µm UFM image of 30 nm Cr sample at 5.11 MHz are presented to demonstrate the consistency of U_z on a much shorter length scale (d).

7.5.3. Material Dependence

High frequency SPM measurements such as UFM can therefore be strongly influenced by actuator position, lever geometry, and frequency, confirming the importance of multidimensional approaches such as sUFM for optimizing measurement conditions especially to quantify and differentiate between areas of materials with distinct properties. In terms of nanomechanics, the UFM response as a function of contact force (F_0) directly relates to the local reduced modulus. Accordingly, this is tested with sUFM for three materials with dissimilar mechanical moduli – i) a Si substrate with a 300 nm thick thermally grown oxide, ii) the same SiO_2/Si substrate with an additional 500 nm thick layer of photoresist, and iii) the same SiO_2/Si substrate but with a 30 nm

thick magnetron sputtered Cr layer. Figure 39 displays the UFM response U_z (y axes) for all 3 materials (distinct curves) with respect to the normal force F_0 (x axes) and ultrasonic amplitude a_u (generated with 2, 4, and 6 V_{PP} drive voltage applied to the sample piezoactuator). In every case, increasing F_0 causes the ultrasonic response to decrease as expected [10]. This is because an increase of the normal load F_0 increases the average indention of the tip into the sample, correspondingly diminishing the non-linear tip-sample interactions during each ultrasonic period that dictate the magnitude of the UFM response.

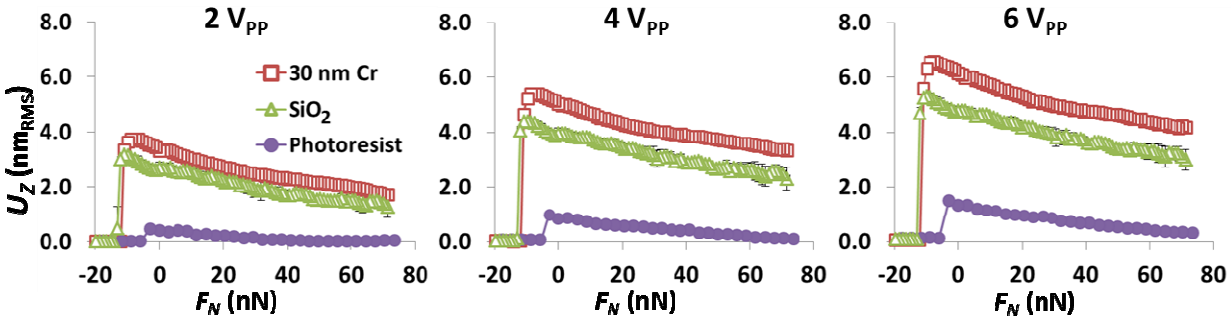

Figure 39: Material dependence of U_z *vs.* F_0 and a_u for a standard cantilever and 4 MHz transducer. The three materials considered are 30 nm Cr, photoresist, and SiO_2, described in detail in the methods section. Each data point is an average of three separate measurements totalling 1.5 seconds (3 x 50 samples with 10 ms time constant), and standard deviation error bars.

The UFM signal should equivalently diminish for compliant specimens. Accordingly, the ultrasonic response U_z is found to be strongest for Cr, followed by SiO_2, and then the photoresist, for any given ultrasonic excitation amplitude. This is consistent with the ranking of Young's moduli (E_{Cr}~140 GPa [34], E_{SiO2}~70 Gpa [35], $E_{photoresist}$~4 Gpa [36]), as well as the calculated reduced Young's moduli in contact with the tip (E^*_{Cr}~79 GPa, E^*_{SiO2}~50 GPa, $E^*_{photoresist}$~5 GPa, assuming Si tip). In fact, the UFM signal should be even stronger for bulk Cr, but is consistent with the sputtered Cr with non-perfect sputtered layer structure studied here.

A simple quantitative measure linked to the relative local stiffness can be obtained from such sUFM data by averaging the UFM response of Figure 39 over the representative force interval, e.g. from 0 to F_{max} = 40 nN. Although it is possible to consider a higher upper limit of the force interval (F_{max} > 40 nN), this value is chosen as it is within the reasonable operating range of the cantilever, and no plastic deformation of the samples are expected. Table 4 presents these results based on the averaged $\langle U_z \rangle = \frac{1}{F_{max}} \int_0^{F_{max}} U_z dF_0$ of the curves in Figure 39. Although this is just a relative measure of local stiffness, that would need further interpretation based on contact mechanics as reported elsewhere [10], the low standard deviation on the order of 5% for diverse measured materials indicates that sUFM potentially allows the effective investigation of mechanical properties for a wide variety of materials, especially uniquely differentiating those with high mechanical stiffness.

Table 4: U_z UFM response for 30 nm Cr, SiO_2, and photoresist materials obtained with 3 ultrasonic drive amplitudes (2 V_{PP}, 4 V_{PP}, 6 V_{PP}). Values are calculated from the U_z *vs*. F_0 curves in Figure 39, between 0 and 40 nN.

	Reduced Young's modulus E^*(GPa)	<U_z> (nm)		
		a_u = 2 V_{PP}	a_u = 4 V_{PP}	a_u = 6 V_{PP}
Cr (30 nm)	79	2.8 ± 0.1	4.4 ± 0.1	5.4 ± 0.1
SiO_2	50	2.2 ± 0.2	3.5 ± 0.2	4.3 ± 0.2
Photoresist	5	0.22 ± 0.05	0.62 ± 0.05	1.00 ± 0.05

One additional observation is also possible with such UFM results. The force at which the ultrasonic response abruptly falls to 0 indicates the pull-off force, and hence is sensitive to adhesion. In this case, the photoresist consistently broke contact with the tip at a reduced pull-off force, indicating diminished adhesion between the tip and the polymer film as compared to the

Cr or bare SiO_2 specimens. Such measurements have been demonstrated previously for distinct cases, but the sUFM approach efficiently enables optimal measurement and mapping of such properties as local adhesion and stiffness.

7.5.4. Multidimensional Spectroscopic UFM and Friction Effects

Finally, sUFM is applied to a 30 nm Cr film, specifically to compare results like in Figure 39 with simultaneous detection of friction which is known to be minimized during optimal UFM operation due to ultrasonic induced lubricity [25]. Instead of using 2D plots as before, however, this is best presented as 3D maps of the UFM response. Figure 40(a) displays the UFM signal (U_z) as color contrast for a wide range of excitation Force (F_0) and frequency (f) coordinates, as well as 3 discrete drive amplitudes (a_u) as before. The frequency of the strongest UFM response (clearly observed as a bright strip at ~4.3 MHz) has practically no dependence on either applied force or excitation amplitude. This is fully expected in the optimal experimental UFM regime, when cantilever vibrations are not excited and thus the lever acts as an effectively infinitely stiff beam [7]. A separate, less consistent peak (around 4.9 MHz) shows much more extensive substructure that varies with the experimental condition, suggesting convolution between piezotransducer and lever resonances.

For Figure 40(a), the expected trends are apparent in the ultrasonic response as a function of normal force and ultrasonic amplitude, in agreement with Figure 37 and Figure 39. Unlike the previous data, however, these results are acquired during scanning, allowing additionally the friction loop response - a representative measure of friction [25,37] - to be simultaneously recorded and mapped for the same multidimensional parameters (Figure 40(b)). The lowest friction (brightest areas in Figure 40(b)) clearly corresponds to ultrasonic frequencies with the strongest (brightest) UFM signal. Moreover, the friction signal appears to be more sensitive at

lower ultrasonic amplitudes. Therefore, while sUFM has been proven to be effective for optimizing UFM experimental parameters, monitoring the friction can also (or additionally) aid users of high frequency AFM techniques.

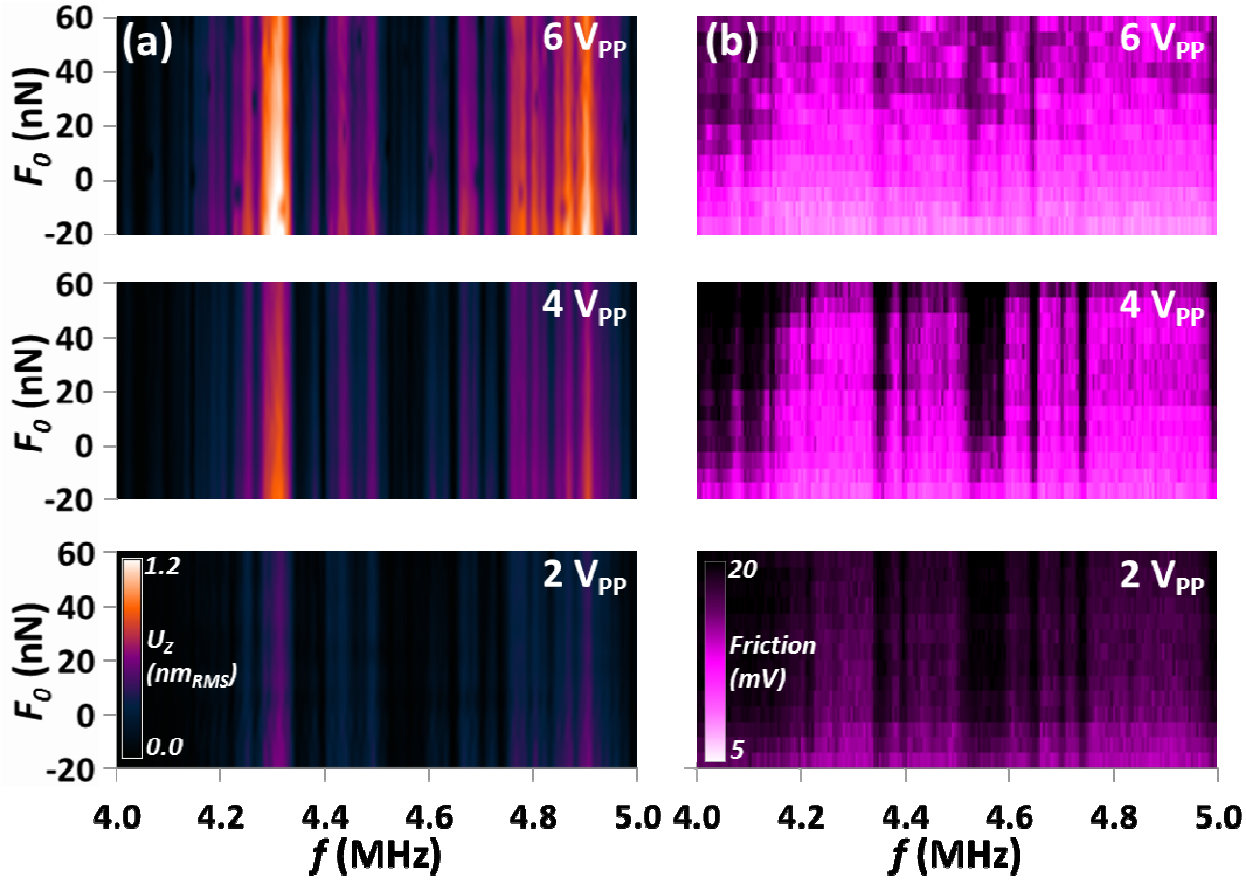

Figure 40: Three dimensional ultrasonic response, $U_z(a_u, f, F_0)$, acquired by the sUFM technique on a 30 nm Cr film (left column), and simultaneously acquired friction force response (right column). Each panel is schematically represented by the ultrasonic response in Figure 35 a_1, a_2, and a_3, respectively. The ultrasonic response is acquired over 500 ms (50 samples at 10 ms), and each friction response is acquired over 1000 ms (an average of four 500 nm line scans at 4 Hz line rate).

7.6. Conclusion

In conclusion, the multidimensional sUFM approach allows one to develop a comprehensive understanding of the physical mechanisms for high frequency scanning probe measurements using nonlinear detection such as UFM, HFM and related approaches. In particular, by determining the strongest, most consistent, and most uniform UFM response, preferred AFM

probes and ultrasonic piezotransducers should be low fundamental resonance frequency (hence long) cantilevers combined with higher resonance frequency piezoactuators (*e.g.* 4 MHz or above). Transducer resonance and position are also demonstrated to be important considerations when comparing high frequency SPM results from separate measurements. Investigations should be confined to areas smaller than $1/10^{th}$ of the ultrasonic wavelength, typically less than 10 x 10 μm^2 for a 4 MHz frequency actuator, otherwise local ultrasonic amplitude calibration or co-located standards may be required. The ultrasonic response for 30 nm Cr, SiO_2, and photoresist captured as a function of normal force, ultrasonic amplitude, and frequency demonstrated sUFM's ability to differentiate mechanical properties of both soft and stiff materials. Ultimately, this provides clear steps for the optimization of quantitative analysis and nanoscale mapping of mechanical properties in SPM, particularly valuable for otherwise hard to study high stiffness materials.

7.7. References

1. G. Binnig, C. F. Quate, and C. Gerber, Physical Review Letters **56** (9), 930 (1986).
2. B. D. Huey, in *Annual Review of Materials Research* (2007), Vol. 37, pp. 351.
3. S. Eslami and N. Jalili, Ultramicroscopy **117**, 31 (2012).
4. D. Lee, H. Lee, N. S. Lee, K. B. Kim, and Y. Seo, Curr. Appl. Phys. **12** (3), 989 (2012).
5. L. M. Picco, L. Bozec, A. Ulcinas, D. J. Engledew, M. Antognozzi, M. A. Horton, and M. J. Miles, Nanotechnology **18** (4) (2007).
6. T. E. Schaffer, M. Viani, D. A. Walters, B. Drake, E. K. Runge, J. P. Cleveland, M. A. Wendman, and P. K. Hansma, *An atomic force microscope for small cantilevers*. (Spie - Int Soc Optical Engineering, Bellingham, 1997), pp.48.
7. O.V. Kolosov and K. Yamanaka, Jpn J Appl Phys 2 **32** (8A), L1095 (1993).
8. E. J. Grier, O. Kolosov, A. K. Petford-Long, R. C. C. Ward, M. R. Wells, and B. Hjorvarsson, Journal of Physics D-Applied Physics **33** (8), 894 (2000).
9. Kazushi Yamanaka, Hisato Ogiso, and Oleg Kolosov, Applied Physics Letters **64** (2), 178 (1994).
10. F. Dinelli, S. K. Biswas, G. A. D. Briggs, and O. V. Kolosov, Physical Review B **61** (20), 13995 (2000).
11. Osamu Matsuda, Takuya Terada, Katsuhiko Inagaki, and Oliver B. Wright, Japanese Journal of Applied Physics **41** (Part 1, No. 5B), 3545 (2002).
12. A. P. McGuigan, B. D. Huey, G. A. D. Briggs, O. V. Kolosov, Y. Tsukahara, and M. Yanaka, Applied Physics Letters **80** (7), 1180 (2002).

13. Robert Szoszkiewicz, Andrzej J. Kulik, Gerard Gremaud, and Malgorzata Lekka, Applied Physics Letters **86** (12), 123901 (2005).
14. M. T. Cuberes, G. A. D. Briggs, and O. Kolosov, Nanotechnology **12** (1), 53 (2001).
15. U. Rabe and W. Arnold, Applied Physics Letters **64** (12), 1493 (1994).
16. K. Yamanaka and S. Nakano, Japanese Journal of Applied Physics Part 1-Regular Papers Short Notes & Review Papers **35** (6B), 3787 (1996).
17. U. Rabe, S. Amelio, E. Kester, V. Scherer, S. Hirsekorn, and W. Arnold, Ultrasonics **38** (1–8), 430 (2000).
18. F. Marinello, P. Schiavuta, S. Vezzù, A. Patelli, S. Carmignato, and E. Savio, Wear **271** (3-4), 534 (2011).
19. A. Striegler, B. Koehler, B. Bendjus, M. Roellig, M. Kopycinska-Mueller, and N. Meyendorf, Ultramicroscopy **111** (8), 1405 (2011).
20. M. T. Cuberes, H. E. Assender, G. A. D. Briggs, and O. V. Kolosov, Journal of Physics D-Applied Physics **33** (19), 2347 (2000).
21. M. Teresa Cuberes, Journal of Nanomaterials **2009**, 1 (2009).
22. G. J. Verbiest, J. N. Simon, T. H. Oosterkamp, and M. J. Rost, Nanotechnology **23** (49) (2012).
23. G. S. Shekhawat and V. P. Dravid, Science **310** (5745), 89 (2005).
24. L. Tetard, A. Passian, K. T. Venmar, R. M. Lynch, B. H. Voy, G. Shekhawat, V. P. Dravid, and T. Thundat, Nat Nanotechnol **3** (8), 501 (2008).
25. F. Dinelli, S. K. Biswas, G. A. D. Briggs, and O. V. Kolosov, Applied Physics Letters **71** (9), 1177 (1997).
26. I. Grishin, B. D. Huey, and O. V. Kolosov, Acs Appl Mater Inter **5** (21), 11441 (2013).
27. E. Teidelt, J. Starcevic, and V. L. Popov, Tribol Lett **48** (1), 51 (2012).
28. S. Hirsekorn, U. Rabe, and W. Arnold, Nanotechnology **8** (2), 57 (1997).
29. J. E. Sader, J. W. M. Chon, and P. Mulvaney, Review of Scientific Instruments **70** (10), 3967 (1999).
30. H. Ogiso K. Yamanaka, O. Kolosov, Applied Physics Letters **64** (2), 178 (1994).
31. M. T. Cuberes, J. Nanomater., 5 (2009).
32. L. Tetard, A. Passian, K. T. Venmar, R. M. Lynch, B. H. Voy, G. Shekhawat, V. P. Dravid, and T. Thundat, Nature Nanotechnology **3** (8), 501 (2008).
33. R. Mitra, Appl. Acoust. **48** (1), 1 (1996).
34. G. B. Beneventi, L. Guarino, M. Ferro, and P. Fantini, J Appl Phys **113** (4) (2013).
35. E. Bassous, Ieee T Electron Dev **25** (10), 1178 (1978).
36. Jiali Gao, Le Guan, and Jinkui Chu, 2010 (unpublished).
37. R. W. Carpick and M. Salmeron, Chem. Rev. **97** (4), 1163 (1997).

Chapter 8: Nanomechanical Morphology of Amorphous, Transition, and Crystalline Domains in Phase Change Memory Thin Films

8.1. Abstract

In the search for phase change materials (PCM) that may rival traditional random access memory, a complete understanding of the amorphous to crystalline phase transition is required. For the well-known $Ge_2Sb_2Te_5$ (GST) and GeTe (GT) chalcogenides, which display nucleation and growth dominated crystallization kinetics, respectively, this work explores the nanomechanical morphology of amorphous and crystalline phases in 50 nm thin films. Subjecting these PCM specimens to a lateral thermal gradient spanning the crystallization temperature allows for a detailed morphological investigation. Surface and depth-dependent analyses of the resulting amorphous, transition and crystalline regions are achieved with shallow angle cross-sections, uniquely implemented with beam exit Ar ion polishing. To resolve the distinct phases, ultrasonic force microscopy (UFM) with simultaneous topography is implemented revealing a relative stiffness contrast between the amorphous and crystalline phases of 14% for the free film surface and 20% for the cross-sectioned surface. Nucleation is observed to occur preferentially at the PCM-substrate and free film interface for both GST and GT, while fine subsurface structures are found to be sputtering direction dependent. Combining surface and cross-section nanomechanical mapping in this manner allows 3D analysis of microstructure and defects with nanoscale lateral and depth resolution, applicable to a wide range of materials characterization studies where the detection of subtle variations in elastic modulus or stiffness are required.

8.2. Foreword

With optimized ultrasonic force microscopy experimental parameters (Chapter 7:), the sUFM method was combined with beam exit Ar ion polishing (BEXP) to investigate the free surface and shallow angle cross-sections of PCM films displaying both nucleation and growth dominated crystallization mechanisms. The following chapter presents the nanomechanical morphology of films subjected to a macroscopic thermal gradient, with subtle heterogeneities and defects distinguished, previously only made possible by tedious, destructive characterization methods, i.e. transmission electron microscopy.

8.3. Introduction

Significant efforts continue to try to improve non-volatile memory systems, ideally with improved read/write cycle endurance, faster switching speeds, and lower power consumption. One such class of materials are the ternary chalcogenides, which exhibit rapid and reversible phase transitions between the amorphous and crystalline states [1,2]. It is well known that this class of phase change materials (PCM) [3] still needs to be improved in several key areas to become competitive with current technologies, with the major target being finding a stoichiometry that exhibits a fast crystallization speed [4] while maintaining mechanical and morphological stability upon high cycling of the read and write process [5]. In parallel with experimental [6-11] and theoretical studies [12-14], nanoscale characterization methods such as scanning probe microscopy (SPM) [8,15-18] and transmission electron microscopy (TEM) [10,12,19,20] have been widely implemented to study the phase switching dynamics and mechanical properties of the chalcogenide materials.

One particularly useful tool for studying the nanomechanical morphology of the switched phases and their corresponding stresses due to density changes combines nanomechanical mapping by

ultrasonic force microscopy (UFM) with beam exit Ar ion beam polishing (BEXP) [21] for low-damage, shallow angle cross sectioning. Accordingly, we report the 3-dimensional nanomechanical morphology of amorphous and crystalline phases for two commercially viable phase change stoichiometries, $Ge_2Sb_2Te_5$ (GST) and GeTe (GT), each with thermally and optically induced crystallization. This work is particularly relevant for characterizing defects through the film thickness for ultimately improving device design and dimensional scaling of these phase change technologies.

8.4. Methods

8.4.1. Sample Fabrication

Amorphous GeTe and $Ge_2Sb_2Te_5$ films were sputtered (Moorfield MiniLab 25) onto Si wafers (3" diameter, 280 μm thick, p-doped, <100>, 0.01 – 1.0 Ω-cm), with an intermediate 100 nm of sputtered Ti to promote adequate bonding. The sputtering conditions in all cases include a deposition rate of 0.3 – 0.4 Å/s at a base pressure of 10^{-5} Torr, with an RF power of 6-8 W for both chalcogenide layers and 40 W for the Ti matching layer.

8.4.2. Sample Processing

Following sample fabrication, each wafer was cut into 25 x 75 mm strips for the application of a thermal gradient, thereby nucleating the crystalline phase in the amorphous film with a distinct transition region (containing both amorphous and crystalline phases) in between. One side of each strip was attached to an electric heater capable of controlled heating to 600 ^{0}C (Linkam Scientific Instruments, UK), while the other side was mounted 20 mm away to a carbon steel heat sink (20 mm diameter, 3.2 mm thickness), Figure 41(a).

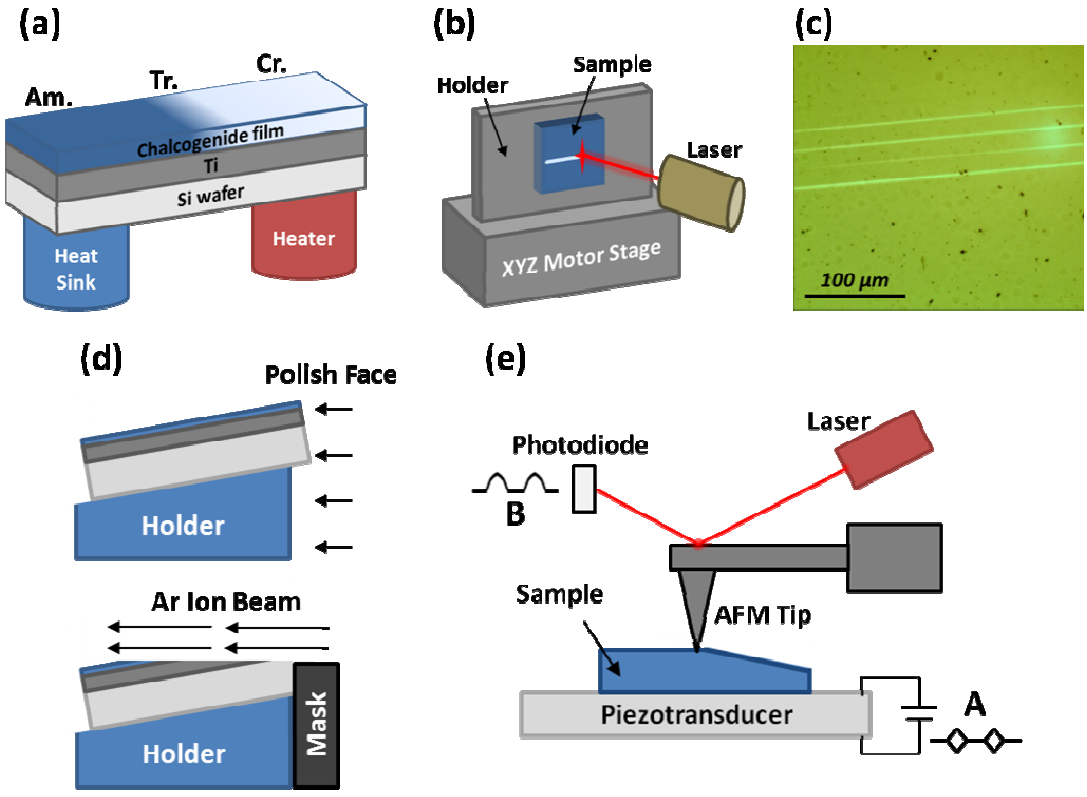

Figure 41: As deposited predominantly amorphous phase change material samples were mounted onto a heater and heat sink via thermally conductive paste creating a fully crystalline phase at the heater side, unaffected amorphous area and a transition region (a). All samples with distinct regions (amorphous, transition, crystalline) were mounted onto an XYZ motor stage and locally heated with a CW laser providing a narrow line of fully switched crystalline zone (b), with phase switching then confirmed by optical microscope (c). The samples were then cross-sectioned using BEXP method [21] (d) for nanomechanical characterization by UFM [22] (e).

Adequate thermal contact between both the sample/heater and sample/heat sink surfaces was made by Boron Nitride conductive heat sink grease (CircuitWorks CW7250). The temperature of the heater was increased by 10°C/s from room temperature to 300°C and held for 2 minutes, until complete crystallization occurred for the phase change material directly above the heater surface. The heat sink was present to maintain the amorphous region in one end of the film (although its temperature was not monitored, no notable heating occurred due to the large mass of the heat sink and small size of the PCM sample). The transition regions between amorphous and

crystalline states for GT and GST films were 350-450 µm and 900-950 µm wide, respectively, as confirmed by optical microscopy.

Following the thermal gradient treatment, each strip of GT and GST was cleaved into three 6 x 6 mm samples, separating the amorphous, crystalline, and transition regions. Each sample was mounted onto a motorized XYZ stage and a focused CW laser of 30-40 mW on-the-sample power (514 nm Ar ion laser, Spectra Physics, USA) was used to write an optically-induced crystalline 'reference' line (2-5 µm wide, 2-3 mm long) across all three phase regions, Figure 41(b). The samples were programmatically translated with a step motor controller (Honda Electronics, Japan) at 50 µm per second to provide a consistent Joule heating per unit area as described elsewhere [11]. Further characterization under the optical microscope confirmed contrast between the crystalline reference line and the amorphous/transition regions for GT and GST, but no observable contrast in the already-crystalline region as expected. This both confirms the complete transition of the thermally switched area, as well as the absence of possible artefacts from laser heating alone. Figure 41(c) typifies 4 parallel crystalline phase lines written in the amorphous GST film as observed in the optical microscope.

Cross-sectioning of all three phase regions for each PCM stoichiometry was next performed by the BEXP method, Figure 41(d), using an in-house modified cross-section polisher (Leica EM TIC020, Germany) [23]. To achieve a final polished angle of 10° from the surface normal, the side surface of each sample was mechanically lapped with a 80° angle to ensure adequate contact with the mask. The ion polisher cutting voltage was set to 7 kV, until the cross-section was completed. The cutting voltage was then lowered to 1 kV for 15-30 minutes to finely polish the cross-section and prevent sample erosion due to transmission sputtering [24].

8.4.3. Sample Characterization

In order to quantify the nanoscale morphology and relative stiffness of the chalcogenide phases, scanning probe based methods were implemented. Specifically, UFM was chosen due to its ability to distinguish subtle differences in local elasticity (<0.1%) [25] for even the most stiff materials, and with the same or better lateral resolution as conventional contact mode AFM [26-28]. Figure 41(e) displays the schematic for these UFM measurements, allowing investigation of both the free surface and the shallow-angle cross sections in a single image. All UFM measurements were performed on both a Multimode SPM system with Nanoscope IV controller (Bruker, USA) and a Cypher AFM (Asylum Research, USA) system, each operated in an ambient environment. To maximize the propagation of the longitudinal ultrasonic waves key to the UFM technique, all samples were mounted onto a piezotransducer with crystalline salol (phenyl salicylate, melting point 42°C). Ultrasonic vibrations were excited at the resonant frequency of the 4 MHz piezotransducer (Physik Instrumente, Germany) with an amplitude modulated sine wave defined by a triangular-shaped waveform produced by an arbitrary function generator (Agilent 33220A, USA), signal A in Figure 41(e). The frequency of the arbitrary waveform was chosen (2.71 kHz) as an optimal trade-off, avoiding vertical feedback loop influences and cantilever resonances, while allowing for sufficiently fast data acquisition. In response to these periodic ultrasonic vibrations, correlated periodic normal displacement of the AFM tip occurs detected by the AFM's position sensitive quadrant photodiode (signal B in Figure 41(e)). This normal deflection signal was analysed by a lock-in amplifier (LIA) (Stanford Research Systems 830), with the reference signal at the modulation frequency provided by the external waveform generator. The UFM amplitude U_z at the first harmonic of the modulation frequency was finally extracted, with a filter time constant of 1 to 3 ms for proper averaging up

to the duration of each image pixel given line scan rates usually of 0.5 to 1.0 Hz. Typical LIA sensitivities were 10 to 20 mV full scale, appropriate for ultrasonic carrier sine wave amplitudes in the range of 2 to 5 V_{PP}. The UFM amplitude was finally routed to the AFM auxiliary inputs, allowing simultaneous topography and nanomechanical UFM acquisition.

8.4.4. Image Analysis

A standard fast Fourier transform (FFT) band pass filter was applied to each UFM image to remove periodic noise, with the lower limit of the filter set to 50% of the grain size, approximately 30 nm for all regions of GST and 15 nm for GT, respectively.

8.5. Results and Discussion

8.5.1. Plan View Specimens

Prior to performing a complete nanomechanical characterization (cross-sectioning and imaging), the nature of each amorphous, transition, or crystalline phase region was verified by two methods. First, the CW laser was used to write a well-defined crystalline-phase-only reference line (see Methods). As these PCM materials display a high reflectivity contrast between amorphous and crystalline phases, allowing their easy identification [29], the films were then inspected with optical microscopy. The films were then independently characterized by UFM, allowing the observation of features much finer than wavelength-limited optical techniques. The crystalline line present in all samples studied also serves as a consistent reference for UFM measurements up to 10-20 μm on either side. This alleviates the need for independent calibration of the absolute ultrasonic amplitude (and hence UFM contrast) that is otherwise necessary, since it can vary on the scale of many hundreds of μm [30] due to the underlying transducer, resonant effects, or spatially dependent ultrasonic transmission. Since the μm scale UFM images

presented here are orders of magnitude smaller than the ultrasonic wavelength, and include an identical crystalline region in each case, they may thus be compared with confidence [31].

Figure 42 presents representative topography (left) and UFM (right) images for the amorphous and transition phase regions for the GST and GT films. Images for the crystalline reference line through the crystalline phase region for GST and GT were also acquired, but are not presented as they display no topography or ultrasonic contrast as expected. The location of the crystalline reference line (dashed lines on topography) is apparent in the topography images by a depression in the thin film, as a result of the lower specific volume for the crystalline phase [32]. The UFM images of the crystalline line through the amorphous region (top row) displays a stronger (brighter) UFM response for the crystalline versus amorphous phase, indicating a higher relative stiffness [33]. This behavior is expected based on previous mechanical studies by nanoindentation [34,35], wafer curvature [36], and resonating beam methods [37].

The topography and UFM images of the crystalline lines through the transition regions (bottom row) also reveal an increased density and stiffness, respectively, but with less contrast presumably due to the partial phase change that has already occurred. The laser line passing through the transition region in GST displays particularly interesting topographic and nanomechanical morphology. The center of the laser line has a lower topography with corresponding high contrast, indicative of crystalline material. Approximately 1-2 μm to either side of the laser line center, however, both the topography and ultrasonic response suggest a higher amorphous fraction. This behaviour may reflect a complex strain distribution in such nanometre scale thick films, especially where the laser induced crystallization is performed in an area already possessing crystalline nuclei as expected for the thermally induced transition region.

Another possibility is the film may partially delaminate from the substrate so that a lower ultrasonic response would be locally observed [38].

For the thermally induced transition region, but away from the crystalline reference lines (i.e. not optically switched), a profound difference in crystallization morphology is apparent for the GST versus GT. For the GST film the microstructure is too fine to be properly resolved in these ~8 µm images, but is clearly less than 100 nm. For GT, on the other hand, there are clear, circular shaped, 2- 5 µm diameter crystalline regions.

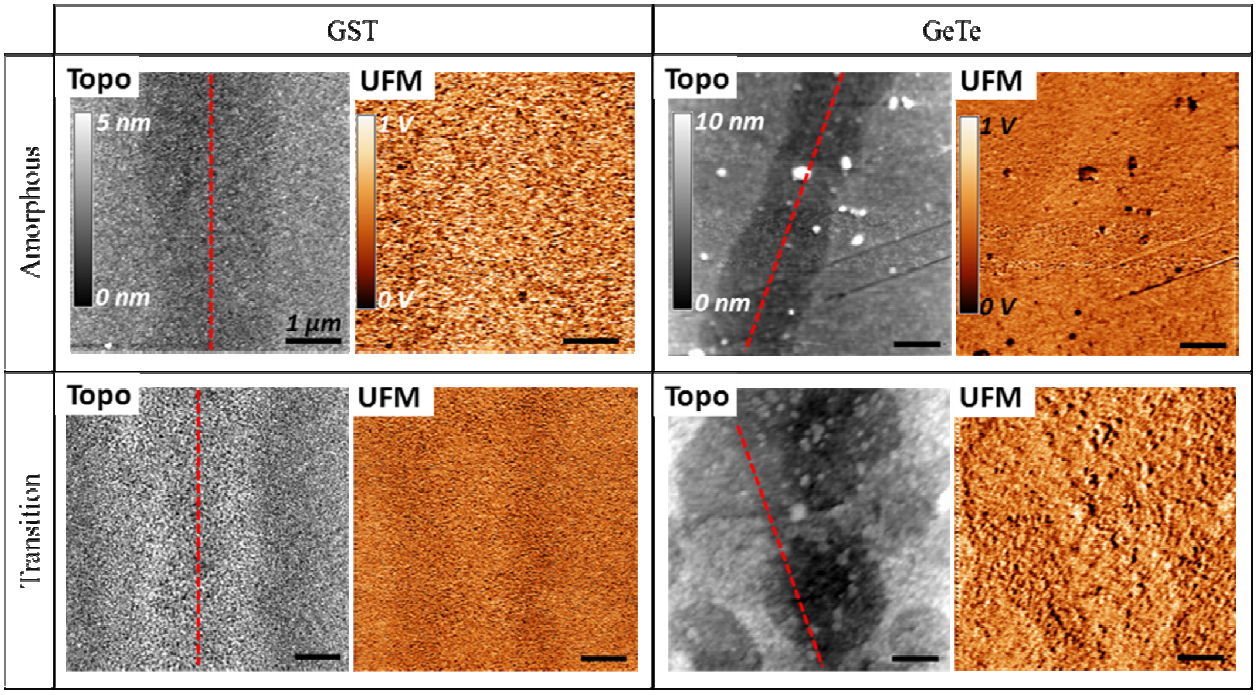

Figure 42: Topography (1st and 3rd columns) and UFM images (2nd and 4th columns) of amorphous (top row) and transition (bottom row) regions of GST (left) and GT (right) films with a crystalline reference line written by laser pulses according to Figure 41(b). The centreline of the laser path is identified in each topography image (dashed overlay), with uniform 1 µm scale bars shown throughout.

To explore details of the nanomechanical morphology of individual grains, higher magnification (1 µm) images were acquired away from but still sufficiently close to the crystalline reference line for reliable UFM measurements, Figure 43. For both the amorphous and crystalline phase regions of the GST film, the grains were ellipsoidal with height and width of ~55 and ~70 nm,

respectively, in close agreement with the ~70 nm grain size reported for similarly sputtered GST films [39]. One notable feature in the UFM images for the GST crystalline phase is the appearance of dark, less stiff rings surrounding some grains (see 3x magnification insets). These may be amorphous residues that fail to crystallize at the grain boundaries, with a characteristic size of ~6 nm as reported elsewhere [40,41]. There are occasional similar features present within the amorphous region as well, which could result from the amorphous region of GST containing a small fraction of crystalline phase grains, likely due to localized temperature elevations during the initial sputtering process.

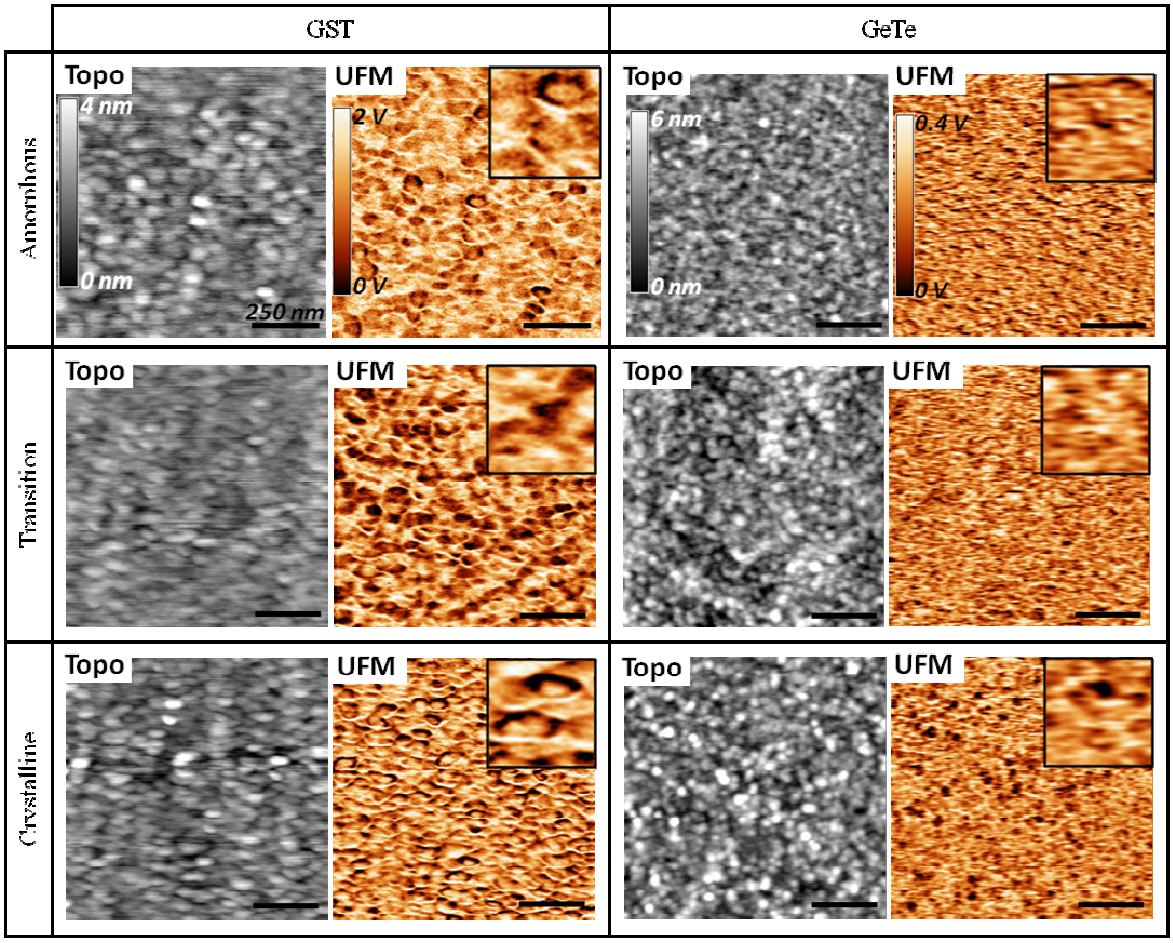

Figure 43: 1 µm topography (left) and UFM images (right) of amorphous (top row), transition (center row), and crystalline (bottom row) regions of GST and GT films. Insets are provided within each UFM image (3x magnification), clearly resolving the nanomechanical morphology.

The transition region for GST (middle row in Figure 43) has much higher nanomechanical non-uniformity than the amorphous or crystalline regions, revealing interspersed amorphous/crystalline phases with varied stiffness. The characteristic length scale of the nucleated crystalline phase within the transition region is approximately 100 – 200 nm, similar to crystallization behavior reported by Yang et al. [15]

To more accurately compare the relative stiffness of all three phase regions, which are necessarily obtained over different regions of the underlying piezotransducer, the RMS variation of the UFM signal was normalised to the average response over the entire imaged area as described elsewhere [30]. For GST, the UFM stiffness contrast in the thermally induced amorphous and crystalline regions varied by 7% and 11%, respectively. For the transition region, it varied significantly more strongly at 14%. On the other hand, the amorphous, crystalline, and transition regions uniformly displayed a relatively weak ultrasonic response variation of 3%, 4%, and 2%, respectively, possibly reflecting the difference between the nucleation dominated kinetics of GST vs. growth dominated kinetics of GT.

8.5.2. Shallow Angle Cross Sections

Following these unique measurements of the surface nanomechanics of variously switched films, BEXP prepared shallow-angle cross-sections for each phase region of GST (top row) and GT (bottom row) were also studied with UFM (Figure 44). Every image has been rotated for clarity, such that the top portion of each image displays the intact surface of the phase change material (akin to the results of Figures Figure 42 and Figure 43, exemplified by the region labelled ‘A’ in Figure 44). The next layer from the top is the 50 nm cross-sectioned phase change material, followed by 100 nm of cross-sectioned Ti, and the underlying cross-sectioned Si substrate.

Importantly, the ion-cross-sectioned portions of the presented images (i.e. beyond region A) are at an oblique orientation topographically, as identified in Figure 41(e,f). Therefore, the stated thickness of each layer is not directly apparent. Moreover, due to variations in the speed at which the Ar ions penetrate the film as well as the local sputtering yield [21], the sectioned angle differs slightly from one layer to another. Conveniently, the simultaneously acquired topography line profiles (Figure 45) can identify these angles, ranging from 17 to 40 degrees, and can be used to calibrate the actual layer thicknesses in the oblique view.

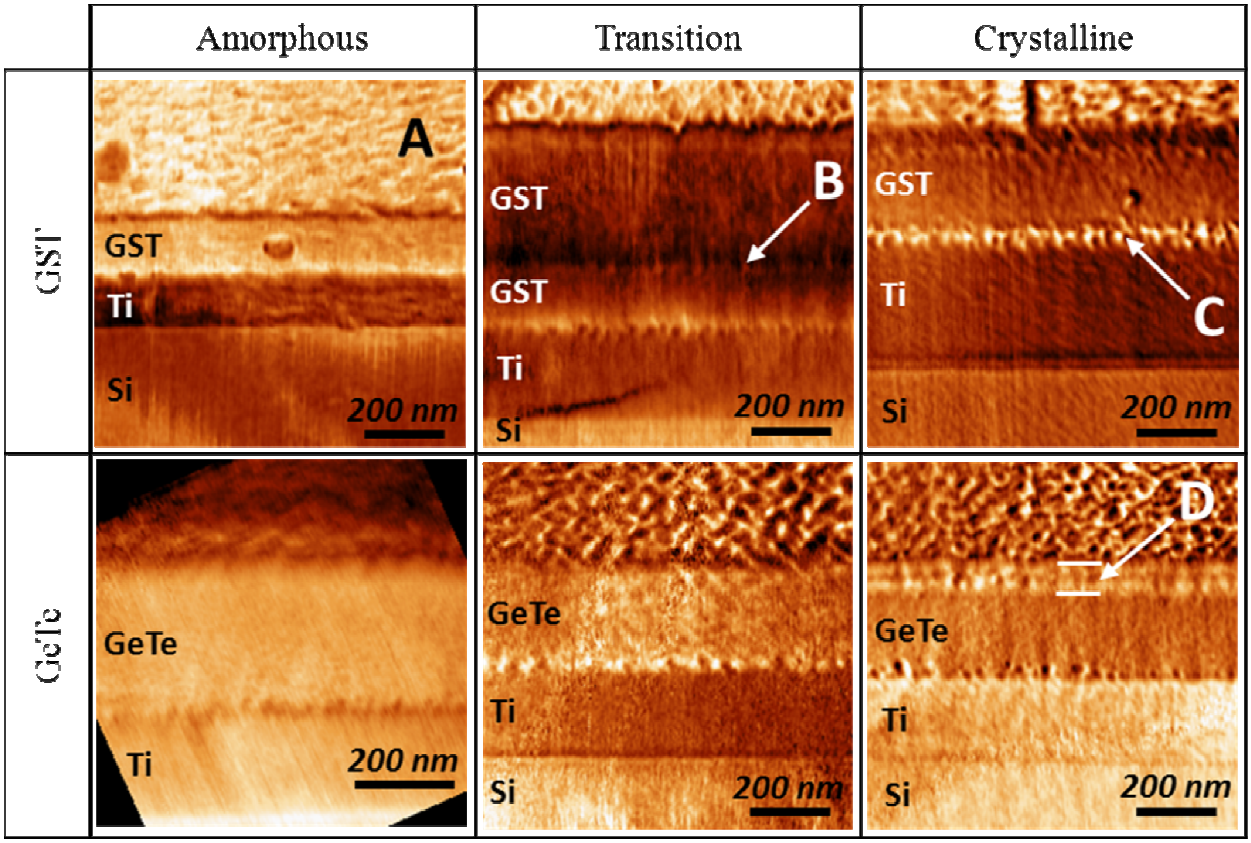

Figure 44: UFM Images of GST and GT films with BEXP cross-sectioning performed according to Figure 41(d). Note: images are presented at an oblique orientation, therefore the thickness of phase change material (50 nm) and Ti underlayer (100 nm) are not directly apparent without topography line profiles (Figure 45).

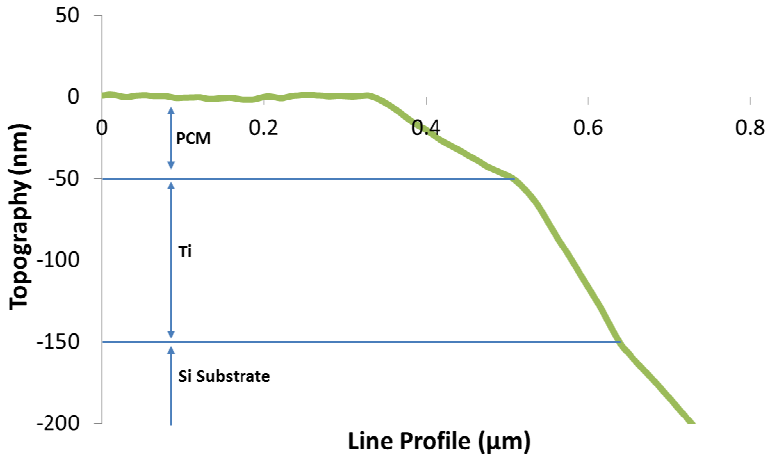

Figure 45: Example topography line-scan profile for the cross-sectioned phase change material, taken from the GST amorphous region, line 66 (out of 256) from the top. The angles between the free-film and cross-sectioned surfaces are 17°, 40°, and 29° for PCM, Ti, and the Si substrate, respectively.

First considering the topography of the sections, rms-roughness values for the amorphous, transition, and crystalline regions of GST are 0.6 nm, 1.4 nm, and 1.4 nm, respectively. For GT, the amorphous, transition, and crystalline regions are 1.1 nm, 0.5 nm, and 1.0 nm, respectively. The corresponding normalized rms calculations of the UFM signal variability, as discussed for Figure 43, is summarized in Table 5, revealing differences between the UFM response for the top (normal to the substrate) and cross-sectioned surfaces. This is likely due to the slight topographic variations from one region to the other, which could otherwise strongly influence contact-nanomechanical results due to changes in contact area [42]. This highlights a benefit of cross-sectioning with the BEXP technique, as it can reduce such topographic influences on nanomechanical contrast by generating surfaces with roughness on the order of just 1 nm as occurred here [23].

With respect to the UFM contrast, there are several noteworthy observations. First, the GST film in the transition region contains a discontinuity (labelled ‘B’ in Figure 44) which displays a lower ultrasonic response. We believe this corresponds to the sputtering process, which was interrupted part way through deposition of the GST layer, highlighting the sensitivity of the

current approach. Additionally, the ultrasonic response at this interface is weaker than the surroundings, indicating a decrease in the local stiffness. Second, the ultrasonic response at the junction between the phase change layers and the Ti (labelled 'C' in Figure 44) displays a stronger UFM contrast for the crystalline and transition regions, but not for the amorphous regions. Such higher signals at the PCM/Ti interface suggest locally stiffer materials as a result of a nucleated crystalline phase. However, a heterogeneity due to possible formation of a TiO_x layer cannot be excluded as a result of breaking the vacuum while switching the sputtering target material from Ti to GST/GT. In future, the sample processing may be improved by sputtering within a chamber capable of holding multiple source materials, to ensure that the vacuum is maintained. Third, at the interface between the top surface and cross-sectioned phase change material for the crystalline GST/GT and GST transition (exemplified by 'D' in Figure 44), a 5-10 nm layer with stronger nanomechanical contrast also is apparent. This most likely is a known artefact associated with the BEXP process near the original specimen surface, where if the Ar beam is allowed to continue after the cross-section is completed, transmission sputtering through the top surface will erode the surface material [23]. This may be addressed by lowering the Ar beam power from 5-7 kV down to 1 kV at the exact moment the beam finishes cutting, but this is difficult to implement without an automated cutting process. Nevertheless, the ability to characterize these artefacts with UFM demonstrates how powerful a tool nanomechanical mapping can be, with lateral resolution down to the AFM tip radius and depth resolution even further enhanced due to the oblique measurement angle.

Table 5: Nanoscale UFM variability of the three regions (amorphous, transition, crystalline) for each material, image size, and surface. 'UFM variability' refers to the root mean square of the ultrasonic response in volts normalised to the ultrasonic amplitude as in ref [43], providing a more accurate means for comparing the ultrasonic response of measurements taken from different areas. Note: all BEXP images were acquired with 1 µm image size, except for the GST amorphous region (800 nm).

Material	Region	Flat Surface	BEXP Surface
$Ge_2Sb_2Te_5$	Amorphous	6.94	9.99
$Ge_2Sb_2Te_5$	Transition	14.24	20.06
$Ge_2Sb_2Te_5$	Crystalline	11.36	13.40
GeTe	Amorphous	3.59	3.92
GeTe	Transition	1.90	18.30
GeTe	Crystalline	4.01	17.78

Taking into account these possible artefacts and processing features, several insights into the nanomechanical properties of the three distinct phase regions can be made for both chalcogenide compositions. The amorphous regions for both GST and GT display the most uniform ultrasonic response, with a variation of just 10% and 4%, respectively. The crystalline and transition regions for GST and GT, on the other hand, display a much stronger nanomechanical contrast. For GST this variation is 13% and 20% for crystalline and transition regions, respectively, as compared to 18% and 18% for GT. The fact that the nanomechanical contrast varies most for the transition regions as compared to the purely crystalline or amorphous confirms the coexistence of nanoscale amorphous and crystalline phases within the transition region.

8.6. Conclusion

The nanomechanical morphology of amorphous and crystalline phases in $Ge_2Sb_2Te_5$ and GeTe thin films have been investigated by ultrasonic force microscopy, both in plan-view as well as for shallow-angle-cross sections prepared by beam exit Ar ion polishing. The characteristic length scale of the crystalline phase within the amorphous films is on the order of 100 – 200 nm for $Ge_2Sb_2Te_5$, consistent with the previously reported nucleation dominated crystallization behavior. Contrast in the nanomechanical response due to stiffness variations between the

amorphous and crystalline phases are demonstrated up to 14% and 20% for the normal and cross-sectioned films, respectively. Several artifacts present in images of the cross-sectioned films were analyzed, with proposed suggestions for future sample fabrication and processing to improve similar measurements in the future. The advantages of utilizing ultrasonic force microscopy and beam exit Ar ion polishing are proven to be effective in characterizing materials with subtle variations in stiffness, relevant to the improvement of phase change films for data storage applications but also applicable to a much wider range of investigations into stiff materials with nanoscale heterogeneities.

8.7. References

1. N. Yamada, E. Ohno, N. Akahira, K. Nishiuchi, K. Nagata, and M. Takao, Jpn. J. Appl. Phys. Part 1 - Regul. Pap. Short Notes Rev. Pap. **26**, 61 (1987).
2. J. Akola and R. O. Jones, Physical Review B **76** (23) (2007).
3. Stanford R. Ovshinsky, Physical Review Letters **21** (20), 1450 (1968).
4. W. Welnic, A. Pamungkas, R. Detemple, C. Steimer, S. Blugel, and M. Wuttig, Nat. Mater. **5** (1), 56 (2006).
5. L. Goux, D. T. Castro, G. A. M. Hurkx, J. G. Lisoni, R. Delhougne, D. J. Gravesteijn, K. Attenborough, and D. J. Wouters, Ieee T Electron Dev **56** (2), 354 (2009).
6. T. Nonaka, G. Ohbayashi, Y. Toriumi, Y. Mori, and H. Hashimoto, Thin Solid Films **370** (1-2), 258 (2000).
7. S. Raoux, C. T. Rettner, J. L. Jordan-Sweet, A. J. Kellock, T. Topuria, P. M. Rice, and D. C. Miller, J. Appl. Phys. **102** (9) (2007).
8. J. Kim, M. H. Kwon, and K. B. Song, Ultramicroscopy **108** (10), 1246 (2008).
9. H. S. P. Wong, S. Raoux, S. Kim, J. L. Liang, J. P. Reifenberg, B. Rajendran, M. Asheghi, and K. E. Goodson, Proc. IEEE **98** (12), 2201 (2010).
10. Sung Jin Park, Moon Hyung Jang, Seung-Jong Park, Mann-Ho Cho, and Dae-Hong Ko, Applied Surface Science **258** (24), 9786 (2012).
11. I. Grishin, B. D. Huey, and O. V. Kolosov, Acs Appl Mater Inter **5** (21), 11441 (2013).
12. W. Welnic, J. A. Kalb, D. Wamwangi, C. Steimer, and M. Wuttig, Journal of Materials Research **22** (9), 2368 (2007).
13. S. Caravati, M. Bernasconi, T. D. Kuhne, M. Krack, and M. Parrinello, Physical Review Letters **102** (20) (2009).
14. Y. Fujisaki, Jpn. J. Appl. Phys. **52** (4) (2013).
15. F. Yang, L. Xu, R. Zhang, L. Geng, L. Tong, J. Xu, W. N. Su, Y. Yu, Z. Y. Ma, and K. J. Chen, Appl Surf Sci **258** (24), 9751 (2012).
16. J. Kim, Scanning **32** (5), 320 (2010).
17. T. Gotoh, K. Sugawara, and K. Tanaka, Jpn J Appl Phys 2 **43** (6B), L818 (2004).

18. B. D. Huey, R. N. Premnath, S. Lee, and N. A. Polomoff, J Am Ceram Soc **95** (4), 1147 (2012).
19. A. Gyanathan and Y. C. Yeo, J. Appl. Phys. **110** (12) (2011).
20. K. Do, D. Lee, D. H. Ko, H. Sohn, and M. H. Cho, Electrochemical and Solid State Letters **13** (8), H284 (2010).
21. O. V. Kolosov, I. Grishin, and R. Jones, IOP Nanotechnology **22** (2011).
22. A. P. McGuigan, B. D. Huey, G. A. D. Briggs, O. V. Kolosov, Y. Tsukahara, and M. Yanaka, Applied Physics Letters **80** (7), 1180 (2002).
23. O. V. Kolosov, I. Grishin, and R. Jones, Nanotechnology **22** (18) (2011).
24. Peter Sigmund, in *Sputtering by Particle Bombardment I*, edited by Rainer Behrisch (Springer Berlin Heidelberg, 1981), Vol. 47, pp. 9.
25. F. Dinelli, M. R. Castell, D. A. Ritchie, N. J. Mason, G. A. D. Briggs, and O. V. Kolosov, Philos Mag A **80** (10), 2299 (2000).
26. M. T. Cuberes, G. A. D. Briggs, and O. Kolosov, Nanotechnology **12** (1), 53 (2001).
27. K. Yamanaka and S. Nakano, Japanese Journal of Applied Physics Part 1-Regular Papers Short Notes & Review Papers **35** (6B), 3787 (1996).
28. K. Yamanaka, H. Ogiso, and O. Kolosov, Applied Physics Letters **64** (2), 178 (1994).
29. M. Libera and M. Chen, Journal of Applied Physics **73** (5), 2272 (1993).
30. J. L. Bosse, P. D. Tovee, B. D. Huey, and O. V. Kolosov, Journal of Applied Physics **115** (14) (2014).
31. R. Mitra, Appl. Acoust. **48** (1), 1 (1996).
32. W. K. Njoroge, H. W. Woltgens, and M. Wuttig, J. Vac. Sci. Technol. A-Vac. Surf. Films **20** (1), 230 (2002).
33. O. V. Kolosov, M. R. Castell, C. D. Marsh, G. A. D. Briggs, T. I. Kamins, and R. S. Williams, Physical Review Letters **81** (5), 1046 (1998).
34. Y. Choi and Y. K. Lee, Electron Mater Lett **6** (1), 23 (2010).
35. I. M. Park, J. K. Jung, S. O. Ryu, K. J. Choi, B. G. Yu, Y. B. Park, S. M. Han, and Y. C. Joo, Thin Solid Films **517** (2), 848 (2008).
36. J. Kalb, F. Spaepen, T. P. L. Pedersen, and M. Wuttig, J. Appl. Phys. **94** (8), 4908 (2003).
37. Y. Won, J. Lee, M. Asheghi, T. W. Kenny, and K. E. Goodson, Appl. Phys. Lett. **100** (16) (2012).
38. John W. Hutchinson, (Harvard University, Division of Engineering and Applied Sciences, 1996), pp. 4.
39. H. Seo, T. H. Jeong, J. W. Park, C. Yeon, S. J. Kim, and S. Y. Kim, Jpn. J. Appl. Phys. Part 1 - Regul. Pap. Short Notes Rev. Pap. **39** (2B), 745 (2000).
40. J. Lee, Z. J. Li, J. P. Reifenberg, S. Lee, R. Sinclair, M. Asheghi, and K. E. Goodson, J. Appl. Phys. **109** (8) (2011).
41. Z. J. Li, J. Lee, J. P. Reifenberg, M. Asheghi, R. G. D. Jeyasingh, H. S. P. Wong, and K. E. Goodson, Ieee Electr Device L **32** (7), 961 (2011).
42. F. Dinelli, H. E. Assender, N. Takeda, G. A. D. Briggs, and O. V. Kolosov, Surf. Interface Anal. **27** (5-6), 562 (1999).
43. J. L. Bosse, P. D. Tovee, B. D. Huey, and O. V. Kolosov, Journal of Applied Physics **115** (14), 144304 (2014).

Chapter 9: Nanoscale Characterization of Amorphous and Crystalline Phases in Chalcogenide Thin Films with Scanning Thermal Microscopy

9.1. Abstract

The thermal properties of amorphous and crystalline phases in chalcogenide phase change materials (PCM) play a key role in device performance for non-volatile random-access memory. Here, we report the nanothermal morphology of amorphous and crystalline phases in laser pulsed GeTe and $Ge_2Sb_2Te_5$ thin films by scanning thermal microscopy (SThM). By performing SThM measurements and applying quantitative physical models to two film thicknesses, the PCM thermal conductivities and thermal boundary conductances between the PCM and SThM probe are independently estimated for the amorphous and crystalline phase of each stoichiometry.

9.2. Foreword

As part of the collaboration with Dr. Kolosov, training was received by two graduate students and one postdoctoral associate to learn the SThM technique, an integral part of their research efforts. Fortunately, though, SThM had direct applications to semiconductor materials and phase change materials, and was proven as a useful tool for spatially mapping thermal properties for low thermal conductivity materials. What follows is the coupling of SThM with quantitative physical models to characterize the thermal conductivity and thermal boundary conductance for amorphous and crystalline phases of PCM thin films. The results demonstrate one possible avenue for SThM, with more discussed in the next chapter as future work to explore.

9.3. Introduction

Phase change materials (PCM) have been in the focus of research interest for the last decade as a candidate for non-volatile memories such as flash memory and dynamic random access memory

as they can combine high read/write speeds, excellent data retention, and low switching power [1]. Phase change memory is based on reversible switching between amorphous and crystalline states [2], producing remarkable reflectivity contrast for optical devices [3,4], and electrical conductivity modulation for solid state devices [5,6]. Finding stoichiometries that promote a fast crystallization time, lower threshold switching voltage/current between states, and improved high-cycle reliability are of particular interest [7]. Although various scanning probe microscopy (SPM) techniques have been employed to study these materials by electrical [1,8-11] and nanomechanical [12,13] means, there lacks a quantitative, non-destructive characterization method to investigate local nanoscale thermal properties of PCM that is a critical factor for their switching energy and read/write dynamics. Several methods are currently employed to study thermal properties, such as Raman spectroscopy and IR spectroscopy, however, these have a spatial resolution limited to the micron scale [14,15]. Scanning Thermal Microscopy (SThM) [16], on the other hand, would be ideal for quantitatively measuring and mapping local thermal properties, with the added potential capability of directly reading and writing 'bits' of data (phase changed regions) with spatial resolution down to the nanometer scale [17,18].

In the present work, we demonstrate a SThM approach to study the thermal properties of amorphous and crystalline phases of commercially viable PCM stoichiometries, $Ge_2Sb_2Te_5$ (a-GST/c-GST) and GeTe (a-GT/c-GT). These are selected as they demonstrate nucleation and growth dominated crystallization behavior, respectively [19]. The thermal responses for the amorphous and crystalline phases are modeled, with thermal conductivities compared with a range of previously reported values. This work is of particular interest to research efforts on determining the phase switching thresholds for phase change materials as a function of varying

experimental parameters, such as composition gradients, sample thickness, applied voltage, or power.

9.4. Materials and Methods

9.4.1. Sample fabrication and SThM experimental setup

The phase change materials considered here are the most common commercially viable stoichiometries, GST and GT, which demonstrate nucleation and growth dominated crystallization behavior, respectively. Two different samples were studied for each material, consisting of sputtered (Moorfield MiniLab 25) 100 and 200 nm thick films of amorphous phase change material on glass coverslips (substrate). In between each phase change film and glass substrate, a 10 nm layer of Ti was sputtered to promote adequate bonding, an order of magnitude thinner than the PCM film, to minimize its influence on measured thermal properties.

Following specimen fabrication, each film was mounted onto a motorized XYZ stage and illuminated with a focused 514 nm wavelength Ar ion laser of varying power from 3 to 4 mW on the sample (Spectra Physics). The specimens were programmatically translated with a step motor controller (Honda Electronics) at 50 μm per second to create crystalline lines in the amorphous films with a consistent heating per unit area. SThM images of various sizes were acquired on the amorphous and crystalline phases of both film thicknesses allowing to investigate the nanoscale thermal properties and corresponding morphology. For the quantitative evaluation of thermal properties, force-distance curves (0.1 Hz ramp rate) were obtained while simultaneously acquiring the thermal signal during approach and retract to determine the temperature drop upon contact with the specimen. Such approach and retract profiles were collected on the crystalline and amorphous regions for both film thicknesses.

All measurements were acquired in ambient temperature and humidity with a Bruker Multi Mode Scanning Probe Microscope with Nanoscope III controller. Thermal transport measurements were performed using SThM probes (Kelvin Nanotechnology, KNT-SThM-01a, 0.3 N/m spring constant, <100 nm tip radius), that were thermally calibrated to relate the probe resistances to probe temperature [20].

The calibrations were done on a Peltier hot/cold plate (Torrey Pines Scientific, Echo Therm IC20) by incrementing the temperature and recording the probe resistance using ratiometric approach (Agilent 34401A digital multimeter) [21]. This was performed externally to the SPM to prevent additional heating from the SPM deflection laser. At first, a DC voltage (sufficiently small to exclude self-heating) was applied to the probe using an arbitrary waveform generator (Agilent 33220A) linking the probe resistance to the ambient temperature. Next, the applied voltage of the probe was increased ensuring controlled self-heating, while recording the probe resistance (Figure 46) therefore determining the temperature of the probe self-heating as a function of excitation voltage.

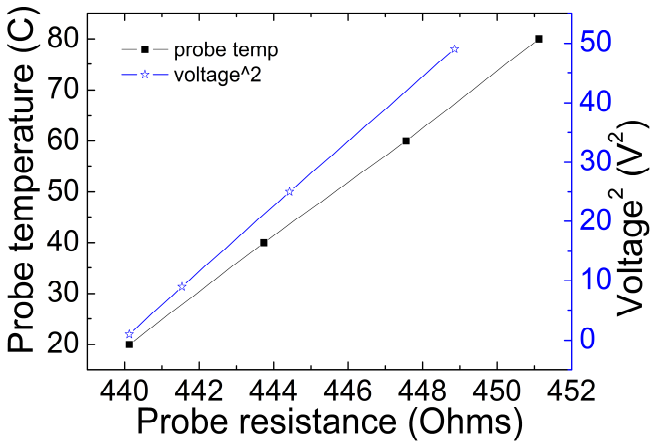

Figure 46: SThM probe calibration at 1 V_{DC}. The left axis presents the probe temperature as a function of probe resistance, while the right axis presents self-heating of the probe. The quadratic scale indicates a linear increase in probe resistance with Joule heating power (~V^2).

The SThM electrical measurements were performed by sensor heating [22,23] with an AC-DC bridge configuration, presented elsewhere in detail by Tovee et al [20]. As expected, the SPM laser illumination for measuring deflection heated the probe by 10°C, therefore adding to the Joule heating of the probe. All measurements were performed with a set-force below 15 nN during imaging to protect the tip and sample from damage to either structure.

For quantification of thermal properties of the phase change specimens, the equivalent thermal resistance between the probe and its surroundings, R_T, is considered according to previous models (Figure 47) as defined by the following equation [16,20]:

$$R_T = \frac{T_H - T_0}{Q_h} \tag{9.1}$$

where T_H and T_0 is the heater and ambient temperature, respectively, and Q_h is the heat generated by the heating element. During the specimen fabrication stage of the experimental process, it is very important to select a sample geometry and substrate that promote optimal contrast for SThM measurements. It is well known from previous experimental data [24,25] that one of the most important factors to consider is the tip/sample thermal boundary conductance (TBC), also known as Kapitza conductance (σ_{ts}, i.e. the reciprocal of $1/R_{ts}$) [26-29]. The SThM response will strongly depend on the tip-sample junction PCM as well as the tip-heater thermal conductance. In preliminary experiments, a 50 nm thin film of phase change material was sputtered onto a substrate of doped Si. However, the Si substrate, having a very high thermal conductivity, negatively impacted the results of the PCM thin film by masking any local conductivity variations between the tip and sample. By selecting a much thicker phase change film (100-200 nm) and substrate with significantly lower thermal conductivity (soda lime glass), the heat transport in the PCM film dominated the measurements, producing notably better results (i.e.

stronger SThM sensitivity to the varying properties of the phase change material and resulting resolution of nanoscale features). Additionally, by performing SThM measurements on two different film thicknesses, i.e. 100 and 200 nm films, and assuming a uniform TBC regardless of thickness (a reasonable approximation given that the mean free path of the heat carriers (phonons) in PCM is much shorter than film thicknesses involved) [30], the true sample thermal conductivity may be extracted from the experimental SThM data.

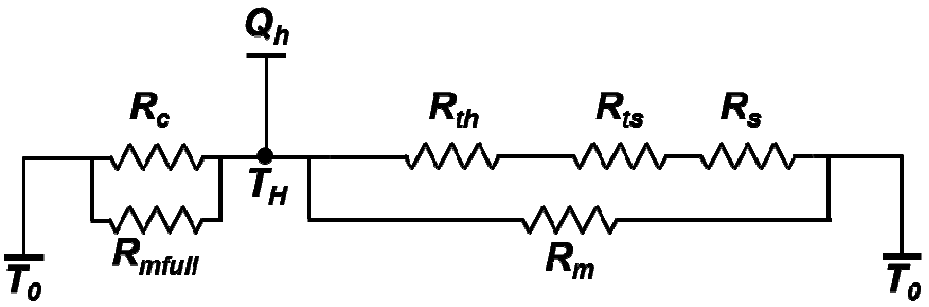

Figure 47: The equivalent thermal resistance between the probe and its surroundings are considered according to previous models.[20] The heat generated by the heating element, Q_h, is transferred through the environment surrounding the cantilever holder, via thermal resistance R_{mfull}, and through the cantilever base itself, via thermal resistance R_c. At the tip apex, the heat is transferred to the environment, R_m, through the tip and heater, R_{th}, and while in contact with the sample, the tip-sample contact resistance, R_{ts} and sample resistance, R_s. The heat generated will create a thermal gradient between the heater, T_H, and ambient environment, T_0.

9.4.2. Quantitative Physical Modeling

A three dimensional finite element analysis (FEA) was performed using commercial software (COMSOL Multiphysics, Joule Heating module) in order to determine the influence of cantilever/sample geometry and sample materials properties on the SThM experimental results. By isolating and understanding the interplay of these factors, the thermal conductivities of the amorphous and crystalline phases can be estimated.

The FEA model is based on the experimental setup as described, with a SThM cantilever, GST or GeTe thin film, soda-lime-silica glass substrate, and thin Ti interlayer between the PCM and substrate. The proportions and materials used for the modeled SThM cantilever were similar to

those implemented in the experiments, Figure 48(a), with 250 nm Au pads and 150 nm Pd resistors micro-patterned on a commercial Si_3N_4 cantilever base [20]. The modeled PCM samples consist of a 2 µm x 8 µm crystalline phase positioned between two 8 µm x 8 µm amorphous phases, with a thickness equal to either 100 or 200 nm (based on the two SThM experimental cases considered). The cantilever and sample were placed in air environment, and the temperature profile of the entire 3-Dimensional system was calculated, Figure 48(b). The thermal conductivities for all materials used in the 3D model are presented in Table 6. Note that the thermal conductivities of the sputtered Au pads and Si_3N_4 cantilever base, with effective values of 170 and 4.5 W/m-K, respectively, are determined by matching the heat-temperature balance and conductance values of the SThM probe in air (within 0.25 to 0.50 K at 293 and 353 K) with experimental data for both hot plate and self-heating calibration measurements, while accounting for the electrical circuit of the probe containing two 100 Ω resistors in series with the heater.

As discussed previously, the tip-sample TBC (σ_{ts}) is important for accurately accounting for the thermal resistance of the probe-sample junction, and therefore for determining the thermal conductivity of the amorphous and crystalline phases for each stoichiometry we studied. This may be presented as:

$$\sigma_{ts} = \rho_c \, \pi \, {r_{ts}}^2 \tag{1.2}$$

where ρ_c and r_{ts} are the conductance and effective interface radius of the contact between the tip and sample, respectively. To incorporate the TBC in the FEA simulation, we include a thin resistive layer between the tip apex and the sample represented by a cylinder with height (h)

much smaller than the contact diameter ($2\,r_{ts}$). The thermal conductivity of the TBC is then calculated as:

$$\sigma_{ts} = h * \rho_c \tag{1.3}$$

The thermal transport in most regions of the modeled SThM system can then be handled by standard heat transfer equations. The characteristic dimensions of the structural elements are on the order of 50 nm to micrometres, which in all cases are higher than the mean free paths in the various materials components, allowing use of the diffusive heat transfer equation [31]:

$$\rho C_p \frac{\partial T}{\partial t} = k\Delta \mathrm{T} + \mathrm{Q} \tag{1.4}$$

where ρ is the density of the material, C_p is the heat capacity at constant pressure, k is the media thermal conductivity, and Q is the heat source. The temperature distribution is assumed to be time independent due to the slow ramp rate of the force-distance curves, so the left hand side of eq. 1.4 equates to zero. By solving eq. 1.4 for all structural parts of the system (Figure 47) and with the proper boundary conditions, we then obtain the modeled temperature distribution. The thermal boundary conditions were set such that the temperature of the surrounding environment as well as the initial temperature of all domains was 293 K. A fixed electrical potential difference is applied across Pd resistors at the probe apex as identified in Figure 48(a) (the only domain in the model to include an electrical component) to induce local Joule heating reflecting experimental conditions. Finally, the thermal discontinuity experienced by the probe when brought into contact or out of contact was calculated and compared to that of corresponding experimental data. By adjusting the thermal properties of the modeled amorphous and crystalline

phases to match the SThM experimental results, the measured amorphous and crystalline PCM thermal properties are estimated.

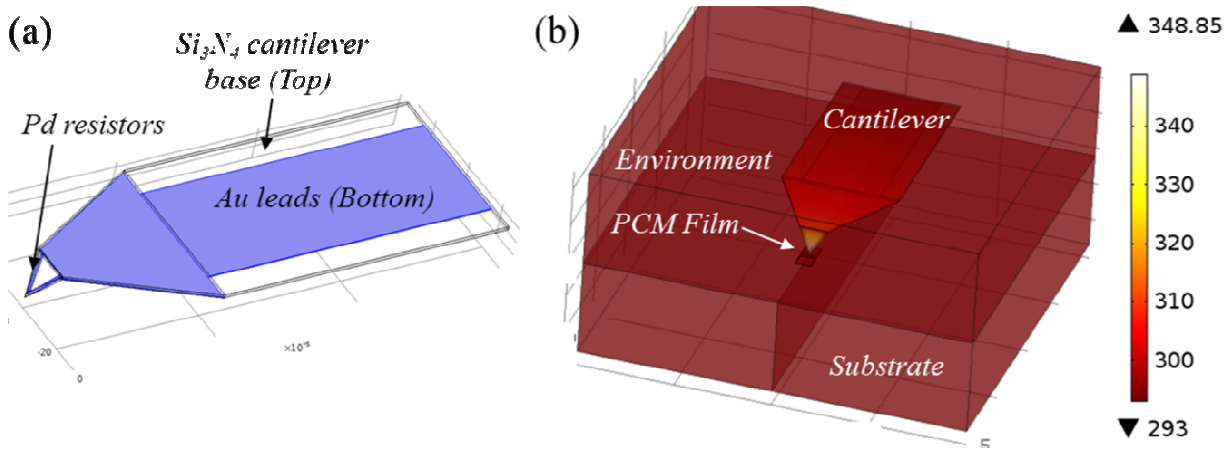

Figure 48: The design of the SThM probe with Si_3N_4 cantilever base, Au pads, and Pd resistors (a) reflected in the simulation. The model system comprises a cantilever approaching a PCM film on a soda lime glass substrate, and the ambient air environment (b).

Table 6: Thermal conductivities (W/m-K) for all materials used in the FEA model. *Note that effective values are used for Au and Si_3N_4 thin films to match the experimentally measured probe thermal and electrical resistances for the hot plate and self-heating calibration measurements.

Pd	Soda-lime glass	Air	Ti	Au	Si_3N_4
71 [32]	1.05 [33]	0.02 [34]	21.9 [32]	170*	4.5*

9.5. Results and Discussion

Figure 49(a,c) presents representative topography (left) and corresponding SThM (right) images for the 200 nm GT specimen with 10 and 2.5 µm scan sizes, respectively. Figure 49(b,d) presents similar results for the 200 nm GST specimen, but with 8 and 2.5 µm scan sizes, respectively. The

SThM images display the temperature of the SThM sensor, henceforth labeled as 'thermal images' with constant power applied to the probe.

Topographically, the depressions running down the centers of the height images correspond to the crystalline phases nucleated in the surrounding amorphous film by the pulsed laser as it traversed the film. Such a specific volume reduction between amorphous and crystalline phases is expected, and is typically 5% for these stoichiometries [35].

For the SThM images, the thermal response is uniformly darker (decreased contrast) for the crystalline phase compared to the surrounding amorphous film, indicating a combined tip-sample and sample spreading thermal resistance, $R_{ts} + R_s$, which is lower than for the amorphous regions.

There are two noteworthy aspects related to the morphology at the boundary between the amorphous and crystalline phases. The higher magnification SThM images in Figure 49(c,d) identify that the boundary is sharper for GT versus GST. Figure 49(c) reveals a 30 to 50 nm transition between the crystalline and amorphous regions for GT. For GST, on the other hand, the gradient in thermal properties from crystalline to amorphous regions occurs over 80 to 440 nm, Figure 49(d). Furthermore, the crystal/amorphous boundary represents a relatively straight line for the GST film, while for GT it has clear deviations from such line. While the line undulation may be expected due to the discrete motion of the step motor, the fact that it is more prominent for the GT film may relate to the growth dominated crystallization behavior for GT as compared to GST, causing more variability in GT phase boundaries once nucleation sites become activated.

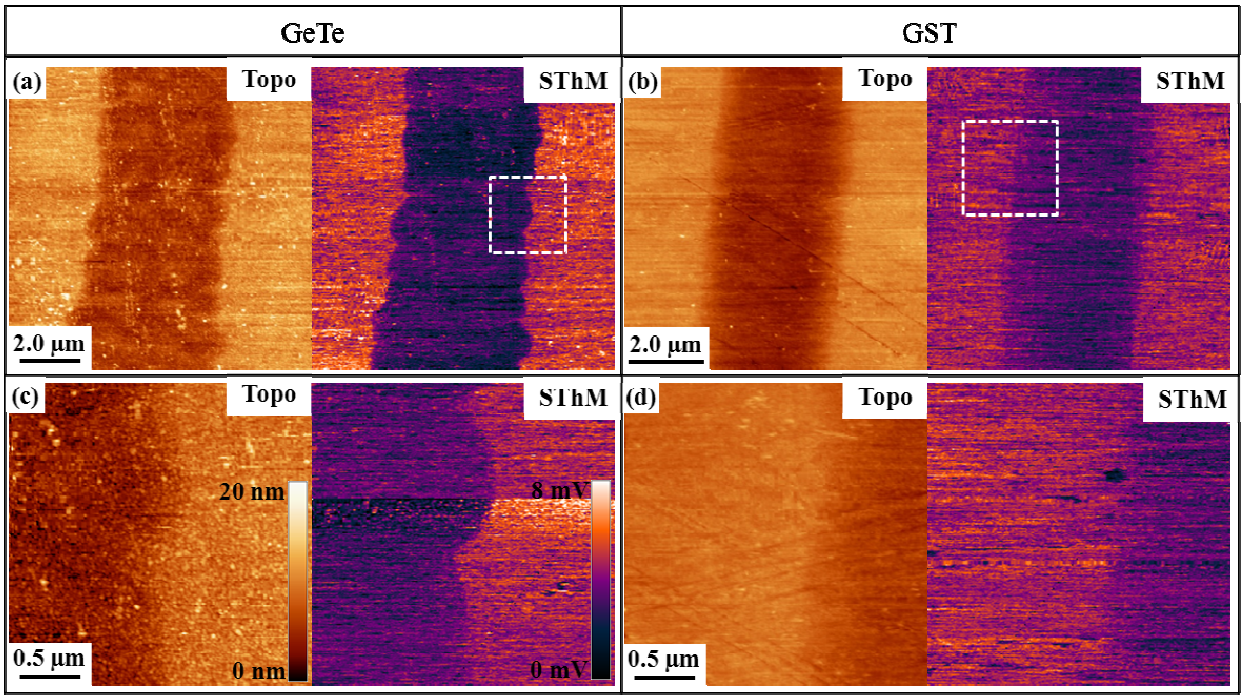

Figure 49: Topography (left) and SThM (right) images with 10 µm (a) and 8 µm (b) scan sizes, respectively, revealing a crystalline line written into 200 nm GT and GST amorphous thin films by a scanned, pulsed laser. The 2.5 µm images (bottom row) for GT (c) and GST (d) are taken from the spatial locations marked by the insets in (a,b).

To better quantify the thermal properties of the crystalline and amorphous regions of each film, conventional 'force-distance' curves were acquired with the SThM tip by approaching until contacting the surface, then retracting until separation, recording the piezo displacement, lever deflection (normal force), and thermal signal throughout. Figure 50(a,b) presents such force-distance curves for 200 nm crystalline and amorphous GST films, respectively, with the tip approaching from the left, snapping to contact leading to a slight decrease in deflection, then linearly deflecting positively as the displacement increases further, indicating that the SThM lever is highly compliant compared to the sample. Figure 50(c,d) presents the simultaneously acquired thermal signals, with approach (dashed) and retraction (solid) directions also identified as shown. While approaching the sample, the thermal signal decreases linearly until the point of tip/sample contact (compare with the snap-in displacements from Figure 50(a,b)), at which point the signal abruptly decreases due to the added tip-sample thermal conductance. During tip

retraction, adhesion forces maintain contact until pull-off occurs as is typical for AFM-based measurements in ambient conditions. The thermal signal again changes sharply, now due to loss of contact, after which the thermal response matches the previous, non-contact values.

When comparing the crystalline (Figure 50(c)) to amorphous (Figure 50(d)) thermal approach curves, the thermal drop is notably stronger for the crystalline phase, consistent with the SThM imaging performed in Figure 49 where the crystalline regions exhibit lower signals. To quantify this parameter more thoroughly, such sharp drops and the subsequent rise in the thermal response for approach and retract, respectively, were averaged for several groups of successive force-distance curves (N=3) and analyzed for each stoichiometry, specimen thickness, and phase. The approach portion of these experimental results was then compared with thermal modeling for equivalent conditions. It is worth noting that the retract curves could have also been used for comparisons to thermal modeling, as experimentally they display similar trends as observed in Figure 50. However, the magnitudes of the thermal jumps are generally less reliable since retraction curves also depend on adhesion effects during tip/sample pull-off. An increase in adhesion would thus produce a larger pull-off displacement (~75 vs. ~40 nm for crystalline and amorphous GST, respectively, in Figure 50), and hence a greater pull-off deflection (~150 vs. ~60 nm), distorting interpretation of the corresponding thermal jump as if a higher thermal conductivity were encountered. The snap-to-contact displacement, and deflection, for approach curves are susceptible to adhesion to much smaller degree with this nearly uniform change in lever deflection (~20 nm). Therefore, any error caused by such adhesion-based artifacts (if present) is minimized for approach curves that are therefore preferred for the SThM quantitative measurements.

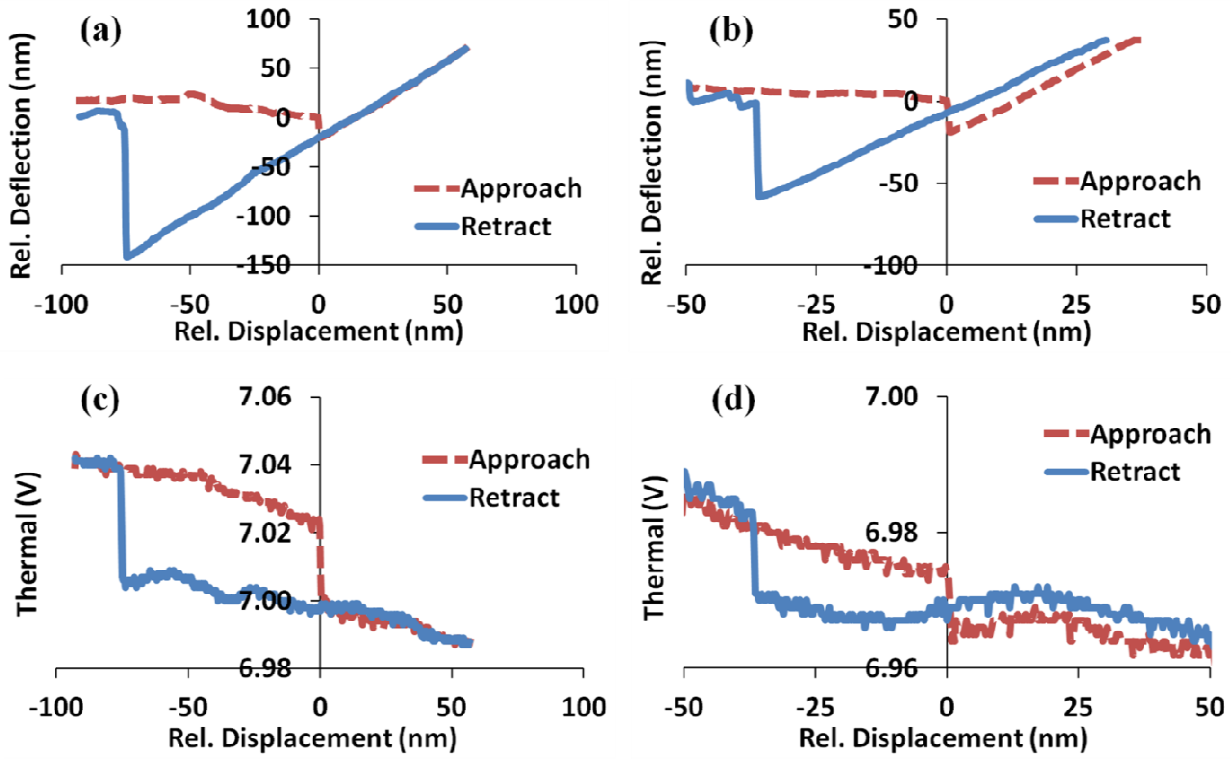

Figure 50: The typical approach and retract SThM curves for PCM materials, with simultaneously recorded relative cantilever deflection (a,b) and thermal (c,d) signal as a function of relative displacement for contact with crystalline (a,c) and amorphous (b,d) GST phases.

The observed thermal "drops" upon contact with the crystalline phases are consistently larger regardless of film thickness, and for both GST and GT (not shown for brevity). However, the contrast between the crystalline and amorphous phase is stronger for thicker PCM films, as anticipated due to the larger contribution of the film with respect to the underlying glass substrate. Since tip-sample TBC R_{ts} is identical for both measurements but the thermal resistance of the film R_s differs with the film thickness, the tip-sample contact resistance can be extracted with appropriate models. The TBC is determined using the acoustic mismatch model (AMM) [27]. It is then considered as an equivalent cylinder representing the tip/sample contact area (see Methods), and the modeled thermal drops are calibrated to match the experimental values. Finally, the influence of the TBC is removed to determine the thermal conductivity of each phase and material.

The temperature distribution of the modeled SThM system is presented for the SThM probe out of contact (Figure 51(a)) and in contact (Figure 51(b)) with c-GST, as well as out of contact (Figure 51(c)) and in contact (Figure 51(d)) with a-GST. The model accounts for the substrate, underlying adhesion layer, chalcogenide film, environment, probe geometry near the apex, and distinct probe materials including a primary silicon nitride tip as well as the resistive heating elements.

For contact with the crystalline GST film, heat is conducted easily from the probe in the plane of the film, and through the glass substrate. This predicts the largest temperature drop of the probe, as measured experimentally. For contact with the amorphous GST film, on the other hand, the higher thermal resistance limits heat dissipation in-plane as well as into the glass substrate, retaining more heat locally. As a result, a weaker thermal drop is predicted, and experimentally measured. When out of contact, the highest temperature of the probe is observed, with minimal heat loss to the PCM and underlying glass substrate as expected. Nevertheless, for near-contact conditions as modeled (50 nm separation), the a-GST (Figure 51(c)) is noticeably hotter than the c-GST out of contact (Figure 51(a)). Equivalent in- and out-of-contact thermal distributions were prepared for c- and a- phase GT, but again are omitted as they follow a similar trend.

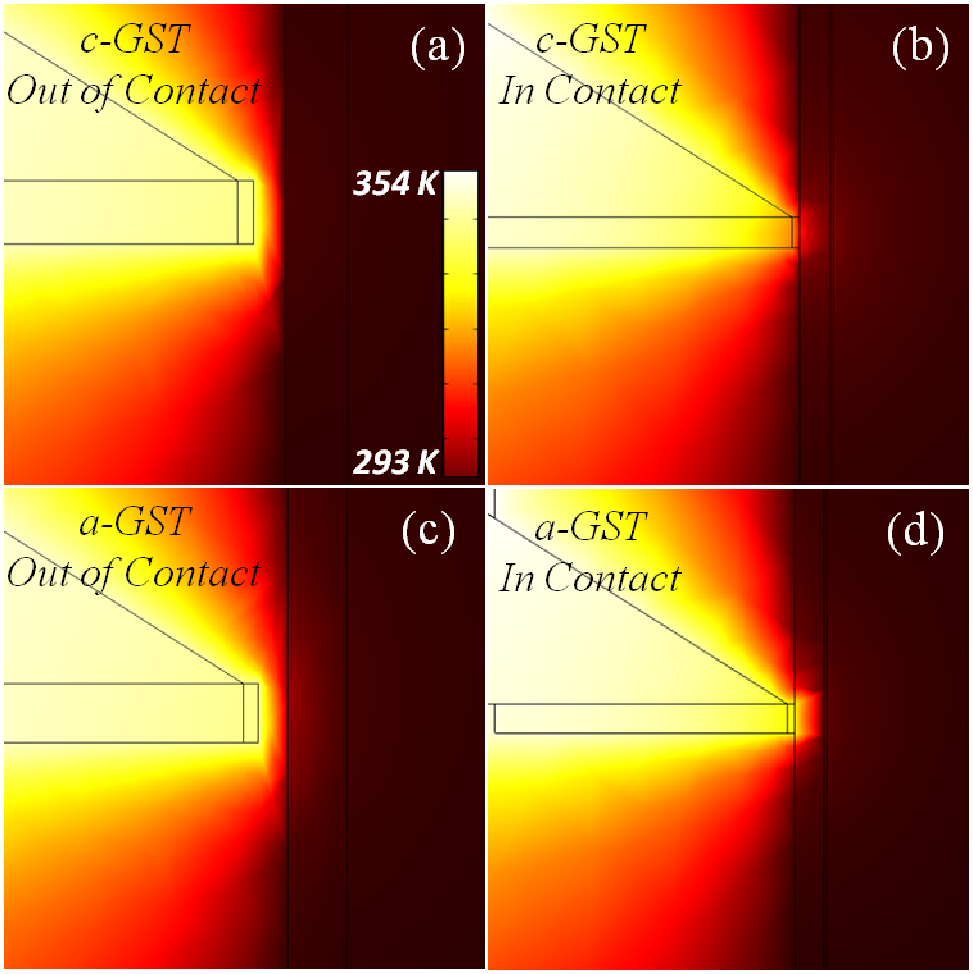

Figure 51: Cross-section view of the simulated temperature distribution between the SThM probe and sample. (a) Out-of-contact and (b) in-contact data for 100 nm c-GST vs out-of-contact (c) and in-contact (d) of 100 nm a-GST film. The out of contact tip/sample distance is 50 nm, and the temperature scale bar applies to all cases. Although not fully visible in (a) and (c), the 10 nm Ti layer is present and incorporated into the temperature distribution model.

The thermal conductivities of a-GST/c-GST (Figure 52(a)) and a-GT/c-GT (Figure 52(b)) thin films are finally calculated by iteratively fitting the model to the experimentally acquired thermal drops. As presented in Table 7, the resulting thermal conductivities for a-GST and c-GST are 0.30 and 1.95 $Wm^{-1}K^{-1}$, respectively, while they are 0.20 and 1.60 $Wm^{-1}K^{-1}$ for a-GT and c-GT. These locally measured thermal conductivities for a-GST and c-GST are within the range of values determined by previous studies using more macroscopic methods, 0.19 to 0.33 $Wm^{-1}K^{-1}$ [27,36,37] and 1.1 to 2.0 $Wm^{-1}K^{-1}$ [36,37] respectively. The particularly high a-GST value may

be explained by considering film preparation, where elevated temperatures during sputtering could result in the presence of a small fraction of nucleated crystalline phase as observed in separate mechanical studies [38] and hence a higher effective thermal conductivity. Additionally, as the experimental a-GST phase was placed between two c-GST reference lines, that may also somewhat contribute to increased heat conduction and therefore result in a higher observed thermal conductivity. Finally, standard deviation error bars reveal a higher uncertainty for the crystalline phase of each stoichiometry. This results from a stronger variation in the experimentally measured thermal "jumps" for the crystalline regions. This can be linked to variations in the local crystallite orientations under the SThM probe and hence a wider range of directionally dependent thermal properties. The resulting a-GT and c-GT thermal conductivity values are considerably lower than those previously reported [39], 2.3 and 5.7 $Wm^{-1}K^{-1}$ for a- and c-GT, respectively. However, the discrepancy in the values may be explained by the contrasting measurement methods. For example, the thermal conductivity measurements on a- and c-GT by Nath and Chopra [39,40] were acquired on a 900 nm film at steady-state, by an in-plane thermal gradient over a 4.0 x 0.5 cm length scale, clearly demonstrating a convergence with bulk values. Here, the thermal gradient was applied normal to the thin film surface, with heat flow considered over an area 6 orders of magnitude less.

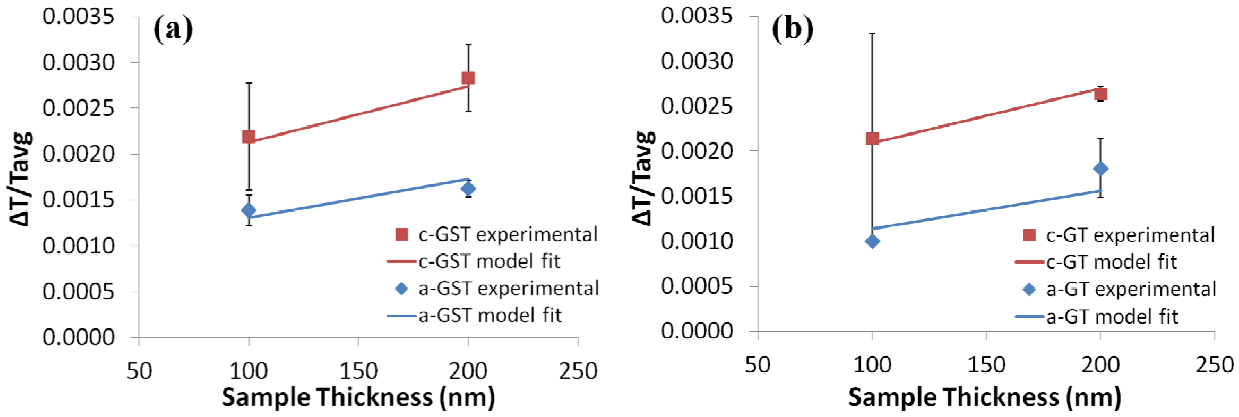

Figure 52: Normalized thermal drop (ΔT/Tavg) versus sample thickness for amorphous and crystalline GST phases, including experimental data (with standard deviation error bars, N=3) and a model fit (a). Similar data is presented for amorphous and crystalline GT (b).

Table 7: Thermal conductivities (W/m-K) for amorphous and crystalline phases of GST and GT, acquired by fitting the simulated temperature profile of the probe to those measured experimentally with force-displacement curves.

Phase	a-$Ge_2Sb_2Te_5$	c-$Ge_2Sb_2Te_5$	a-GeTe	c-GeTe
Thermal conductivity [W/m-K]	0.30	1.95	0.20	1.60

The TBC between GST films and substrates of different materials (C, Ti, TiN) has been calculated elsewhere using the acoustic mismatch model (AMM) [27]. However, thermal time-domain thermoreflectance (TDTR) data reveals approximately one order of magnitude lower conductance values due to interfacial effects such as grain boundaries, impurities, and surface defects [41]. For example, AMM values range from 5.0×10^8 to 3.3×10^{10} $Wm^{-2}K^{-1}$ and 5.3×10^8 to 1.4×10^{10} $Wm^{-2}K^{-1}$ for a-GST and c-GST, respectively, while TDTR values range from 3.9×10^7 to 5.6×10^7 $Wm^{-2}K^{-1}$ for c-GST (no data is available for a-GST). The TBC values for a- and c-GST in contact with a Si_3N_4 SThM probe as implemented here have not been reported, so values were calculated instead based on the acoustic mismatch and geometry [26,42], specifically 7.0×10^8 and 3.8×10^7 $Wm^{-2}K^{-1}$ [27] between a-GST/Si_3N_4 or c-GST/Si_3N_4

contacts, respectively. TBC values for a- and c-GT in contact with the Si_3N_4 probe have also not been explicitly reported, so the a- and c-GST values were applied; a reasonable assumption as the GST/GT Debye temperatures are similar [43,44].

9.6. Conclusion

Scanning thermal microscopy (SThM) has been implemented to characterize optically switched chalcogenide phase change materials of GeTe (GT) and $Ge_2Sb_2Te_5$ (GST). Quantitative physical models together with the experimental results allowed to account for the thermal boundary conductance, and to directly determine both the thermal conductivities of the amorphous and crystalline phases as well as contact thermal resistances. The thermal conductivities for amorphous and crystalline GST are 0.30 and 1.95 $Wm^{-1}K^{-1}$, respectively. The thermal conductivities for amorphous and crystalline GT are 0.20 and 1.60 $Wm^{-1}K^{-1}$, respectively. The reported approach has been demonstrated as an effective tool for measuring thermal properties of nanoscale phase change materials, while distinguishing thermal contrast of distinct phases down to 50 nm. SThM provides an alternative characterization method to IR imaging or Raman micro-spectroscopy, and is applicable for the characterization of other thin film materials with similar low thermal conductivities.

9.7. References

1. D. Loke, T. H. Lee, W. J. Wang, L. P. Shi, R. Zhao, Y. C. Yeo, T. C. Chong, and S. R. Elliott, Science **336** (6088), 1566 (2012).
2. Stanford R. Ovshinsky, Physical Review Letters **21** (20), 1450 (1968).
3. M. Libera and M. Chen, Journal of Applied Physics **73** (5), 2272 (1993).
4. W. Welnic, S. Botti, L. Reining, and M. Wuttig, Physical Review Letters **98** (23) (2007).
5. M. H. R. Lankhorst, B. W. S. M. M. Ketelaars, and R. A. M. Wolters, Nat Mater **4** (4), 347 (2005).
6. M. Wuttig and N. Yamada, Nat Mater **6** (11), 824 (2007).
7. D. Lencer, M. Salinga, B. Grabowski, T. Hickel, J. Neugebauer, and M. Wuttig, Nat Mater **7** (12), 972 (2008).

8. J. L. Bosse, I. Grishin, Y. G. Choi, B. K. Cheong, S. Lee, O. V. Kolosov, and B. D. Huey, Applied Physics Letters **104** (5) (2014).
9. J. Kim, Scanning **32** (5), 320 (2010).
10. H Bhaskaran, A Sebastian, A Pauza, H Pozidis, and M Despont, Review of Scientific Instruments **80** (2009).
11. H. Satoh, K. Sugawara, and K. Tanaka, Journal of Applied Physics **99** (2) (2006).
12. I. Grishin, B. D. Huey, and O. V. Kolosov, Acs Appl Mater Inter **5** (21), 11441 (2013).
13. James L. Bosse, Ilya Grishin, Bryan D. Huey, and Oleg V. Kolosov, arXiv:1406.2416v1 (2014).
14. W. W. Cai, A. L. Moore, Y. W. Zhu, X. S. Li, S. S. Chen, L. Shi, and R. S. Ruoff, Nano Letters **10** (5), 1645 (2010).
15. A. A. Balandin, S. Ghosh, W. Z. Bao, I. Calizo, D. Teweldebrhan, F. Miao, and C. N. Lau, Nano Letters **8** (3), 902 (2008).
16. A. Majumdar, Annu Rev Mater Sci **29**, 505 (1999).
17. M. A. Lantz, B. Gotsmann, U. T. Durig, P. Vettiger, Y. Nakayama, T. Shimizu, and H. Tokumoto, Applied Physics Letters **83** (6), 1266 (2003).
18. Manuel E. Pumarol, Mark C. Rosamond, Peter Tovee, Michael C. Petty, Dagou A. Zeze, Vladimir Falko, and Oleg V. Kolosov, Nano Letters **12 (6)**, 2906 (2012).
19. J. H. Coombs, A. P. J. M. Jongenelis, W. Vanesspiekman, and B. A. J. Jacobs, Journal of Applied Physics **78** (8), 4918 (1995).
20. P. Tovee, M. Pumarol, D. Zeze, K. Kjoller, and O. Kolosov, J Appl Phys **112** (11) (2012).
21. Peter Tovee, Manuel E. Pumarol, D. A. Zeze, Kevin Kjoller, and O. Kolosov, J. Appl. Phys. **112**, 114317 (2012).
22. M. Chirtoc, X. Filip, J. F. Henry, J. S. Antoniow, I. Chirtoc, D. Dietzel, R. Meckenstock, and J. Pelzl, Superlattice Microst **35** (3-6), 305 (2004).
23. P. Grossel, O. Raphael, F. Depasse, T. Duvaut, and N. Trannoy, Int J Therm Sci **46** (10), 980 (2007).
24. Peter D Tovee and Oleg V Kolosov, arXiv:1110.6055v3 (2013).
25. Peter D Tovee, Manuel E Pumarol, Mark C Rosamond, Robert Jones, Michael C Petty, Dagou A Zeze, and Oleg V Kolosov, arXiv:1305.6240 (2013).
26. Jean-Luc Battaglia, Vincent Schick, Clément Rossignol, Andrzej Kusiak, Isabelle Aubert, Alessio Lamperti, and Claudia Wiemer, Appl Phys Lett **102**, 181907 (2013).
27. E Bozorg-Grayeli, J P Reifenberg, K W Chang, M Panzer, and K E Goodson, (2010).
28. J Reifenberg, E Pop, a. Gibby, S Wong, and K Goodson, Thermal and Thermomechanical Proceedings 10th Intersociety Conference on Phenomena in Electronics Systems, 2006. ITHERM 2006., 106.
29. L J Challis, Journal of Physics C-Solid State Physics **7**, 481 (1974).
30. H. S. P. Wong, S. Raoux, S. Kim, J. L. Liang, J. P. Reifenberg, B. Rajendran, M. Asheghi, and K. E. Goodson, Proc. IEEE **98** (12), 2201 (2010).
31. John H Lienhard, (2008).
32. C. Y. Ho, R. W. Powell, and P. E. Liley, Journal of Physical and Chemical Reference Data **1** (2), 279 (1972).
33. L.P.B.M. Janssen and C.G. Warmoeskerken, *Transport Phenomena Data Companion*. (Edward Arnold, 1987).
34. William M Haynes, *CRC handbook of chemistry and physics*. (CRC press, 2012).

35. V. Weidenhof, I. Friedrich, S. Ziegler, and M. Wuttig, J Appl Phys **86** (10), 5879 (1999).
36. H K Lyeo, D G Cahill, B S Lee, J R Abelson, M H Kwon, K B Kim, S G Bishop, and B K Cheong, Appl Phys Lett **89** (2006).
37. J. L. Battaglia, A. Kusiak, V. Schick, A. Cappella, C. Wiemer, M. Longo, and E. Varesi, J Appl Phys **107** (4) (2010).
38. J. L. Bosse, P. D. Tovee, B. D. Huey, and O. V. Kolosov, J Appl Phys **115** (14) (2014).
39. Prem Nath and K. L. Chopra, Physical Review B **10** (8), 3412 (1974).
40. Prem Nath and K. L. Chopra, Thin Solid Films **18** (1), 29 (1973).
41. J. P. Reifenberg, K. W. Chang, M. A. Panzer, S. Kim, J. A. Rowlette, M. Asheghi, H. S. P. Wong, and K. E. Goodson, Ieee Electr Device L **31** (1), 56 (2010).
42. K Børkje and SM Girvin, New Journal of Physics **14** (8), 085016 (2012).
43. H. Wang, Y. Xu, M. Shirnono, Y. Tanaka, and M. Yarnazaki, Mater Trans **48** (9), 2349 (2007).
44. Y. Ishihara, Y. Yoshita, and I. Nakada, J Phys Soc Jpn **55** (6), 1948 (1986).

Chapter 10: Conclusion and Proposed Future Work

10.1. Introduction

The multiparametric techniques developed as part of this work have allowed the research community to characterize a diverse range of materials systems with added functionality and benefits. A few examples of these include the development of an AFM capable of higher scan rates, characterizing performance parameters faster and with a higher spatial resolution, improving image quality through error correction, and applying automated spectroscopic methods to quantify results. In most cases, technique developments were made in response to challenges faced with the characterization of specific materials properties. In some cases, the methodology and effectiveness was demonstrated for a different materials system entirely, namely those that present expected behavior with sufficient contrast. Therefore, the focus of future efforts should be to A) continue the development of AFM-based techniques, B) demonstrate their effectiveness on a proven materials system, and most importantly C) close the loop by utilizing them to fully characterize the original material(s) system under investigation. What follows is a discussion of future experiments and analysis, to not only demonstrate these new techniques, but apply them to materials systems that may benefit from their development. Finally, materials properties that were left unexplored in the original scope of this work are addressed.

10.2. Phase Change Memory Thin Films

As part of the scope for the project to characterize the switching dynamics of chalcogenide phase change materials, samples were fabricated with a stoichiometry more representative of those used in commercial applications. These samples were grown without a capping layer to allow for laser induced crystallization, and then studied with various AFM techniques at the collaborators

site (Lancaster, UK). This included nanomechanical characterization by ultrasonic force microscopy, and scanning thermal microscopy for thermal characterization. The electrical characterization was then performed locally (Storrs, USA). Adequate data for nanomechanical morphology (Chapter 8:) and thermal conductivity (Chapter 9:) was acquired while stationed overseas in the collaborators laboratory, but all of the films oxidized during transport back to the US, resulting in heterogeneities at the free-film surface (see 10.2.1). Anticipating this potential problem before leaving the UK, secondary films were fabricated with the chalcogenide layer sandwiched between carbon layers, which has been previously shown to protect the films from oxidation, while still allowing the flow of current during AFM imaging [1]. Unfortunately, electrical characterization failed on the "in-house" fabricated carbon coated films, resulting in a negligible current signal despite high applied bias (-10 to 10 V). It became clear that new samples must be fabricated. A fruitful discussion at a recent conference with an experienced chalcogenide film fabricator sparked a collaboration that resulted in the production of new, oxide-free films. What follows is a summary of preliminary experiments on the un-capped films, and a suggested plan for characterization and quantification of future results. Recommendations will also be made regarding the coupling of AFM studies and real-world device applications.

10.2.1. Switching Dynamics

After demonstrating the threshold switching capabilities by AFM methods for GeSe (Chapter 2:), the same technique was implemented to characterize commercially viable stoichiometries, $Ge_2Sb_2Te_5$ (GST) and GeTe (GT), as they display nucleation and growth dominated crystallization behavior, respectively. The experimental setup, film thicknesses, and fabrication techniques were identical to Section 2.3: Materials and Methods. Nanosecond voltage pulses were applied to each stoichiometry to determine the switching threshold voltage duration and

amplitude. Two representative current images of pulsed crystalline bits within an amorphous film are presented with logarithmic scales spanning 7 orders of magnitude (1 pA to 10 µA), Figure 53. The results of the threshold switching experiment are presented in Figure 54.

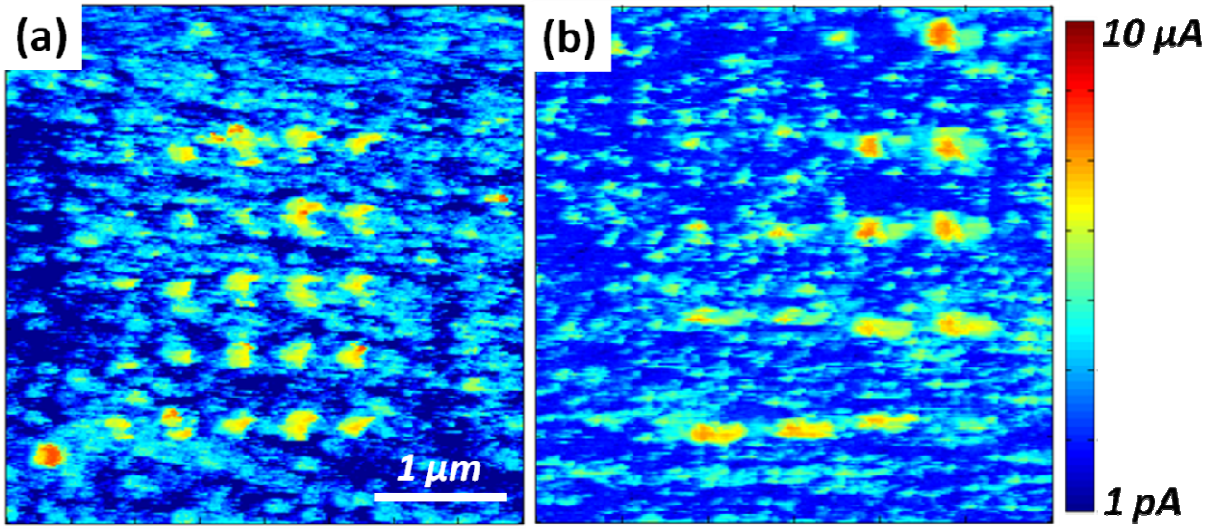

Figure 53: Current images of the pulsed amorphous GST (a) and GT (b) film with varying pulse amplitude and durations. The GST image displays crystalline bits applied with 10V pulse amplitude and 15-75 ns pulse durations for each column from left to right. All crystalline bits in the GT image are produced by 8V pulse amplitude and 30 ns pulse duration. Both images are acquired with read voltage of 1V.

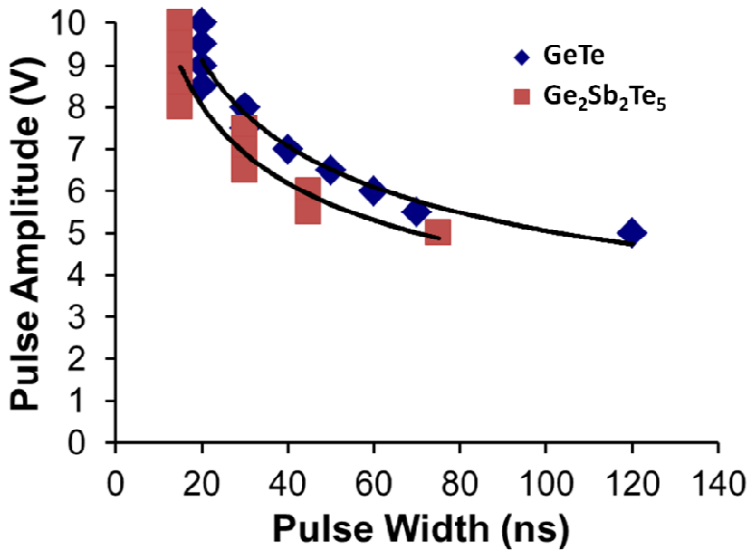

Figure 54: Minimum pulse amplitude and pulse duration required for the amorphous to crystalline phase transition in GST and GT thin films.

Preliminary results indicate faster switching with the GST as opposed to GT films, 15 versus 20 ns at 10V, respectively. As expected, both films did not demonstrate any phase switching with a pulse amplitude lower than a threshold electric field, in this case 5V across a 50 nm film thickness, corresponding to 100 V/µm.

The switching threshold voltage (5V) was then applied while collecting AFM image frames to study the nucleation and growth dynamics as a function of time for both stoichiometries. Unfortunately, each experiment did not produce consistent results, and only the GST film demonstrated a consistent current signal over an extended number of image frames, Figure 55. As expected, the original nucleation sites exhibited minimal growth, and many new nucleation sites formed. The experiment was performed several more times, but a similar quality of results was never observed. Additionally, the corresponding experiment performed on the GT film resulted in current signal degradation after only 10 image frames, Figure 56.

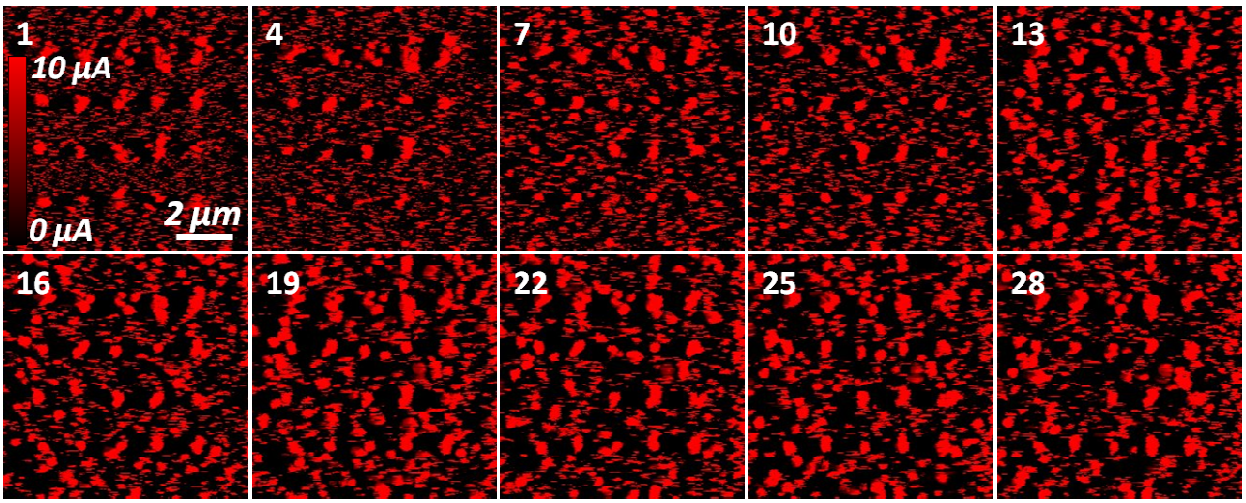

Figure 55: Montage of sequential current images with pre-pulsed crystalline bits in a GST thin film (6 µm scan size, 5V DC bias, 3Hz line scan rate). Films were pre-pulsed with 8V pulse amplitude and 1ms pulse duration. The image frame is indicated in the upper left hand corner.

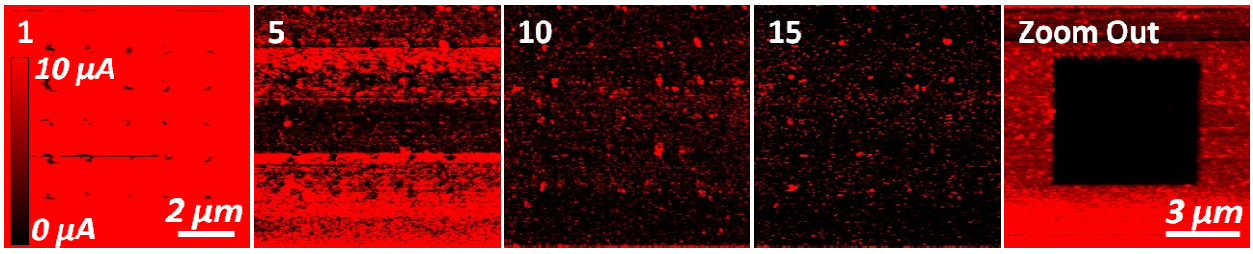

Figure 56: Montage of sequential current images with pre-pulsed crystalline bits in a GT thin film (6 µm scan size, 5V DC bias, 3Hz line scan rate). Films were pre-pulsed with 8V pulse amplitude and 1ms pulse duration. The image frame is indicated in the upper left hand corner. The final image frame was acquired after the montage was complete, with a 'zoomed out' 10 µm scan size to reveal the degradation in the current signal as a function of scanning time.

Despite imaging in an environment with Argon gas flow, the AFM image quality is due to an absent capping layer on the thin films. To address this issue, several new films have been fabricated with a Carbon capping layer to ensure that no oxide formation occurs at the free film surface [1].

My recommendation for future experiments is to characterize the switching thresholds by the methods employed in Chapter 2: on the GeSe films, and implement these values in a nucleation and growth study as outlined above for GST and GT. A "particle size" analysis with fixed threshold current value (ImageJ) should be performed for the quantification of nucleation and growth area (in nm^2) as a function of time. Another suggested method is to apply the Nanoscale Conductance Mapping (NCM) technique outlined in Chapter 3:, which is particularly useful for performing the first three-dimensional analysis of effective switched volume as a function of time.

10.2.2. Morphology

In Chapter 7:, a spectroscopic approach applied to ultrasonic force microscopy (sUFM) was demonstrated on various materials as a proof of concept for the optimization and quantification of nanomechanical properties. In Chapter 8:, this method was combined with beam exit Ar ion

polishing (BEXP) to characterize the free surface and shallow-angle cross-sections of PCM thin films. In the analysis of both GST and GT films, several interesting features were resolved, including bright, stiff [2] regions due to either crystalline nucleation [3,4], a TiO_x oxide layer, or transmission-sputtering erosion from the BEXP process [5]. To date, it is not certain which combination of these factors, and in what quantity, are present. Therefore, I recommend that a 2-nm C capping layer should be sputtered once the BEXP process is completed, which will be sufficiently thin to allow for adequate resolution during UFM characterization, but thick enough to prevent oxidation of the cross-sectioned surface. Nanomechanical characterization of an oxide-protected, cross-sectioned surface will allow for a more definitive investigation of amorphous and crystalline phase morphology, and may even be combined with electrical characterization (i.e. NCM) for a more complete study.

10.2.3. Thermal Modeling

In Chapter 9:, Scanning Thermal Microscopy (SThM) was demonstrated as an effective technique for the determination of thermal conductivity in low-k materials, such as amorphous and crystalline GST/GT, with <50 nm spatial resolution. The thermal conductivity of these phase change materials were determined by fitting quantitative physical models to experimental thermal "drops", where all of the heat generated was through Joule heating of the SThM cantilever materials by applied bias (Pd and Au). In the future, these quantitative models may be applied to Joule heating induced by nanosecond voltage bias across the PCM [6], between the AFM probe and the bottom electrode, similar to the experiments performed in Chapter 2: for GeSe, and in Section 10.2.1 for GST/GT. This would bring the community one step further in relating thermal results from an AFM study to real device performance.

Another recommended path to achieve this goal is within film fabrication. Unfortunately, in both experiments, the threshold voltages required to switch the phase change materials were only relative, as thermally insulating capping layers (C) and bottom electrodes (TiN) were not employed. By utilizing these additional layers and reducing the PCM film thickness to 10 nm, the threshold voltages required will approach those of operating devices, allowing for a more complete study regarding fast-crystallization stoichiometries by AFM methods [7,8]. Utilizing the AFM as a characterization tool capable of producing results within device-relevant performance ranges is very attractive, especially if pulse duration and amplitude results approach sub-nanosecond and 1-2V, respectively.

10.3. Friction Coefficient Mapping

While the community has utilized AFM-based techniques to quantify the coefficient of friction (COF) for a number of years, there lacks a controlled study regarding the influence of topography (surface slope changes), scan rate, and probe geometry on the COF [27]. For studies performed here (Section 5.7), calculated topographic artifacts due to the ratchet mechanism (i.e. tip/sample collisions) [9] should only result in a 56% higher COF when compared to artifact-free intrinsic material properties. However, the observed COF values are in excess of 300%. For future experiments, Friction Coefficient Mapping (FCM) may be used within a controlled experiment with fixed variables and discreet scan rates, on a sample that does not appreciably wear over time, i.e. nano-crystalline diamond. This would allow for spatially resolved quantification of the ratchet mechanism on the measured COF.

10.4. Error-Corrected AFM

The Error-Corrected AFM technique is applicable to any AFM mode where the error signal can be calibrated with regard to the materials property under investigation. The ease and quality of

the technique has been demonstrated for contact mode topography, non-contact mode topography, and non-contact mode phase imaging. One very interesting application would be to correct topography in real-time to improve the accuracy of a height-dependent materials property. One such example is for the improvement of Magnetic Force Microscopy (MFM) and Electric Field Microscopy (EFM), which critically depend on the distance between the AFM cantilever and the underlying surface [10,11]. In each case, the topography is mapped for one line, and the subsequent line scan traces over the same path and acquires the MFM/EFM signal, but with a tip-sample displacement between ~5 to 100's of nanometers. Higher quality data is found as this distance decreases, but then results in increased risk for tip-sample collision; a problem that will manifest only if the original traced height path was incorrect. Therefore, by collecting the height and the corresponding error signal during the first line scan, and implementing the error correction for the subsequent line, tip-sample distances may be decreased without sacrificing scan rate or image quality.

10.5. Spectroscopic Ultrasonic Force Microscopy

The spectroscopic approach to ultrasonic force microscopy (sUFM) has provided the community with a better understanding of the physical mechanisms that arise from different experimental parameters, such as the cantilever (length, spring constant, resonant frequency), piezotransducer (resonant frequency), and applied ultrasonic amplitudes. For the first time, the ultrasonic response as a function of frequency has been mapped to better understand the interplay of these factors. One key observation was the presence of sharp spikes in the ultrasonic response as the resonant frequency of the cantilever and piezotransducer converged, Figure 37(a-c) in Section 7.5.1. This behavior is undesirable for UFM measurements, as the ultrasonic response is mainly composed of cantilever resonance effects, rather than the nanomechanical response of the

underlying sample. Recently as part of this work, a high sampling rate (4 MS/s), real-time signal detection method has provided direct evidence for when these cantilever vibrations dominate the ultrasonic response. Figure 57 presents the cantilever deflection as a function of ultrasonic amplitude (and time) for one modulation cycle, demonstrating the influence of cantilever resonances on the ultrasonic response. The results suggest that previously reported literature may have suffered from these resonance effects, unfortunately. Therefore, for future experiments these vibrations may be quantified for many cantilevers, piezotransducers, and frequencies to determine optimal UFM conditions. This recent observation has a large impact on the high-frequency nanomechanics research community, as future data may be collected reliably, without the influence of these effects.

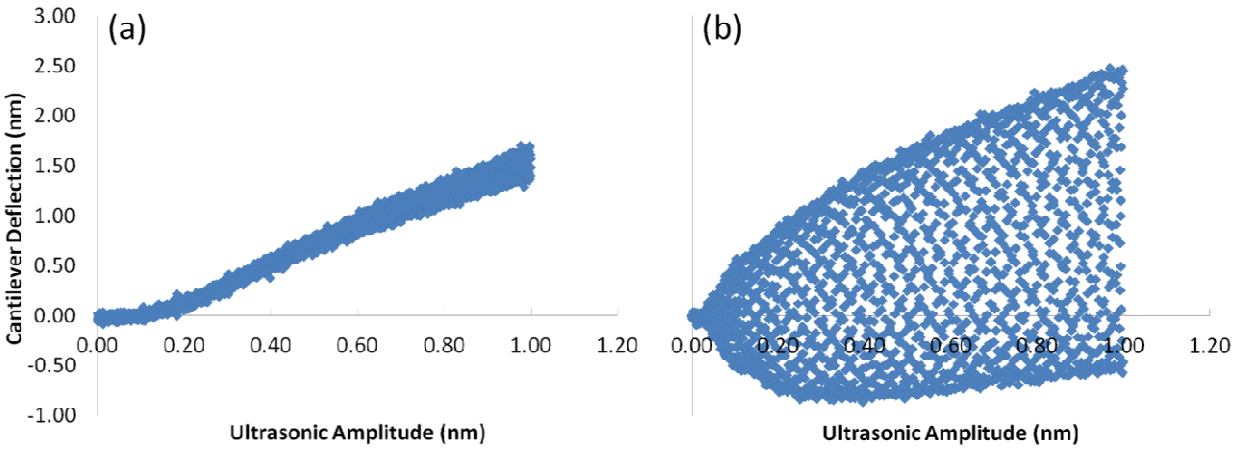

Figure 57: Cantilever deflection vs. ultrasonic amplitude with minimal (a) and excited (b) cantilever resonances, collected at 2.242 MHz and 1.897 MHz, respectively, both with 450 µm cantilever and 2 MHz piezotransducer. Note that the abscissa may also be represented as a function of time (500 µs period between 0 and 1 nm of ultrasonic amplitude), demonstrating vibrations in the time domain.

10.6. Conclusion

Throughout this dissertation, the scope of work has constantly changed, with new paths paved and pursued as a result of interesting observations and experiences. Providing tools to the research community for many AFM characterization modes has been a major driving force. As

with any successful research effort, more questions are now left to be answered than at the beginning of the journey. The beauty of science and research is that these questions never run out; there will always be many facets left to explore.

10.7. References

1. H. Bhaskaran, A. Sebastian, A. Pauza, H. Pozidis, and M. Despont, Review of Scientific Instruments **80** (8) (2009).
2. O. V. Kolosov, M. R. Castell, C. D. Marsh, G. A. D. Briggs, T. I. Kamins, and R. S. Williams, Physical Review Letters **81** (5), 1046 (1998).
3. Y. Choi and Y. K. Lee, Electron Mater Lett **6** (1), 23 (2010).
4. I. M. Park, J. K. Jung, S. O. Ryu, K. J. Choi, B. G. Yu, Y. B. Park, S. M. Han, and Y. C. Joo, Thin Solid Films **517** (2), 848 (2008).
5. O. V. Kolosov, I. Grishin, and R. Jones, Nanotechnology **22** (18) (2011).
6. S. Senkader and C. D. Wright, Journal of Applied Physics **95** (2), 504 (2004).
7. C. D. Wright, M. Armand, and M. M. Aziz, Ieee T Nanotechnol **5** (1), 50 (2006).
8. S. Gidon, O. Lemonnier, B. Rolland, O. Bichet, C. Dressler, and Y. Samson, Applied Physics Letters **85** (26), 6392 (2004).
9. Sriram Sundararajan and Bharat Bhushan, J. Appl. Phys. **88** (8), 4825 (2000).
10. D.. Bonnell, (Wiley-VCH, New York, 2001).
11. J. P. Cleveland, B. Anczykowski, A. E. Schmid, and V. B. Elings, Applied Physics Letters **72** (20), 2613 (1998).